Multimode strong coupling of cold atoms to a fiber ring resonator including a nanofiber-based optical interface

DISSERTATION

zur Erlangung des akedemischen Grades

Doktor der technischen Wisschenschaften

eingereicht von

DI Martin Blaha
Matrikelnummer 01025913
Anningerstraße 76-78/4, 2353 Guntramsdorf

an der
Fakultät für Physik der Technischen Universität Wien

Betreuung: Prof. Dr. Arno Rauschenbeutel, E141 – Atominstitut/Institut für Physik, Humboldt Universität zu Berlin

Diese Dissertation haben begutachtet:

Prof. Dr. Jakob Reichel
Prof. Dr. Pablo Solano

Martin Blaha

Wien, am 21.04.2021

Multimode strong coupling of cold atoms to a fiber ring resonator including a nanofiber-based optical interface

DISSERTATION

Submitted in partial fulfillment of the requirements for the degree of

Doktor der technischen Wisschenschaften

by

DI Martin Blaha
Matrikelnummer 1025913
Anningerstraße 76-78/4, 2353 Guntramsdorf

to the Faculty of Physics
at the Vienna University of Technology

Advisor: Prof. Dr. Arno Rauschenbeutel, E141 – Atominstitut/Institut für Physik, Humboldt Universität zu Berlin

____

The dissertation has been reviewed by:

Prof. Dr. Jakob Reichel	Prof. Dr. Pablo Solano

Martin Blaha

Wien, am 21.04.2021

In the beginning the universe was created
This made lot of people very angry and has been widely regarded as a bad move
– *Douglas Adams*

Erklärung zur Verfassung der Arbeit

Martin Blaha
Anningerstraße. 76-78/4, 2353 Guntramsdorf

Hiermit erkläre ich, dass ich diese Arbeit selbständig verfasst habe, dass ich die verwendeten Quellen und Hilfsmittel vollständig angegeben habe und dass ich die Stellen der Arbeit - einschließlich Tabellen, Karten und Abbildungen -, die anderen Werken oder dem Internet im Wortlaut oder dem Sinn nach entnommen sind, auf jeden Fall unter Angabe der Quelle als Entlehnung kenntlich gemacht habe.

(Ort,Datum)

Martin Blaha

Abstract

In recent decades, a special research focus was laid on the realization of strong interaction between optical emitters and the confined electromagnetic field inside a resonator, coined as cavity quantum electro dynamics (QED). In the context of this thesis, a novel regime of cavity QED was investigated, where the coupled atom–cavity system operates in a regime inaccessible to most established cavity setups, the multimode strong coupling regime.

During the thesis, an experimental apparatus was set up, that is designed to strongly couple an ensemble of atoms to a long fiber ring resonator featuring an integrated optical nanofiber for interfacing the resonator field with laser-cooled atoms. For sufficiently large atom numbers our system enters the regime of multimode strong coupling. Here, the atom–resonator coupling strength is larger than the free spectral range of the resonator and the atoms will simultaneously couple to several longitudinal resonator modes.

Alongside the experimental realization, we developed a theoretical formalism based on photon transport, that allows us to describe our experimental system that, being a long fiber ring resonator, operates at the boundary between waveguide and cavity QED. With the explicit consideration of a position dependent cavity field and not restricting our description to a single longitudinal mode of the resonator, we could calculate a theoretical prediction for the steady state of our resonator. Furthermore, it enables us to quantify the effects of multimode strong atom–resonator interaction, well outside the scope of validity of the established Jaynes- and Tavis-Cummings models, that are typically used to describe cavity QED.

In the experiment, we measured the transmission spectra of the coupled atom–resonator system, that show a normal-mode splitting exceeding the free spectral range of the resonator, a clear evidence that we entered the multimode strong coupling regime. Moreover, the measured spectra agree well with the theoretical predictions from the model derived in the thesis.

Both, our theoretical and experimental findings differ qualitatively from that of the Tavis-Cummings model and could open the way to further investigations of light-matter interaction in the regime of multimode strong coupling. Moreover, our description can serve as an alternative to the established description of strong coupling, especially for systems in which the resonator field is significantly changed in a single roundtrip, and thus, with its terminology common to waveguide QED, open a new perspective for a better understanding of strong light-matter interaction.

Kurzfassung

In den letzten Jahrzehnten wurde ein besonderer Forschungsschwerpunkt auf die Realisierung der starken Wechselwirkung zwischen optischen Emittern und dem elektromagnetischen Feld innerhalb eines Resonators gelegt, deren Beschreibung als Resonator-Quantenelektrodynamik (QED) bezeichnet wird. In dieser Arbeit wird ein neuartiger Bereich der Resonator-QED untersucht, bei dem das gekoppelte Atom-Resonator System in das - den meisten etablierten Experimenten dieses Forschungsfeldes vorenthaltene - Regime der multimodalen starken Wechselwirkung vordringt.

Im Zentrum der präsentierten Arbeit steht ein neuer experimenteller Aufbau, der darauf ausgelegt ist, ein lasergekühltes Ensemble von Atomen an das Feld eines langen Faser-Ringresonators via integrierter optischer Nanofaser zu koppeln. Ab einer passenden Anzahl gekoppelten Atomen tritt unser System in das Regime der multimodalen starken Kopplung ein, welches sich dadurch auszeichnet, dass die Atom-Resonator Kopplungsstärke den freie Spektralbereich des Resonators übersteigt und die Atome gleichzeitig an mehrere longitudinale Resonatormoden koppeln. Des Weiteren entwickelten wir einen theoretischen Formalismus auf Basis des Photonentransports, der uns erlaubt unser System, welches an der Grenze zwischen Wellenleiter- und Resonator-QED arbeitet, zu beschreiben. Die explizite Berücksichtigung eines ortsabhängigen Resonatorfeldes und die Nichtbeschränkung auf eine einzelne longitudinale Mode des Resonators ermöglicht uns eine theoretische Vorhersage für den stationären Zustand unseres Systems zu berechnen. Insbesondere kann unser Model Effekte der starken Multimoden-Atom-Resonator Wechselwirkung quantifizieren, die bereits außerhalb des Gültigkeitsbereichs der etablierten Jaynes- und Tavis-Cummings-Modelle liegen, jene Modelle, die üblicherweise zur Beschreibung der Resonator-QED verwendet werden.

Unsere experimentell bestimmten Transmissionsspektren des gekoppelten Atom-Resonator Systems zeigen eine Normalmodenaufspaltung, die den freien Spektralbereich des Resonators überschreitet. Dies ist ein klarer Beweis dafür in das Regime der multimodalen starken Kopplung vorgedrungen zu sein. Die gemessenen Spektren stimmen gut mit unseren theoretischen Vorhersagen aus dem in dieser Arbeit abgeleiteten Modell überein. Damit ist gezeigt, dass sich sowohl unsere theoretischen als auch experimentellen Ergebnisse qualitativ von denen des Tavis-Cummings-Modells unterscheiden und den Weg für weitere Untersuchungen der Licht-Materie Wechselwirkung im Regime der multimodalen starken Kopplung öffnen. Darüber hinaus kann unsere Beschreibung als Alternative zur genauen Beschreibung der starken Kopplung für Systeme dienen, in denen das Resonatorfeld bereits in einem Durchgang signifikant verändert wird und somit, mit seiner für die Wellenleiter-QED üblichen Terminologie, einen neuen Blickwinkel zum Verständnis der starken Kopplung eröffnen.

Die approbierte gedruckte Originalversion dieser Dissertation ist an der TU Wien Bibliothek verfügbar.
The approved original version of this doctoral thesis is available in print at TU Wien Bibliothek.
TU Bibliothek Your knowledge hub WIEN

List of Publications

The following articles represent the (soon to be) published work described in this thesis:

- Johnson, A., Blaha, M., Ulanov, A. E., Rauschenbeutel, A., Schneeweiss, P., and Volz, J. (2019). Observation of Collective Superstrong Coupling of Cold Atoms to a 30-m Long Optical Resonator. *Physical Review Letters*, **123**(24), 243602.
- Blaha, M., Johnson, A., Rauschenbeutel, A., and Volz, J. (2021), Effects beyond the Tavis-Cummings model in many-atom cavity QED. *(in preparation)*

Introduction

A new chapter of physics was opened in the early 20th century, when the discreteness of light and matter found its way into the physicists means of describing the universe. With these quanta of light and matter, the foundations of modern quantum physics were laid, initiating a paradigm shift in the understanding of the world, making it richer, more interesting, and sometimes even harder to grasp.

The first indication of energy quantization arose in thermodynamics, where Planck [1] introduced it to accurately describe the composition of radiation emitted by a black body, such as for instance a glowing piece of metal. Taking the consequences of the postulated discrete energy quanta of light literally, led amongst others, to the understanding of the photo electric effect, by Einstein, confirming the link between energy and frequency of light [2]. The emerging understanding and acceptance of light and atoms having discrete energy levels allowed Schrödinger to develop a description relying on wave-like probability amplitudes to calculate the position of an electron in an atom. This way it was possible to describe the discrete spectrum of emitted light from a hydrogen atom as transition of the electron between atomic energy levels without contradictions [3]. Finally, with a fully quantized description of light by Dirac [4], it was possible to understand the processes behind atomic decay and spontaneous emission. Notably, in 1946, Purcell noticed that the decay rate of an emitter is not a fundamental characteristic of each atomic energy level but depends strongly on the environment the atom is placed in [5]. He showed that the decay rate can be largely increased when the emitter is put into a cavity. This triggered in-depth investigations of light–matter interaction at the fundamental quantum-mechanical level, known today as cavity quantum electro dynamics (cQED) [6–9].

The theoretical foundations of cQED are rooted in a simple fully quantized model by Jaynes and Cummings, developed in 1963 [10]. At its principles, the model describes a single electromagnetic field in a cavity interacting with a single two-level atom and predicts, for example, a fast coherent energy exchange between the atom and the cavity field. With this model it was possible to correctly calculate the periodically changing probabilities of finding an emitter in its excited state when coupled to a cavity, known as Rabi-oscillations. Furthermore, this model predicted the collapse and revival of the atomic inversion over time, a phenomenon that could be experimentally verified two decades later [11].

Before the experimental achievement of coupling a single atom to a cavity field, it was discovered, that the interaction strength between light and matter is increased when coupling a few atoms to a cavity. This behaviour is generally described by the Tavis-Cummings model [12], which together with Jaynes-Cummings paved the way of understanding and exploiting the quantum nature of light–matter interaction, where to this day these models are the main theories behind the description of cQED.

In recent decades, ensuing experiments centred around light–matter interaction inside cavities led to new technologies and applications in many sprouting research fields, such as quantum metrology [13], quantum simulation [14], quantum communication [15, 16] and information processing [17]. Ultimately, the field of cQED has been acknowledged representatively with a Nobel Prize “for ground-breaking experimental methods that enable measuring and manipulation of individual quantum systems." in 2012 [18].

In parallel to (and as part of) the development of experimental cQED, it was soon understood, that the fundamental quantized processes in atoms are often masked by the much larger energy scales present in the atom’s external degree of freedom, mainly its movement due to thermal excitation. It is thus crucial to thermally isolate the atoms for precise measurements, where utilizing the light–matter interaction allowed for the development of new methods for cooling and trapping atoms [19, 20], as well as manipulating their position in space [21].

For the research presented in this thesis, interfacing atoms with resonant probe light is done via an optical nanofiber. Nanofibers are optical fibers tapered down to a diameter of about half the wavelength of the guided light, resulting in significant confinement of the light and a strong increase of its intensity. In nanofibers, a large fraction of the light is guided on the outside of the fiber as evanescent field, that can mediate very strong interaction with emitters in close vicinity of the fiber. It has been theoretically predicted [22] and experimentally confirmed [23–25] that trapping and interfacing of neutral atoms via nanofibers can be done. Using this interface, it was possible to investigate fundamental atomic physics [26–28] and build applications such as for instance quantum memories [29, 30]. Recently, atom–light interaction under the non-intuitive polarization properties of guided light in the nanofiber was investigated in greater detail. The observed effects of asymmetric emission from atoms into a waveguide opened a new regime in the field of waveguide QED (wQED), where the so-called chiral interaction facilitated via spin-momentum locking between light and matter is investigated [31–33].

In this thesis, we investigate a new regime of cavity QED which lies at the boundary between traditional cavity and waveguide QED. To this end, we built a long fiber ring resonator with an integrated optical nanofiber coupled to an ensemble of laser-cooled atoms. Experimentally, this setup allows us to reach the so called multimode strong coupling regime, where the collective coupling strength between the ensemble and the resonator surpasses the free spectral range of the latter, i.e., $g_N > \nu_{\mathrm{FSR}}$ [34–36]. Consequently, the atomic ensemble couples simultaneously to several longitudinal resonator modes.

To this end, we set up an experimental apparatus, allowing for the trapping and cooling of atoms in a magneto optical trap (MOT), optimised to reach optical densities (OD) of the atomic ensemble, probed through the fiber, exceeding $\mathrm{OD} = 50$. We carefully characterized two implementations of fiber ring resonators, using a 29.3 m and a 45.5 m long fiber ring, that are presented in this thesis. For an accurate determination of coupling strength between the individual atoms and the resonator field, we utilized correlation measurements of fluorescence photons, emitted from the atoms into the nanofiber. By doing so, we could measure the number of atoms coupling to the guided mode of the nanofiber, thus, infer the single-atom optical density for our setup. Finally, as the main focus of this work, I show the measured transmission spectra of our coupled resonators, that exhibit clear signatures of operation in the regime of multimode strong coupling. In an outlook, I present initial experimental studies of the temporal response of the atomic ensemble to abrupt changes in the excitation field, which reveals collective effects of the coupled emitters.

As the standard ensemble resonator description using the multimode version of the Tavis-Cummings model did not yield a correct theoretical description of our experiment we developed a new model utilizing a modified approach based on photon transport in wQED, as introduced in [37–39]. This model allows us to consider a successive, cascaded interaction of each individual atom with the cavity field. This is fundamentally different to the “superatom” model deployed by Tavis-Cummings, where the ensemble–cavity field interaction is described as part of a collectively enhanced single–atom interaction. The predictions of our model agree well with our measurements, thus, we could experimentally confirm the validity of our predictions.

Outline The thesis is outlined in the following manner: In chapter 1, I will discuss the basic implementation of optical resonators and describe the concept of strong coupling between a single emitter and the optical field of a cavity by introducing the theoretical framework of Jaynes-Cummings [10] and Tavis-Cummings [12]. Furthermore, I will present the concept of optical nanofibers - the key element of our resonator - and discuss the unique behaviour of nanofiber-based resonators, which is their length independent cooperativity. Consequently, we are enabled to experimentally enter the new regime of multimode strong coupling for a sufficiently long fiber ring resonator.

In chapter 2, I will discuss conditions for which the Jaynes- and Tavis-Cummings model are valid and will show that for our experimental parameters these conditions are not fulfilled. To accurately describe the coupled atom–resonator system beyond these limits, I will introduce a real-space approach considering the photon-propagation in the resonator. Assuming chiral interaction between the nanofiber guided light and the atoms, we solve for the steady-state solutions of the resonator fields and for the power spectrum of the output of the coupled resonator. In the remainder of this chapter, I will apply the introduced real-space approach to different scenarios of atom–resonator coupling and discuss the expected outcome with respect to the predictions of the established cQED models and point out the deviations between their predictions and those of our model.

In chapter 3, I will introduce the optical nanofiber as the main tool facilitating light–matter interaction. First, I will discuss the optical properties of nanofibers, presenting the solutions for the mode profile functions of guided light inside the nanofiber. Second, I will summarize the fabrication process and the optimisation steps that were performed during installation of our new fiber pulling rig. Lastly, I will present the experimental characterization of the nanofibers that were produced and used in our setup.

In Chapter 4, I will discuss the optical properties of birefringent fiber ring resonators and how we utilize polarization spectroscopy to lock our resonator. I will present the experimental environment to interface and lock the resonator, as well as the detection setup used for our transmission and correlation measurements. In a last step, I will summarize the characterization of our two implementations of fiber ring resonators and discuss the different loss channels that limit the resonator finesse and suggestions for improving the setup.

In chapter 5, the experimental setup will be described, where I will elaborate on details of the vacuum chamber, the concept and experimental implementation of our MOT, the installed laser systems, and the experimental control environment. Particularly, in this chapter, I will introduce the concept of using correlation measurements of fluorescence photons to determine the number of atoms coupled to the nanofiber.

Lastly, in chapter 6, I will discuss the conducted cQED experiments, showing transmission spectra of our atom–resonator system which show that we enter the strong and multimode strong coupling regime for both implemented resonators. Additionally, I provide a brief outlook into the investigation of the temporal dynamics of the coupled system.

To conclude this thesis, I will summarize all reported findings of this thesis and provide an outlook to further investigations in chapter 7.

Table of contents

Introduction **xv**

1 Theory of optical resonators **1**
1.1 Introduction to optical resonators . . . 1
1.2 Interaction between light and matter in resonators . . . 3
1.2.1 Jaynes-Cummings model - single emitter in a cavity . . . 3
1.2.2 Tavis-Cummings model - many emitters in a cavity . . . 5
1.2.3 Multimode coupling . . . 6
1.3 Experimentally realized atom–resonator interaction - strong coupling regime 7
1.3.1 Strong coupling regime . . . 8
1.3.2 Solution of an interfaced resonator . . . 8
1.4 Nanofiber resonators - length independent cooperativity . . . 11

2 Cascaded interaction approach **13**
2.1 Limits of conventional cQED models . . . 13
2.2 Cascaded interaction approach . . . 15
2.2.1 General approach . . . 15
2.2.2 Chiral light–matter coupling . . . 18
2.3 Solutions to the chiral interaction approach . . . 19
2.4 Interpretation and comparison of solutions . . . 21
2.4.1 Atoms coupled to a single propagating field . . . 21
2.4.2 Empty resonator . . . 23
2.4.3 Cavity with vanishing finesse . . . 23
2.4.4 Single-atom strong coupling . . . 24
2.4.5 Collective strong coupling . . . 26
2.4.6 Collective strong coupling in our model . . . 26

3 Optical Nanofibers **31**
3.1 Optical properties of optical nanofibers . . . 31
3.1.1 Electromagnetic fields in the optical nanofiber . . . 31
3.1.2 Solutions of fiber guided modes . . . 32
3.1.3 Mode spectrum of guided light . . . 34
3.2 Manufacturing of nanofibers . . . 35
3.2.1 Method . . . 35

3.2.2 Monitoring and optimising the pulling process using the new rig . . . 37
3.2.3 Mounting of the fibers 38
3.2.4 Conclusions regarding new pulling rig 40
3.3 Experimentally implemented nanofibers 40

4 Experimental implementation of the fiber ring resonator 43
4.1 Polarization properties of light in fiber ring resonators 43
4.2 Locking the resonator 44
4.3 Implementation of the resonator 46
4.4 Interfacing the resonator 48
4.5 Characterization of the resonator 50
4.5.1 Resonator 1 - TU Wien 50
4.5.2 Resonator 2 - HU Berlin 52
4.6 Discussion 54
4.6.1 Implementation of resonators 54
4.6.2 Length considerations for the resonators 57

5 Experimental setup 59
5.1 Vacuum chamber and glass cell 59
5.1.1 Chamber design 60
5.1.2 Glass cell and fiber arm 61
5.1.3 Insertion of nanofiber 62
5.2 Magneto optical trap 64
5.2.1 Principle 64
5.2.2 Experimental Realization 66
5.2.3 Imaging and optical density 70
5.3 Laser systems 74
5.3.1 MOT lasers - Cooler and Repumper 74
5.3.2 Lasers for interfacing the resonator - Probe, Lock and Heating . . . 74
5.4 Experimental control environment 76
5.5 Coupling atoms to the nanofiber 78
5.5.1 Optical density trough the nanofiber 78
5.5.2 Atom number calibration 79
5.5.3 Pumping the ensemble through the fiber 79
5.5.4 Correlation measurements 81
5.5.5 Correlation measurements with the cavity switched on 86
5.6 Possible experimental improvements 87

6 Observation of multimode strong coupling 89
6.1 Experimental proceedings 89
6.1.1 Experimental sequence 89
6.1.2 Probing the resonator 90
6.1.3 Intensity calibration 91
6.1.4 Data acquisition 91

6.2 Transmission measurements 92
  6.2.1 Overcoupling the resonator - transition to waveguide physics 92
  6.2.2 Short ring resonator 93
  6.2.3 Multimode strong coupling 93
6.3 Further experiments 97
  6.3.1 Dynamics of multimode strong coupling 97
  6.3.2 Simplified experimental setup 98
  6.3.3 Observations 98

7 Summary and Outlook **103**
7.1 Summary 103
7.2 Outlook 104

App. A Driven optical cavity with loss **107**

App. B Multimode expansion for Jaynes- and Tavis-Cummings model **109**

App. C Transmission coefficients of the coupling beamsplitter **111**

App. D Solution to the chiral–interaction Hamiltonian **113**

App. E Atomic emission into the waveguide **117**

References **119**

Chapter 1

Theory of optical resonators

An optical resonator is in general every arrangement of optical components that isolates an electro-magnetic mode from the free-space continuum of modes allowing it to store light via longitudinal and transversal confinement. Resonators are versatile optical tools used in a variety of research related applications such as laser resonators, filtering etalons, short-term optical frequency standards, precise length measurements and most importantly for us, for providing resonant enhancement of intra-cavity power and therefore amplifying the interaction between optical (quantum) emitters and the light inside the cavity. In this research field, coined as cavity quantum electrodynamics (cQED), many exciting fundamental insights to light-matter interaction were investigated and optical resonators became an important tool for, as a few representative examples given, quantum information processing [17], investigation of non-linear optics [40, 41] and cavity optomechanics [42].

In this chapter, I will first introduce the properties of optical resonators and discuss common implementations. This will be followed by a discussion of how to model the interaction between light in a resonator and a quantum emitter. I will introduce the most common theoretical framework in cQED, formulated by Jaynes-Cummings [10] and Tavis-Cummings [12] to describe the coupling of a single and multiple emitters to the cavity field, respectively. Furthermore, I will derive an expansion to these models, including several longitudinal cavity modes to the description to find a classical limit of multimode atom–resonator coupling. In a next step, I will calculate the spectral features of a probed resonator subject to loss and discuss the strong coupling regime, where the atom–resonator interaction exceeds the resonator's loss rates. In the remainder of this chapter, I will discuss nanofiber-based resonators and their unique length independent cooperativity, which allows us to enter the multimode strong coupling regime when implementing such a nanofiber based fiber ring resonator.

1.1 Introduction to optical resonators

The idea in cavity quantum electrodynamics is to store light as long as possible to increase the time it can interact with a coupled emitter or equivalently to use the amplified intensity of the light to increase the interaction between the light and the emitter. There are different ways of implementing a cavity, the most common are presented here.

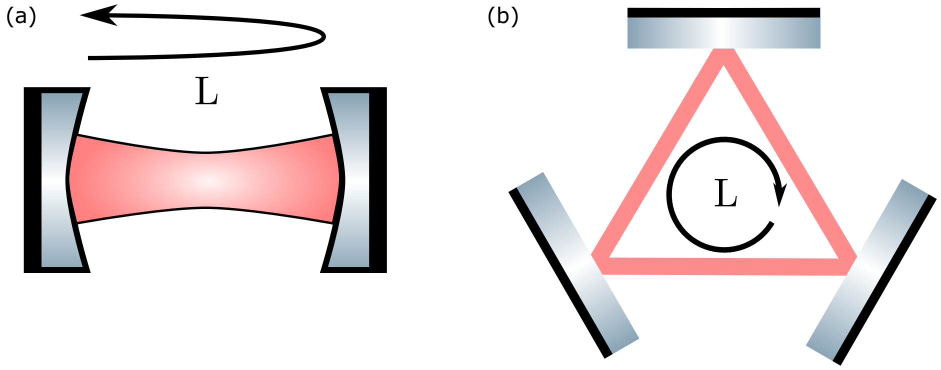

Fig. 1.1 While in a Fabry Pérot (a) the counter-propagating resonator field, creates a standing wave, a ring resonator (b) features two independently running waves.

Fabry-Pérot cavities A Fabry Pérot cavity is probably the most used implementation of a resonator and the common textbook example used to introduce the basic properties of optical cavities. As seen in Fig. 1.1(a), this resonator consists of two reflecting surfaces, e.g., mirrors or end facets of a glass plate with a distance $d = L/2$, where $L_{\mathrm{opt}} = nL$ is the roundtrip length of a cavity photon and n being the refractive index of the medium between the mirrors. The cavity is usually characterized by its finesse F, which quantifies the longitudinal confinement of light or, equivalently, is proportional to the number of roundtrips a photon undergoes before it is lost from the cavity, where

$$F = \frac{\nu_{\mathrm{FSR}}}{\delta\nu} = \frac{2\pi}{L_{\mathrm{tot}}}. \tag{1.1}$$

Here, $\nu_{\mathrm{FSR}} = \frac{c}{L_{\mathrm{opt}}}$ is the free spectral range, the frequency spacing between two successive resonances, c is the speed of light, $\delta\nu$ the linewidth of a resonance and L_{tot} the total roundtrip loss. As an example, in an empty symmetric Fabry-Pérot cavity, where losses only originate from scattering and absorption from the mirrors, they can be quantified as $L_{\mathrm{tot}} = 2(1-R)$, where R is the power reflection. A different way of characterizing a cavity uses the so-called quality factor

$$Q = \omega\tau = \frac{\omega}{2\kappa} = \frac{\omega F L_{\mathrm{opt}}}{2\pi c}. \tag{1.2}$$

Here, ω is the frequency of the light and τ the photon lifetime inside the cavity with a resulting photon decay rate $2\kappa = 1/\tau = 2\pi\delta\nu$. Both, Q and F can be used to compare resonators of different implementations, where Q can range up to 10^8 for state-of-the-art experiments [43, 44].

Ring resonators In contrast to the Fabry-Pérot cavity a ring resonator does not retro-reflect the light in the cavity. Instead, it constitutes an optical resonator where light can

Die approbierte gedruckte Originalversion dieser Dissertation ist an der TU Wien Bibliothek verfügbar.
The approved original version of this doctoral thesis is available in print at TU Wien Bibliothek.
TU Bibliothek WIEN Your knowledge hub

independently circulate in two different directions [45], thus featuring a pair of (near) degenerate resonator modes. Most common implementations of ring cavities use three (Fig. 1.1(b)) or four mirrors in a bow-tie configuration. Furthermore, there are additional implementations, namely whispering gallery resonators that utilize the total internal reflection of light in a tiny spherical optical element, allowing for compact resonator setups [44, 46]. In a similar manner as above, the finesse is defined for a ring resonator as $F = \frac{\nu_{\mathrm{FSR}}}{\delta\nu} = \frac{\pi}{L_{\mathrm{tot}}}$.

1.2 Interaction between light and matter in resonators

The description of the interaction of light and matter in high finesse cavities is generally referred to as cavity quantum electrodynamics (cQED) [6–9]. The theoretical foundation of this field of research was laid by Jaynes and Cummings in 1963 [10].

1.2.1 Jaynes-Cummings model - single emitter in a cavity

When quantifying light–matter interaction one considers typically a single two-level atom interacting with a single (resonator) mode. The atom inside this cavity is represented by an excited state $|2\rangle$ and a ground state $|1\rangle$ with an energy difference $\hbar\omega_{\mathrm{at}}$, depicted in Fig. 1.2. The electric field operator for light in the resonator, assuming a cavity mode profile $f(\vec{r})$ can be written as

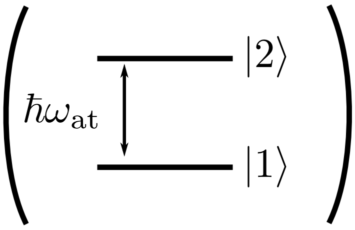

Fig. 1.2 Illustration of the Jaynes-Cummings model, where a two-level atom sits in a single-mode cavity. The atomic states are denoted as $|1\rangle$ for the ground state and $|2\rangle$ for the excited state, with an energy spacing $\hbar\omega_{\mathrm{at}}$ between them.

$$\hat{\vec{E}} = \vec{\varepsilon}\sqrt{\frac{\hbar\omega}{\varepsilon_0 V_0}}\left(\hat{a} + \hat{a}^{\dagger}\right) f(\vec{r}), \tag{1.3}$$

where $\vec{\varepsilon}$ is the unit polarization vector of the field, $\hat{a}$ ($\hat{a}^{\dagger}$) is the annihilation (creation) operator for a single photon in the resonator field, ω the optical frequency with $k = \omega/c$ being its wavevector, ε_0 is the vacuum permittivity and $V_0 = \int_V dV \varepsilon |f(\vec{r})|^2$ is the mode volume of the field inside the resonator of volume V and permittivity ε. The interaction part of the Hamiltonian in dipole approximation reads

$$\hat{H}_{\mathrm{int}} = -\hat{\vec{d}} \cdot \hat{\vec{E}}, \tag{1.4}$$

where $\hat{\vec{d}} = e\hat{\vec{r}}$ is the dipole operator of the atom with elementary charge e, characterizing the distribution of charge within the atomic system. For the atomic transitions we introduce the operators

$$\begin{aligned} \hat{\sigma}_+ &= |2\rangle\langle 1| \\ \hat{\sigma}_- &= |1\rangle\langle 2| = \hat{\sigma}_+^\dagger \\ \hat{\sigma}_z &= |2\rangle\langle 2| - |1\rangle\langle 1|, \end{aligned} \tag{1.5}$$

where $\hat{\sigma}_+$ ($\hat{\sigma}_-$) are the atomic raising and lowering operators and $\hat{\sigma}_z$ is the inversion operator. Using these operators, we can evaluate $\hat{\vec{d}} \cdot \hat{\vec{E}} \propto \hat{\vec{d}} \cdot \vec{\varepsilon} = d(\hat{\sigma}_+ + \hat{\sigma}_-)$, where $d = e\langle 2|\hat{\vec{r}} \cdot \vec{\varepsilon}|1\rangle$ is the electric dipole matrix element of the atomic transition. Thus, we obtain

$$\hat{H}_{\text{int}} = \hbar g(\vec{r})\,(\hat{\sigma}_+ + \hat{\sigma}_-)\left(\hat{a} + \hat{a}^\dagger\right). \tag{1.6}$$

Here we define the coupling strength between the field and the emitter by

$$g(\vec{r}) = \frac{-d}{\hbar}\sqrt{\frac{\hbar\omega}{\varepsilon_0 V_0}}\, f(\vec{r}), \tag{1.7}$$

where the rate of coherent energy exchange between the field and the two-level atom is proportional to this quantity. For an example given, assuming a plane-wave inside the cavity, where $f(\vec{r}) = 1$, thus V_0 being the volume of the cavity, the coupling strength can be determined to be (see [47])

$$g^2 = \frac{d^2\omega}{2\varepsilon_0\hbar V_0}. \tag{1.8}$$

The full Hamiltonian also includes the Hamiltonians of the uncoupled systems, the Hamiltonian of the two-level atom with the energy-level spacing $\hbar\omega_{\text{at}}$ and the Hamiltonian for a single-mode light field with ω_c being the frequency of the cavity light, given by

$$\begin{aligned} \hat{H}_{\text{at}} &= \frac{1}{2}\hbar\omega_{\text{at}}\hat{\sigma}_z \\ \hat{H}_{\text{c}} &= \hbar\omega_c\hat{a}^\dagger\hat{a}. \end{aligned} \tag{1.9}$$

Making use of the rotating wave approximation, where we neglect energy non-conserving terms $\hat{\sigma}_+\hat{a}^\dagger$ and $\hat{\sigma}_-\hat{a}$ in $\hat{H}_{\text{int}}$, one arrives at the Jaynes-Cummings Hamiltonian [10]

$$\frac{\hat{H}_{\text{JC}}}{\hbar} = \frac{1}{2}\omega_{\text{at}}\hat{\sigma}_z + \omega_c\hat{a}^\dagger\hat{a} + g\left(\hat{\sigma}_+\hat{a} + \hat{\sigma}_-\hat{a}^\dagger\right). \tag{1.10}$$

Eigenstates of Jaynes-Cummings model In a next step we solve for the system's eigenstates by diagonalizing the Hamiltonian in Eq (1.10). For n photonic excitations in the system the eigenenergies are given by

$$E_n = \hbar\omega(n + 1/2) \pm 1/2\hbar\Omega_n(\Delta), \tag{1.11}$$

where $\Omega_n(\Delta) = \sqrt{4g^2(n+1)+\Delta^2}$ is the so-called Rabi frequency evaluated for the atom–resonator detuning $\Delta = \omega_c - \omega_{\text{at}}$. In the un-coupled scenario, $g = 0$, the eigenstates $|1,n+1\rangle$ and $|2,n\rangle$ are referred to as bare states, where for the resonant case $\Delta = 0$, their energy is degenerate, with one energy quanta either stored in the excited atom or the field. In the coupled system $g > 0$, the new eigenstates are given by

$$\begin{aligned} |n,+\rangle &= \quad \cos(\theta_n/2)|2,n\rangle + \sin(\theta_n/2)|1,n+1\rangle \\ |n,-\rangle &= -\sin(\theta_n/2)|2,n\rangle + \cos(\theta_n/2)|1,n+1\rangle, \end{aligned} \tag{1.12}$$

where $\tan(\theta_n) = -\Omega_n(0)/\Delta$. These states are referred to as dressed states, shifted in energy with respect to the bare states, where the origin of this so-called AC-Stark shift was first discussed in [48]. Figure 1.3(b) compares the spectra of the coupled and uncoupled atom–resonator system for the resonant case of a single photonic excitation.

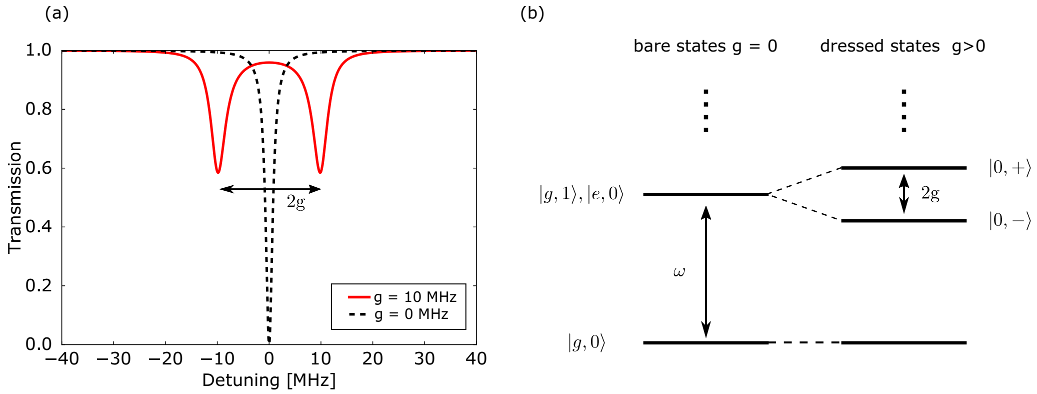

Fig. 1.3 (a) Expected measured spectrum of a coupled, lossy cavity interfaced with a weak driving laser resonant with the cavity and the atomic transition $\omega_c = \omega_{\text{at}}$. As one scans the probe frequency ω across resonance, two shifted transitions (red) are observed compared to the uncoupled case (black dotted). (b) Underlying spectrum, comparing the energy levels of bare and dressed states, when coupling the two-level atom to the field. The dressed states show an energy difference of $2g$ for a single photonic excitation.

When solving for the dynamics of the Jaynes-Cummings Hamiltonian, having the atom initially in the excited state, one observes so-called Rabi oscillations, where the probability of the atom being in the excited state oscillates with the frequency $\Omega_n(\Delta)$. In the case of a resonant cavity and an initially empty resonator (n=0) the atom will decay into the cavity and soon after reabsorb this photon, undergoing oscillations with a periodicity $\Omega_0 = 2g$, coined as vacuum-Rabi frequency.

1.2.2 Tavis-Cummings model - many emitters in a cavity

Reaching large coupling strengths g with a single emitter is technically a quite involved task making it necessary to design cavities with very small mode volumes (see Eq. (1.7)). To circumvent this technical obstruction one can instead make use of a collective enhancement by coupling N identical emitters to the cavity field increasing the coupling strength $g_N = \sqrt{N}g_1$, where g_1 is the single-atom coupling strength. The first description theoretically modelling this collective behaviour was done by Tavis and Cummings [12]. Following the Jaynes-Cummings Hamiltonian, one can sum up the individual energy contributions of N atoms coupling to a single-mode cavity field to be

$$\frac{\hat{H}_{TC}}{\hbar} = \sum_{n=1}^{N} \omega_{\text{at}} \hat{\sigma}_n^+ \hat{\sigma}_n^- + \omega_c \hat{a}^\dagger \hat{a} + \sum_{n=1}^{N} g_1 \left(\hat{\sigma}_n^+ \hat{a} + \hat{\sigma}_n^- \hat{a}^\dagger \right). \tag{1.13}$$

Given this approach, each atom has the same probability of absorbing from and emitting into the cavity, where we are not able to determine which atom actually did so. The whole ensemble therefore can be treated as one collective emitter, where a photonic excitation can excite a so-called spin wave in the atomic ensemble, described as a collective quasi-particle excitation. Assuming at most a single excitation in the system, one can define collective excitation and annihilation operators

$$\hat{S}_+ = \frac{1}{\sqrt{N}} \sum_{n=1}^{N} \hat{\sigma}_n^+ \text{ and } \hat{S}_- = \frac{1}{\sqrt{N}} \sum_{n=1}^{N} \hat{\sigma}_n^-, \tag{1.14}$$

that can be used to re-formulate Eq. (1.13) to read

$$\frac{\hat{H}_{TC}}{\hbar} = \omega_{\text{at}} \hat{S}_+ \hat{S}_- + \omega_c \hat{a}^\dagger \hat{a} + \sqrt{N} g_1 \left(\hat{S}_+ \hat{a} + \hat{S}_- \hat{a}^\dagger \right), \tag{1.15}$$

being the Tavis-Cummings Hamiltonian in the low-excitation limit. When comparing $\hat{H}_{TC}$ to $\hat{H}_{JC}$ one immediately sees, that in the Tavis-Cummings approach we expect the same behaviour as discussed for the Jaynes-Cummings approach before, but with an enhanced coupling strength $g_N = \sqrt{N}g_1$.

1.2.3 Multimode coupling

For large (collective) coupling strengths coming of the order of the free spectral range, limiting the description to single mode interaction may not be applicable. In order to consider additional modes, we expand the Jaynes-Cummings Hamiltonian to be

$$\frac{\hat{H}}{\hbar} = \omega_{\text{at}} \hat{\sigma}_+ \hat{\sigma}_- + \sum_j \omega_j \hat{a}_j^\dagger \hat{a}_j + \sum_j g \left(\hat{\sigma}_+ \hat{a}_j + \hat{\sigma}_- \hat{a}_j^\dagger \right), \tag{1.16}$$

where $\hat{a}_j^\dagger$ ($\hat{a}_j$) creates (annihilates) a photon in the j-th mode of the resonator. The resonator modes are separated by the free spectral range $\omega_{\text{FSR}} = 2\pi\nu_{\text{FSR}}$ and are given by $\omega_j = j\,\omega_{\text{FSR}} + \Delta_a$, where Δ_a is the atom–resonator detuning, defined for the resonance closest to ω_{at}.

In a similar way, we can apply this expansion to the Tavis-Cummings approach for at most a single excitation in the system by introducing the collective excitation operators

$\hat{S}_\pm = 1/\sqrt{N}\sum_n \hat{\sigma}_n^\pm$. For simplicity, the remainder of this discussion is shown for the Jaynes-Cummings method, but works analogously for Tavis-Cummings. The complete derivation for the steady state of the atom–resonator system, where the atoms strongly couple to many resonator modes is detailed in Appendix B.

We can determine the systems eigenfrequencies, i.e., modes that are up to loss time-independent, by solving the resonance condition

$$1 = \frac{g^2}{\omega} \sum_{j=-J}^{J} \frac{1}{\omega - j\,\omega_{\mathrm{FSR}} - \Delta_a}. \tag{1.17}$$

Here ω corresponds to an eigenfrequency of Eq. (1.16), the new positions of the resonator modes of the coupled system and $j \in \mathbb{N}$ is the resonance's mode-number. This equation has $2(J+1)$ solutions and for the case of multimode strong coupling, where $g \gg \omega_{\mathrm{FSR}}$, the new eigenfrequencies of the coupled atom–resonator can be solved analytically to be

$$\tilde{\omega}_j = \omega_j + \frac{1}{2}\omega_{\mathrm{FSR}}. \tag{1.18}$$

As one can see here, in this limiting case of extreme coupling, the resonances are maximally shifted with respect to the uncoupled resonator by $\omega_{\mathrm{FSR}}/2$, where the observed splitting saturates. Note that the single-mode Jaynes- and Tavis-Cummings model do not feature such a limit for the normal-mode splitting.

1.3 Experimentally realized atom–resonator interaction - strong coupling regime

While the Jaynes- and Tavis-Cummings model describe idealized closed systems, where atoms only interact with a single field mode, in an actual experimental implementation, there are several dissipative channels coupling the system to the environment. This influence of the resonator's properties on the light–matter interaction can be quantified by the Purcell factor [5], given by

$$C = \frac{3}{4\pi^2}\left(\frac{\lambda}{n}\right)^3 \frac{Q}{V_0}, \tag{1.19}$$

describing the increase of probability for an emitter to spontaneously emit a photon when put inside a cavity. This quantity, also referred to as cooperativity, shows that in order to increase the light–matter interaction, it is required to minimize its mode volume while keeping the quality-factor very high, hence keep losses low. By doing so, many experimental setups could be implemented exploring single-atom strong coupling, see for examples [9, 49, 50].

Loss channels in a cavity For an actual experimental implementation of a resonator, we can identify several loss channels for light out of the system, as depicted in Fig. 1.4. First, there are losses from the cavity implementation, denoted as $\kappa = \kappa_0 + \kappa_{\mathrm{ext}}$. Here, $2\kappa_0$ is the

Die approbierte gedruckte Originalversion dieser Dissertation ist an der TU Wien Bibliothek verfügbar.
The approved original version of this doctoral thesis is available in print at TU Wien Bibliothek.
TU Bibliothek WIEN Your knowledge hub

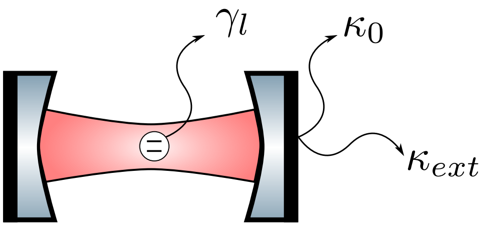

Fig. 1.4 Sketch of a FP resonator consisting of two mirrors and a two-level atom in the centre. The atom can scatter light into the single cavity mode (red) or into the surrounding environment with a scattering rate of γ_l. The mirrors can in principle scatter and absorb (κ_0) as well as transmit light (κ_{ext}).

intrinsic energy loss rate, quantifying the losses inside the resonator, due to imperfections of the mirrors or dielectrics inside the cavity causing absorption and scattering of photons. Furthermore, to excite or probe the resonator, an external and coherent field needs to be coupled to the cavity field. The coupling between the fields inside and outside the resonator is denoted as $2\kappa_{\text{ext}}$ and also leads to energy loss from the atom–cavity system. Second, the atom is not exclusivity coupling to the resonator mode, but also decays to the continuum of modes surrounding the cavity. This happens with a rate γ_l proportional to the spontaneous decay rate of an atom, given by $\gamma = \omega^3 d^2 / 6\pi\varepsilon_0 \hbar c^3$ [51].

1.3.1 Strong coupling regime

Typically, a system in cQED is characterized by comparison of the introduced parameters γ and $\kappa = \kappa_0 + \kappa_{\text{ext}}$ to the coupling strength g. A special interest lays in the realization of strong coupling, where the energy exchange between the atom and the cavity field is much faster than any other dissipative process. In this regime, in a single-mode resonator, the system can be described well using the Jaynes- and Tavis-Cummings models. The strong coupling regime is defined by

$$g \gg (\kappa, \gamma). \tag{1.20}$$

Note that also the relation

$$C = \frac{g^2}{2\kappa\gamma} \gg 1 \tag{1.21}$$

is often used to characterize the ability to operate in the strong coupling regime. This condition, using the cooperativity to characterize the atom–resonator system, is mostly used equivalently to Eq. (1.20), but is not as strong of a restriction since only $g^2 \gg \kappa\gamma$.

1.3.2 Solution of an interfaced resonator

In a next step we want to calculate the expected spectral features of a probed, lossy cavity coupled to a single atom. There are several methods allowing us to do so, where the most common approach used to derive the dynamics in an open quantum system is making use of a master equation [52], shown for this system in Appendix A.

Here, we present instead an approach introduced in [38], where we analyse the photon transport through a waveguide that interfaces a cavity embedded with a two-level atom as shown in Fig. 1.5. Note that in the remainder of this thesis, this approach will be re-introduced and discussed in detail.

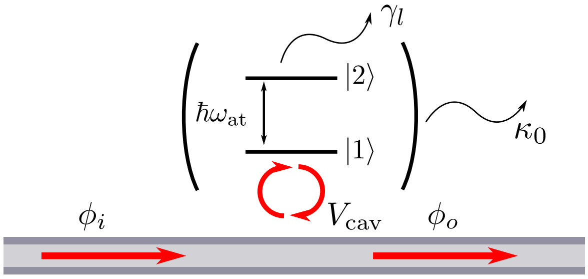

Fig. 1.5 For the photon transport approach a waveguide couples to the cavity including a single two-level atom, that is described by the Jaynes-Cummings model. The coupling waveguide is used to provide a weak excitation field ϕ_i, where we are interested in the spectral features of the probed cavity revealed in the outgoing light field ϕ_o.

According to the formalism in [38] the Hamiltonian of the coupled cavity with an embedded single atom is given by

$$
\begin{aligned}
\frac{\hat{H}}{\hbar} &= \hat{U}_{\text{probe}} + \frac{\hat{H}_{JC,l}}{\hbar} = \\
&\int_{-\infty}^{\infty} dx \left[\hat{c}^{\dagger}(x)(\omega_0 - i v_g \frac{\partial}{\partial x})\hat{c}(x) + V_{\text{cav}}\delta(x)\left(\hat{a}^{\dagger}\hat{c}(x) + \hat{a}\hat{c}^{\dagger}(x)\right)\right] \\
&+ (\omega_{\text{at}} - i\gamma_l)\hat{\sigma}_{+}\hat{\sigma}_{-} + (\omega_c - i\kappa_0)\hat{a}^{\dagger}\hat{a} + g\left(\hat{\sigma}_{+}\hat{a} + \hat{\sigma}_{-}\hat{a}^{\dagger}\right),
\end{aligned}
\tag{1.22}
$$

where $\hat{U}_{\text{probe}}$ describes the probing of the cavity with a waveguide and $\hat{H}_{JC,l}$ describes the atom–resonator interaction using a Jaynes-Cummings approach like Eq. (1.10). Note that here, we include loss channels into the description, such as spontaneous decay γ_l from the atom and an intrinsic loss rate of the cavity field κ_0. In the Hamiltonian, $\hat{c}^{\dagger}(x)$ $(\hat{c}(x))$ is the creation (annihilation) operator of a photon in the driving field, $\hat{a}^{\dagger}$ $(\hat{a})$ is the cavity photon creator (annihilator) operator, $\hat{\sigma}_{\pm}$ is the atomic raising (lowering) operator, $V_{\text{cav}} = \sqrt{2\kappa_{\text{ext}} v_g}$ is the coupling strength between the field in the cavity and the external driving field, v_g is the group velocity of light in the waveguide, ω_{at} is the atomic resonance frequency, and ω_c is the cavity resonance closest to atomic resonance.

To solve the eigenequation $H|\Psi\rangle = \varepsilon|\Psi\rangle$ in the steady state we make an ansatz for the wavefunction to be

$$
|\Psi\rangle = \left[\int dx \phi_{\text{c}}(x)\hat{c}^{\dagger}(x) + \phi_{\text{at}}\hat{\sigma}_{+} + \phi_{\text{cav}}\hat{a}^{\dagger}\right]|0\rangle,
\tag{1.23}
$$

where ϕ_c is the photon wave function of the probe field and ϕ_{at} and ϕ_{cav} are the excitation amplitudes of the cavity and the atom. For the driving field one can assume a plain wave, with output (input) amplitude ϕ_o (ϕ_i)

$$\phi_c(x) = \begin{cases} \phi_i \cdot e^{ikx} & x < 0 \\ \phi_o \cdot e^{ikx} & x \geq 0 \end{cases} \tag{1.24}$$

to arrive at a set of differential equations

$$\begin{aligned} \tilde{\Delta}_a \phi_{\text{at}} + g\phi_{cav} &= \varepsilon \phi_a \\ \tilde{\Delta}_c \phi_{cav} + g\phi_{\text{at}} + \frac{V_{\text{cav}}}{2}\left(\phi_i + \phi_0\right) &= \varepsilon \phi_{cav} \\ -iv_g\left(\phi_0 - \phi_i\right) + V_{\text{cav}}\phi_{cav} &= \varepsilon \cdot \phi_i(x), \end{aligned} \tag{1.25}$$

where we substituted

$$\begin{aligned} \tilde{\Delta}_a &= (\omega_{\text{at}} - \omega - i\gamma_l) \\ \tilde{\Delta}_c &= (\omega_c - \omega - i\kappa_0). \end{aligned} \tag{1.26}$$

We can now derive the steady state values of the output amplitude ϕ_o as a function of the incoming amplitude ϕ_i to be

$$\frac{\phi_o}{\phi_i} = \frac{g^2 + (\gamma_l + i\Delta_a)\left(\kappa_0 - \kappa_{\text{ext}} + i\Delta_c\right)}{g^2 + (\gamma_l + i\Delta_a)\left(\kappa_0 + \kappa_{\text{ext}} + i\Delta_c\right)}, \tag{1.27}$$

as well as the excitation amplitudes for the cavity field ϕ_{cav} and the atom ϕ_{at}

$$\begin{aligned} \frac{\phi_{\text{cav}}}{\phi_i} &= \frac{-i\sqrt{2v_g\kappa_{\text{ext}}}(\gamma_l + i\Delta_a)}{g^2 + (\gamma_l + i\Delta_a)(\kappa_0 + \kappa_{\text{ext}} + i\Delta_c)} \\ \frac{\phi_{\text{at}}}{\phi_i} &= \frac{-g\sqrt{2v_g\kappa_{\text{ext}}}}{g^2 + (\gamma_l + i\Delta_a)(\kappa_0 + \kappa_{\text{ext}} + i\Delta_c)}. \end{aligned} \tag{1.28}$$

The spectral response of the system when exciting via ϕ_i, given by Eq. (1.27), is plotted in Fig. 1.3(a), for the resonant case $\Delta_a = \Delta_c$. While the empty resonator (dotted black line) shows a resonance at zero detuning, the coupled system (red line) shows a split resonance, with a splitting of $\Omega = 2g$. As a comparison, the spectrum that was calculated using the Jaynes-Cummings model is shown in Fig. 1.3(b), where the lifted degeneration of the energy levels of the dressed states in the coupled atom-light system is shown.

An important quantity, that can be derived using this formalism describing a probed, coupled resonator is the excited state population per cavity photon $\left|\frac{\phi_{\text{at}}}{\phi_{\text{cav}}}\right|^2 = \frac{g^2}{\gamma_l^2 + \Delta_a^2}$. With this, the atom-induced dampening of the cavity field on resonance, used in the next chapter to define a scope for the validity of the Jaynes-Cummings model, can be defined as

$$\left|\frac{\phi_{\text{at}}}{\phi_{\text{cav}}}\right|^2 \gamma_l = \frac{g^2}{\gamma_l}. \tag{1.29}$$

1.4 Nanofiber resonators - length independent cooperativity

Ultimately, I would like to discuss a particular implementation of cavities, built around an optical nanofiber. A nanofiber is a tapered optical glass fiber, allowing for an almost lossless transition into a waist region of sub-wavelength diameter. This geometry provides very strong transverse confinement of the guided light, which can couple effectively to emitters in close vicinity of the fiber surface (details in chapter 3). Both types of resonators, ring resonators and Fabry-Pérot cavities, can be fabricated composed entirely of optical waveguide featuring an optical nanofiber section, as depicted in Fig. 1.6. Such cavity implementations utilize for instance fiber integrated beam splitters facilitating a fiber ring resonator [53–55], or imprints of index modulation in or around the waist of a nanofiber creating Bragg mirrors [56–58].

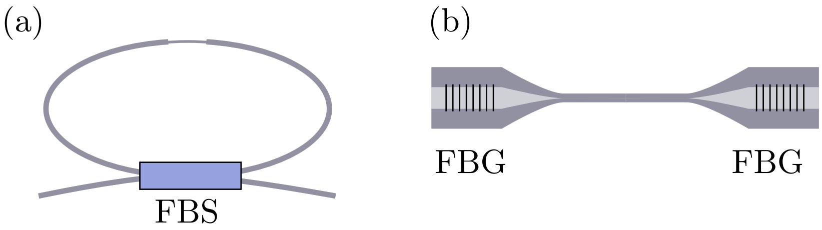

Fig. 1.6 (a) Sketch of a fiber ring resonator with an integrated nanofiber (indicated as thinner fiber section) using a fiber beamsplitter (FBS). (b) Sketch of an optical nanofiber with imprinted fiber Bragg gratings (FBG).

The cooperativity of nanofiber-based resonators interfacing a single atom (see Eq. (1.19) and [59]), is given by

$$C = \frac{4}{\pi}\left(\frac{\sigma_{\mathrm{at}}}{A_{\mathrm{eff}}}\right)F = \frac{4}{\pi}\sigma_{\mathrm{at}}\left(\frac{F L_{\mathrm{opt}}}{V_0}\right), \tag{1.30}$$

with $\sigma_{\mathrm{at}} = \frac{3\lambda^2}{2\pi}$ being the single atom absorption cross-section. Note that here, the finesse F represents the longitudinal confinement of light in the cavity and the transverse confinement of light is given by the ratio $\frac{\sigma_{\mathrm{at}}}{A_{\mathrm{eff}}}$, with A_{eff} being the effective mode area of guided light in the nanofiber section. This shows that the longitudinal and transverse mode confinements in these resonators can be treated independently from each other, thus the cooperativity must be cavity-length independent.

This can be understood, when comparing nanofiber-based resonators to conventional mirror cavities. Typically, to generate stable resonance conditions and allow high field intensities at the position of the atom, concave mirrors are used to form a resonator. By doing so, the field mode has a waist in the centre of the cavity given by the curvature and the spacing between the mirrors (see for instance [60]). The waist diameter of a mode in a conventional cavity changes drastically with its length L_{opt}, while the mode area of a fiber guided light in a cavity remains the same and the mode volume grows only as $V \propto L_{\mathrm{opt}}$.

Furthermore, in a nanofiber-based resonator, when neglecting cumulative roundtrip losses, e.g., absorption of light inside the fiber, the coupling strength scales as $g \propto 1/\sqrt{L_{\text{opt}}}$. At the same time, the intrinsic losses can be determined to be $\kappa \propto 1/L_{\text{opt}}$, while the spontaneous atomic decay rate remains constant. With this we can say $\frac{g}{\kappa} \propto \sqrt{L_{\text{opt}}}$ and $\frac{g}{\gamma} \propto \sqrt{1/L_{\text{opt}}}$, hence (see [61] for details)

$$C = \frac{g^2}{2\kappa\gamma} = \text{const.} \tag{1.31}$$

This important particularity of nanofiber-based resonators forms the basis of our experiment, where the cavity parameters scale as

$$\begin{aligned} \nu_{\text{FSR}} &\propto 1/L_{\text{opt}} \\ g &\propto 1/\sqrt{L_{\text{opt}}}, \end{aligned} \tag{1.32}$$

such that, there is a length L_{opt}, where the coupling strength exceeds the free spectral range $g > \nu_{\text{FSR}}$, as shown in Fig. 1.7 and explained in detail in [54]. If in that case $C_N \gg 1$ is fulfilled this regime is coined as multimode strong coupling regime (sometimes superstrong coupling regime [34]), where the atoms simultaneously couple to many longitudinal resonator modes.

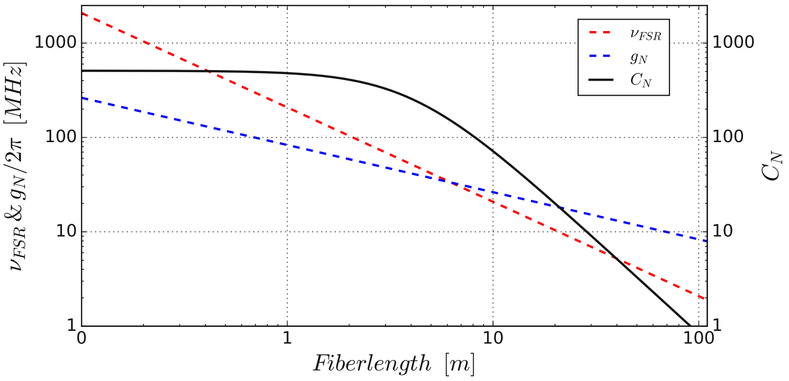

Fig. 1.7 Length dependency of collective coupling strength g_N (blue dashed line), cooperativity C_N (black solid line) and free spectral range ν_{FSR} (red dashed line) of a fiber ring resonator including an optical nanofiber. For the plot, coupling of 2000 atoms in a two-colour dipole trap that traps the atoms 200 nm above the nanofiber surface was assumed, as shown in [23]. For this realization, the single-atom coupling strength was estimated to be $g_0 = 2\pi \times 1.5$ MHz for a resonator of finesse $F = 40$. The figure shows that the cooperativity is length independent until the propagation losses for light in the fiber ring become substantial (assumed here 1.5 dB/km). Once the collective coupling strength g_N exceeds ν_{FSR}, the resonator reaches the multimode strong coupling regime.

Chapter 2

Cascaded interaction approach

In the past chapter we introduced the commonly used and very successfully applied Jaynes-Cummings [10] and Tavis-Cummings [12] models quantifying the interaction of light and matter with a single mode of an electro-magnetic field in a cavity. When implementing the experiment presented in this thesis, our observations underlined that the Jaynes- and Tavis-Cummings model with their used approximations cannot be applied successfully to describe our measured transmission spectra and an alternative description was required.

In this chapter, I will discuss the limits to the validity of the established models, and I will introduce a real-space formalism based on [37–39] to mitigate the underlying assumptions of Jaynes-Cummings and Tavis-Cummings. In our approach, we utilize photon transport to consider a successive single-atom interaction of atoms coupled to the cavity field. Moreover, we explicitly consider a position dependent cavity field $\hat{a}^\dagger(x)$, allowing to take into account the modification of the field after interacting with an optically dense atomic ensemble. Furthermore, this way, our method naturally supports arbitrarily many longitudinal resonator modes coupling to the ensemble allowing us to also model multimode strong coupling.

I will derive the expected spectrum of our system and show that in the limits of low optical density or small finesse our model reduces to well-known waveguide and cavity QED, allowing to connect these two fields. In the remainder of this chapter, I will discuss the exceedingly different behaviour of our model compared to the predictions of Tavis-Cummings once the identified limits to the coupling strength g_N are surpassed, such as the emergence of new resonator modes.

2.1 Limits of conventional cQED models

The Jaynes- and Tavis-Cummings model are well established theories to describe the interaction between light and matter in a cavity and have been shown to successfully fit the observations of most experimental implementations in cQED.

Nevertheless, one needs to be aware of underlying approximations and limits of these approaches that can lead to significant derivations between theory and observation. One implicit assumption to both models is the instantaneous interaction between the cavity field and the emitters. In other words, all time scales, i.e., loss and coupling rates must be slow compared to the photon roundtrip time $\tau = 1/\nu_{\mathrm{FSR}}$. This is fulfilled for most experimentally realized systems, since they specifically use tiny mode volumes, realized through short cavity lengths in order to increase the single-atom coupling strength g_1 (see 1.3). Thus, they feature large free spectral ranges, for which both assumptions, instantaneous and single-mode interaction, are fulfilled. In this sense, the free spectral range is usually solely used to describe the experimental realization of the cavity.

However, we may expect deviations from the established Tavis-Cummings model when working with large atom numbers N, where the single roundtrip losses become substantial. Excessive absorption of the atomic ensemble will lead to a perturbed cavity field even after a single pass. Furthermore, increasing N will lead to a large collective Rabi frequency $\Omega = 2\sqrt{N}g_1$, eventually exceeding ν_{FSR}. This becomes especially important when working with resonators of exceptionally small ν_{FSR}, such as our fiber ring resonators.

In order to define a regime for the validity of the Tavis-Cummings model, we have to compare two characteristic frequencies of the atom–resonator system to the free spectral range. Firstly, as introduced in chapter 1, the rate of atom-induced energy loss rate of the system, given by g_N^2/γ_l needs to be much smaller than the free spectral range in order to guarantee an unperturbed cavity field after a single roundtrip. Secondly, we already introduced the possibility of coupling strengths coming of the order of the free spectral range, where in this regime the atomic ensemble can simultaneously couple to several longitudinal modes of the resonator at the same time. Thus, we can formulate restrictions for the Tavis-Cummings Hamiltonian to apply, given by

$$\begin{aligned} \frac{g_N^2}{\gamma_l} &\ll \nu_{\mathrm{FSR}} \\ g_N &\ll \nu_{\mathrm{FSR}}. \end{aligned} \tag{2.1}$$

The main objective of the following theoretical discussion is the introduction of an approach typical in waveguide QED into the description of cQED. While doing so, we will identify a direct relation between the channelling efficiency β, the fraction of photons being emitted into a preferred mode, and the coupling strength g_N, given for a ring resonator by

$$g_N^2 = 2\beta\gamma N\nu_{\mathrm{FSR}}. \tag{2.2}$$

With this quantity we can reformulate the conditions in Eq. (2.1) to be

$$\begin{aligned} \beta N &\ll \frac{1}{2}(1-\beta) \\ \beta N &\ll \frac{1}{2}\frac{\nu_{\mathrm{FSR}}}{\gamma}. \end{aligned} \tag{2.3}$$

For $\beta \ll 1$, a situation realized in most experimental setups, the first condition in Eq. (2.3) reduces to $\beta N \ll 1/2$. With the definition for the resonant single-pass optical density for an atomic ensemble $\mathrm{OD} = 4\beta N$, we see that the Tavis-Cummings model can only be valid as long as $\mathrm{OD} \ll 2$, a condition that is easily experimentally violated. More strikingly, as a consequence of Eq. (2.3), a Jaynes-Cummings approach describing single-atom strong coupling in a ring resonator featuring loss is only valid as long as

$$\beta \ll 1/3. \tag{2.4}$$

As an example, I would like to discuss the case of single atom strong coupling, assuming the case, where the atom near perfectly couples to the waveguide, $\beta \approx 1$. For such a case to be implemented, it would require a cavity with essentially no dissipation into non-cavity modes, i.e., $\gamma_l = (1-\beta)\gamma \to 0$. This could, e.g., be realized with a hollow sphere with the atom in its centre. In this scenario the cooperativity approaches infinity

$$C = \frac{g_{\mathrm{max}}^2}{(\kappa_0 + \kappa_{\mathrm{ext}})\gamma_l} \to \infty, \tag{2.5}$$

although $g_{\mathrm{max}} = \sqrt{2\gamma \nu_{\mathrm{FSR}}}$, the maximum coupling strength given for a single atom, is limited. At the same time, we get for the atom-induced energy loss rate $g^2/\gamma_l \to \infty$. This suggests that the description of the Jaynes-Cummings model for a probed single-mode resonator (Eq. (1.27)) becomes inaccurate as soon $\beta \ll 1/3$ is violated and an alternative description for this scenario must be used.

2.2 Cascaded interaction approach

The theoretical basis of our approach to model the transmission of light through our system was introduced by [37–39]. In these references a method for photon propagation in position space is used to calculate the single-photon transport in a single-mode waveguide, that is coupled to an atom-cavity system. Thereby, several applications are being discussed, such as calculating the transmission through the waveguide when coupled to a Fabry-Pérot cavity or a whispering-gallery resonator, each with an embedded single atom. Nevertheless, this approach only considers the propagation of a photon in the coupling waveguide, where the cavity–atom interaction is described by the Jaynes-Cummings Hamiltonian, an approach not suitable to accurately describe our long ring resonators. Thus, we will adapt this photon propagation method and apply it to the cavity field as well.

2.2.1 General approach

In this section we derive a general Hamiltonian modelling light propagating in a ring resonator coupled to an ensemble of atoms, as shown in Fig. 2.1. Making use of the approach in [37–39], we first formulate the Hamiltonians for propagating photons in the coupling waveguide

Die approbierte gedruckte Originalversion dieser Dissertation ist an der TU Wien Bibliothek verfügbar.
The approved original version of this doctoral thesis is available in print at TU Wien Bibliothek.
TU Bibliothek WIEN Your knowledge hub

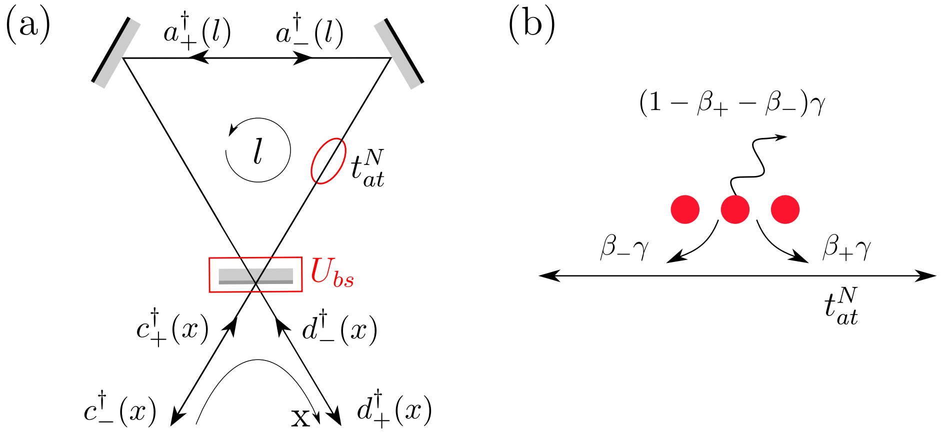

Fig. 2.1 (a) Sketch of a ring cavity coupled to atoms via t_{at} (indicated in red). The cavity can be excited by incoming light $\hat{c}_+^\dagger(x)$ ($\hat{d}_-^\dagger(x)$) and the corresponding output is given by $\hat{d}_+^\dagger(x)$ ($\hat{c}_-^\dagger(x)$), where the coupling waveguide modes are $\hat{c}_\pm^\dagger(x)$ for $x<0$ and $\hat{d}_\pm^\dagger(x)$ for $x>0$. The light is coupled to the resonator via a beamsplitter $\hat{U}_{bs}$ at position $x=0$. Inside the resonator we consider the counter-clockwise (CCW) $\hat{a}_+^\dagger(l)$ and clockwise (CW) $\hat{a}_-^\dagger(l)$ propagating light fields. The positions in the resonator are indicated by the coordinate l, where at the beamsplitter $l=0=L$. (b) Atoms can couple to the resonator mode $\hat{a}_\pm^\dagger(l)$ with their corresponding coupling rates $\beta_\pm\gamma$ into CW and CCW direction, respectively.

and inside the cavity to be

$$\begin{aligned}\frac{\hat{H}_{wg}}{\hbar} &= \sum_k \omega_k \hat{c}_k^\dagger \hat{c}_k + \sum_k \omega_k \hat{d}_k^\dagger \hat{d}_k \\ \frac{\hat{H}_{cav}}{\hbar} &= \sum_k \omega_k \hat{a}_k^\dagger \hat{a}_k,\end{aligned} \tag{2.6}$$

where $\hat{c}_k^\dagger$ ($\hat{c}_k$) is the creation (annihilation) operator of a photon with wavevector k used to describe the probing light field for $x<0$ and the operator $\hat{d}_k^\dagger$ ($\hat{d}_k$) is used equivalently for light at $x>0$. Furthermore, new to this approach, we introduce a propagating light field inside the cavity, indicated as $\hat{a}_k^\dagger$ ($\hat{a}_k$).

In the next step, we split each light field into right and left propagation, shown for the example of $\hat{c}_k^\dagger$

$$\frac{\hat{H}_{\hat{c}}}{\hbar} = \sum_k \omega_k \hat{c}_k^\dagger \hat{c}_k = \sum_{k+} \omega_+ \hat{c}_{k+}^\dagger \hat{c}_{k+} + \sum_{k-} \omega_- \hat{c}_{k-}^\dagger \hat{c}_{k-}. \tag{2.7}$$

We now transfer Eq. (2.7) into position space by approximating the light's linear dispersion relation as linear around the interesting frequency ω_0 as $\omega_{k\pm} = \omega_0 + v_g(k \pm k_0)$, where v_g is the group velocity in the medium and $\pm k_0$ the corresponding wavenumber. With this we can

Fourier-transform the propagating light fields and the real-space Hamiltonian $\hat{H}_{\hat{c}}$ reads

$$\frac{\hat{H}_{\hat{c}}}{\hbar} = \int_{-\infty}^{0} dx \hat{c}_{+}^{\dagger}(x)\left(\omega_0 - i v_g \frac{\partial}{\partial x}\right)\hat{c}_{+}(x) + \hat{c}_{-}^{\dagger}(x)\left(\omega_0 + i v_g \frac{\partial}{\partial x}\right)\hat{c}_{-}(x). \tag{2.8}$$

In the example given here, the operator $\hat{c}_{+}^{\dagger}(x)$ creates a right-propagating photon at position x for $x < 0$.

Exactly the same transformation is applied to $\hat{d}_k^{\dagger}$ and the cavity field $\hat{a}_k^{\dagger}$, but for the resonator, instead of left and right moving photons we talk about two counter-propagating modes, clockwise (CW) and counter-clockwise (CCW). Furthermore, the group velocity inside the cavity v_c can in principle be different than v_g for the probing field. Now, the operator $\hat{a}_{-}^{\dagger}(l)$ ($\hat{a}_{+}^{\dagger}(l)$) creates a photon propagating in CW (CCW) direction at position l inside the cavity with frequency ω.

After the Hamiltonians of the light fields are known, in the next step we have to consider the coupling of atoms to the resonator field as depicted in Fig. 2.1(b). For this, we assume that each excited atom has a total population decay rate 2γ, where the partial decay rates into the CCW (CW) modes are $\beta_{\pm}\gamma$. As a consequence, the atom decays to the continuum of surrounding vacuum modes with the rate $(1-\beta_{+}-\beta_{-})\gamma = \gamma_l$, which we implement as a loss term $-i\gamma_l$ in the Hamiltonian. The atomic energy term including loss is therefore given by

$$\frac{\hat{H}_{at}}{\hbar} = \sum_{n=1}^{N} \hat{\sigma}_n^{+}\hat{\sigma}_n^{-}\left(\omega_{\mathrm{at}} - i\gamma_l\right), \tag{2.9}$$

where $\hbar\omega_{\mathrm{at}}$ is the atomic excitation energy and $\hat{\sigma}_n^{+}$ ($\hat{\sigma}_n^{-}$) is the raising (lowering) operator of the n-th two-level atom. The interaction between the atoms and the cavity field can be modelled analogue to the interaction term in the Jaynes-Cummings approach in Eq. (1.10), using the real space operators $\hat{a}_{\pm}^{\dagger}(l)$, and is given by

$$\frac{\hat{H}_{int}}{\hbar} = \sum_{n=1}^{N}\int_{0}^{L}\left[\delta\left(l-l_n\right)V_{n,+}\left(\hat{\sigma}_n^{+}\hat{a}_{+}(l) + \hat{\sigma}_n^{-}\hat{a}_{+}^{\dagger}(l)\right) + \delta\left(l-l_n\right)V_{n,-}\left(\hat{\sigma}_n^{+}\hat{a}_{-}(l) + \hat{\sigma}_n^{-}\hat{a}_{-}^{\dagger}(l)\right)\right]. \tag{2.10}$$

Here, $V_{n,\pm}$ is the direction dependent coupling strength between the n-th atom and the field at position l_n. Note that the model in principle allows for the atoms to be coupled symmetrically $V_{n,+} = V_{n,-}$, asymmetrically $V_{n,+} \neq V_{n,-}$ or fully chirally $V_{n,\pm} = 0, V_{n,\mp} > 0$, where the atoms exclusively interact with one of the CW or CCW modes.

In a last step, we need to model the coupling between the external light fields $\hat{c}_{\pm}^{\dagger}(x)$, $\hat{d}_{\pm}^{\dagger}(x)$ to the cavity field $\hat{a}_{\pm}^{\dagger}(l)$. This can be done by introducing a unitary operator $\hat{U}_{bs}$ that corresponds to the implementation of a beamsplitter or low-reflectivity mirror. To this end, we formulate the beamsplitter matrix

$$\hat{U}_{bs} = t_{\mathrm{rt}}\left(i v_c t_1 \hat{a}(L)\hat{a}^{\dagger}(0) + \sqrt{v_c v_g}\, t_2 \hat{a}(L)\hat{d}^{\dagger}(0)\right) + i v_g t_1 \hat{c}(0)\hat{d}^{\dagger}(0) + \sqrt{v_g v_c}\, t_2 \hat{c}(0)\hat{a}^{\dagger}(0), \tag{2.11}$$

where t_1 and t_2 are the amplitude reflection and transmission trough the beamsplitter, as depicted in Fig. 2.2(a). These transmission quantities can be related to standard cQED parameters as shown in Appendix C to be

$$\begin{aligned} t_1 &= \sqrt{1-\frac{2\kappa_{\text{ext}}}{\nu_{\text{FSR}}}}, \; t_2 = \sqrt{\frac{2\kappa_{\text{ext}}}{\nu_{\text{FSR}}}} \\ t_{\text{rt}} &= \sqrt{1-\frac{2\kappa_0}{\nu_{\text{FSR}}}} = \sqrt{1-\frac{\pi}{F}} = \sqrt{1-L_{\text{tot}}}, \end{aligned} \tag{2.12}$$

where, $2\kappa_{\text{ext}}$ is the energy coupling rate of the probing field to the resonator field and $2\kappa_0$ is the resonator's intrinsic energy loss rate. In this way, including the factor t_{rt} in the definition of $\hat{U}_{bs}$, we are enabled to consider any losses in the cavity arm of the beamsplitter, such as scattering, absorption or in the case of a fiber ring resonator, losses induced by bending the fiber and fiber splices.

Finally, the real-space Hamiltonian that describes a ring resonator coupled to an ensemble of atoms is the sum of the individual Hamiltonians introduced before $\hat{H} = \hat{H}_{wg} + \hat{H}_{cav} + \hat{H}_{at} + \hat{H}_{int} + \hat{U}_{bs}$ and is given by

$$\begin{aligned} \frac{\hat{H}}{\hbar} = & \int_{-\infty}^{0} dx \left[\hat{c}_+^\dagger(x) \left(\omega_0 - i v_g \frac{\partial}{\partial x} \right) \hat{c}_+(x) + \hat{c}_-^\dagger(x) \left(\omega_0 + i v_g \frac{\partial}{\partial x} \right) \hat{c}_-(x) \right] + \\ & \int_{0}^{+\infty} dx \left[\hat{d}_+^\dagger(x) \left(\omega_0 - i v_g \frac{\partial}{\partial x} \right) \hat{d}_+(x) + \hat{d}_-^\dagger(x) \left(\omega_0 + i v_g \frac{\partial}{\partial x} \right) \hat{d}_-(x) \right] + \\ & \int_{0}^{L} dl \left\{ \hat{a}_+^\dagger(l) \left(\omega_0 + i v_c \frac{\partial}{\partial l} \right) \hat{a}_+(l) + \hat{a}_-^\dagger(l) \left(\omega_0 - i v_c \frac{\partial}{\partial l} \right) \hat{a}_-(l) + \right. \\ & \sum_{n=1}^{N} \left[\delta(l) \hat{\sigma}_n^+ \hat{\sigma}_n^- \left(\omega_{\text{at}} - i \left(1 - \beta_+ - \beta_- \right) \gamma \right) + \delta\left(l - l_n \right) V_{n,+} \left(\hat{\sigma}_n^+ \hat{a}_+(l) + \hat{\sigma}_n^- \hat{a}_+^\dagger(l) \right) \right. \\ & \left. \left. + \; \delta\left(l - l_n \right) V_{n,-} \left(\hat{\sigma}_n^+ \hat{a}_-(l) + \hat{\sigma}_n^- \hat{a}_-^\dagger(l) \right) \right] \right\} + \hat{U}_{bs}. \end{aligned} \tag{2.13}$$

Note that for this derivation a few approximations are implicitly applied. At first, for describing the interaction between light and atoms coupled to the resonator in $\hat{H}_{int}$ (Eq. (2.10)), we applied a rotating wave and dipole approximation. Secondly, we consider only one transverse cavity mode and, for simplicity in the following discussion, we assume $\beta_\pm$ to be the same for each atom. This approximation is justified as long as the variation of $\beta_{n,\pm}$ around a mean value β is small (see also Appendix D).

2.2.2 Chiral light–matter coupling

In the implemented experiment, the ring resonator consists entirely of an optical fiber, where the atom–resonator coupling is mediated via the evanescent field of a running wave guided on the outside of an optical nanofiber integrated into the resonator, see Fig. 2.2. We probe the system through a waveguide, using an optical fiber coupled to the resonator via an in-fiber

Die approbierte gedruckte Originalversion dieser Dissertation ist an der TU Wien Bibliothek verfügbar.
The approved original version of this doctoral thesis is available in print at TU Wien Bibliothek.
TU Bibliothek Your knowledge hub WIEN

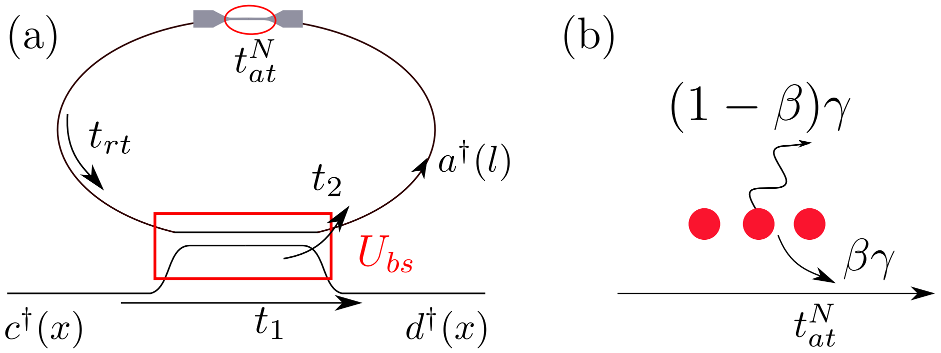

Fig. 2.2 (a) Schematic of our experiment, where only the forward propagating modes $\hat{c}^\dagger(x)$ ($x \leq 0$) and $\hat{d}^\dagger(x)$ ($x > 0$) couple to the resonator via a beamsplitter $\hat{U}_{bs}$. Due to chiral light–matter interaction, the only cavity mode that interacts with the atoms is the CCW mode, as indicated in (b). To consider coupling and loss in our setup, we define t_1, t_2 as transmissions through the beamsplitter and t_{rt} as loss inside the resonator.

beamsplitter, where the only input photons are generated via $\hat{c}_+^\dagger(x)$. Consequently, inside the empty resonator we only launch the counter-clockwise propagating mode $\hat{a}_+^\dagger(l)$. In this situation, the atoms exhibit chiral light–matter interaction [33, 62], such that atoms will emit much more in forward than in backward direction, i.e., $\beta_+ \gg \beta_-$. Note that even when this situation of chiral light-matter coupling is not perfectly realized in our system, as soon as we couple to many atoms a collective enhancement of coupling $g_N = \sqrt{N} g_1$ builds up along the direction the ensemble is probed. Scattering in opposite direction is typically small and can be treated as loss and does not affect the forward transmission [63]. Consequently, of these assumptions, we can re-formulate the Hamiltonian for the case of chiral light–matter interaction and obtain

$$\begin{aligned}\frac{\hat{H}}{\hbar} = &\int_{-\infty}^{0} dx \hat{c}^\dagger(x) \left(\omega_0 - i v_g \frac{\partial}{\partial x}\right) \hat{c}(x) + \int_{0}^{+\infty} dx \hat{d}^\dagger(x) \left(\omega_0 - i v_g \frac{\partial}{\partial x}\right) \hat{d}(x) + \\ &\int_0^L dl \left\{ \hat{a}^\dagger(l) \left(\omega_0 + i v_c \frac{\partial}{\partial l}\right) \hat{a}(l) + \sum_{n=1}^{N} \left[\delta(l) \hat{\sigma}_n^+ \hat{\sigma}_n^- \left(\omega_{\mathrm{at}} - i(1-\beta)\gamma\right) + \right.\right. \\ &\left.\left. \delta(l - l_n) V_{\mathrm{at}} (\hat{\sigma}_n^+ \hat{a}(l) + \hat{\sigma}_n^- \hat{a}^\dagger(l)) \right] \right\} + \hat{U}_{bs}.\end{aligned} \tag{2.14}$$

2.3 Solutions to the chiral interaction approach

In the next step we want to solve the Hamiltonian describing the chiral light–matter interaction for the steady state case. This can be done by solving the time-independent Schrödinger equation $\hat{H}|\Psi\rangle = \varepsilon|\Psi\rangle$ for the system's eigenenergy ε. For a single-photon input state we can make an ansatz for the general wavefunction

$$|\Psi\rangle = \left[\int_{-\infty}^{0} dx \phi_c(x) \hat{c}^\dagger(x) + \int_{0}^{+\infty} dx \phi_d(x) \hat{d}^\dagger(x) + \int_0^L dl \phi_a(l) \hat{a}^\dagger(l) + \sum_{n=1}^{N} \phi_{\mathrm{at},n} \hat{\sigma}_n^+ \right] |0\rangle. \tag{2.15}$$

The propagating photon fields for the light in the coupling waveguide for the steady state are assumed to be plane waves, given by

$$\begin{aligned} \phi_c(x) &= \phi_c e^{ikx} \Theta(-x) \\ \phi_d(x) &= \phi_d e^{ikx} \Theta(x) \end{aligned} \tag{2.16}$$

and the photon field inside the resonator

$$\phi_a(l) = e^{-ikl} \sum_{n=0}^{N} \phi_n \Theta(l - l_n) \Theta(l_{n+1} - l) \tag{2.17}$$

for the CCW propagating cavity field, where $l_0 = 0$ and $l_{N+1} = L$. Note that the atoms are coupled to the resonator at positions $l = l_n$, where the atomic excitation amplitude is $\phi_{\mathrm{at},n}$ and the fields after the n-th atom are given by ϕ_n, separated accordingly via Θ Heavyside step functions. Note that for the implementation of a fiber ring resonator we can assume the same group velocity for light in the resonator and the coupling fiber $v_g = v_c$.

Applying the general wavefunction to the Hamiltonian and comparing coefficients in front of the operators $\hat{d}^\dagger(0), \hat{a}^\dagger(0), \hat{a}^\dagger(l_n), \hat{\sigma}_n^+$, we obtain the following set of eigenequations, as derived in detail in Appendix D:

$$\begin{aligned} \hat{d}^\dagger(0): &\quad 0 = -iv_g \frac{\phi_d}{2} - v_g t_{\mathrm{rt}} t_2 \frac{\phi_N}{2} e^{-ikL} + iv_g t_1 \frac{\phi_c}{2} \\ \hat{a}^\dagger(0): &\quad 0 = iv_g \frac{\phi_0}{2} - iv_g t_{\mathrm{rt}} t_1 \frac{\phi_N}{2} e^{-ikL} + v_g t_2 \frac{\phi_c}{2} \\ \hat{a}^\dagger(l_n): &\quad 0 = -iv_g \left(\phi_n - \phi_{n-1}\right) e^{-ikl_n} + V_{\mathrm{at}} \phi_{\mathrm{at},n} \\ \hat{\sigma}_n^+: &\quad 0 = V_{\mathrm{at}}/2 \left(\phi_n + \phi_{n-1}\right) e^{-ikl_n} + \left(\omega_{\mathrm{at}} - i\gamma_l - \omega\right) \phi_{\mathrm{at},n} \end{aligned} \tag{2.18}$$

Coupling strength In this photon transport approach, the coupling between the atoms and the propagating resonator field is given by $V_{\mathrm{at}} = \sqrt{2\beta\gamma v_g}$. This definition of V_{at} in our model is consistent with the coupling strength g in the Jaynes-Cummings model, where we can identify $V_{\mathrm{at}}^2/L = g^2$, where both terms have the same unit as frequency. This relation can be motivated when calculating the mean number of photons $\langle\hat{n}\rangle$ inside the resonator. For the case of the Jaynes-Cummings approach, we can define $\langle\hat{a}^\dagger\hat{a}\rangle = \langle\hat{n}\rangle$, and for our waveguide approach $\langle\int_0^L dl\, \hat{a}(l)^\dagger \hat{a}(l)\rangle = \langle\hat{n}\rangle$, thus, leading to $V_{\mathrm{at}}^2/L = g^2$. For more details see Appendix E. Moreover, this relation allows us to directly compare coupling strengths in both models via the relation

$$g^2 = 2\beta\gamma\nu_{\mathrm{FSR}}. \tag{2.19}$$

Die approbierte gedruckte Originalversion dieser Dissertation ist an der TU Wien Bibliothek verfügbar.
The approved original version of this doctoral thesis is available in print at TU Wien Bibliothek.
TU Bibliothek WIEN Your knowledge hub

Solutions In the last step, we solve the set of equations (2.18) and use $V_{\mathrm{at}} = \sqrt{2\beta\gamma v_g}$ to obtain for the cavity fields

$$\begin{aligned} \frac{\phi_n}{\phi_{n-1}} &= 1 - \frac{2\beta\gamma}{\gamma + i\Delta_a} = t_{\mathrm{at}} \quad n \neq 0 \\ \frac{\phi_0}{\phi_c} &= \frac{-it_2}{e^{-ikL}t_1 t_{\mathrm{at}}^N t_{\mathrm{rt}} - 1}, \end{aligned} \tag{2.20}$$

where we defined the probe-atom detuning $\Delta_a = \omega_{\mathrm{at}} - \omega$, and a single-pass atomic transmission of cavity light trough an atom t_{at}. The field at the output of the coupled fiber ring resonator is given by

$$\frac{\phi_d}{\phi_c} = \frac{t_{\mathrm{at}}^N t_{\mathrm{rt}} e^{-ikL} - t_1}{t_{\mathrm{at}}^N t_{\mathrm{rt}} t_1 e^{-ikL} - 1}. \tag{2.21}$$

This equation can be re-formulated using $t_{\mathrm{at}}^N = t_N$ and $kL = \Delta_c/\nu_{\mathrm{FSR}}$ and we obtain a compact and intuitive equation for the transmission through a waveguide coupled to a ring resonator, given by

$$T = \left| \frac{e^{-i\Delta_c/\nu_{\mathrm{FSR}}} t_{\mathrm{rt}} t_N - t_1}{e^{-i\Delta_c/\nu_{\mathrm{FSR}}} t_{\mathrm{rt}} t_N t_1 - 1} \right|^2. \tag{2.22}$$

Here, Δ_c is the probe–cavity detuning that can in principle exceed several free spectral ranges $\Delta_c/2\pi\nu_{\mathrm{FSR}} > 1$. Thus, simultaneous coupling of the atomic ensemble to several resonator modes is implicitly included in this description. Furthermore, no assumptions restrict the value of channelling efficiency β or the number of coupled atoms N to make accurate predictions of the steady state of the probed system.

2.4 Interpretation and comparison of solutions

In this section I will first discuss our cascaded single-atom transmission approach by investigating the interaction between the guided light in a waveguide and an ensemble of atoms. Afterwards I will motivate the generality of our approach by showing how the solution in Eq. (2.22) can accurately model the case of an empty resonator and the case of a resonator with vanishing finesse capable of transitioning fully into a waveguide.

In the second, central part of this discussion I will compare the predictions for single atom and collective strong coupling of the Jaynes- and Tavis-Cummings model to our approach via stepwise violation of the conditions formulated in Eq. (2.1). To this end, I will present the most outstanding differences as well as cases for which both models can be merged.

2.4.1 Atoms coupled to a single propagating field

When looking at the set of solutions for the cavity fields in Eq. (2.20), we obtain the single-pass transmission of cavity light trough an atom t_{at}. In order to further motivate that this quantity describing the coupling between the atom and the cavity field is based on a typical waveguide QED description, we show specifically the case of coupling a single atom to a single propagating field of a waveguide, using the photon propagation approach to obtain the same quantity for the steady state solution. The corresponding Hamiltonian with an atom coupled at position $l = 0$ is then given by

$$\frac{\hat{H}}{\hbar} = \int_{-\infty}^{\infty} dl \left[\hat{a}^{\dagger}(l)(\omega_0 - i v_g \frac{\partial}{\partial l})\hat{a}(l) + V_{\text{at}}\delta(l)(\hat{\sigma}^{+}\hat{a}(l) + \hat{\sigma}^{-}\hat{a}^{\dagger}(l))\right] + \hat{\sigma}^{+}\hat{\sigma}^{-}(\omega_{\text{at}} - i\gamma_l). \tag{2.23}$$

For this scenario we use a single-excitation wavefunction ansatz Eq. (2.15) for $N = 1$, where we ignore the excitation field $\hat{c}^{\dagger}$ ($\hat{d}^{\dagger}$). When applied to the Schrödinger equation, we arrive again at a set of differential equations, similar to Eq.(2.18). Solving this set of equations, we obtain the steady state solution of the atomic excitation amplitude ϕ_{at} and output field ϕ_1, both as a function of the incoming field ϕ_0:

$$\begin{aligned} \frac{\phi_1}{\phi_0} &= \frac{(1-\beta)\gamma - \beta\gamma + i\Delta_a}{(1-\beta)\gamma + \beta\gamma + i\Delta_a} = 1 - \frac{2\beta\gamma}{\gamma + i\Delta_a} = t_{\text{at}} \\ \frac{\phi_{\text{at}}}{\phi_0} &= \frac{-iV_{\text{at}}}{(1-\beta)\gamma + \beta\gamma + i\Delta_a} = -\frac{i\sqrt{2\beta\gamma v_g}}{\gamma + i\Delta_a}. \end{aligned} \tag{2.24}$$

N-atom single-pass transmission With the definition of single-pass transmission of light interacting with a single atom $\phi_1/\phi_0 = t_{\text{at}}$, eventually, we can calculate the single-pass transmission for N atoms coupled to the waveguide. For large N we can approximate

$$t_N = \left(1 - \frac{2\beta\gamma N}{N(\gamma + i\Delta_a)}\right)^N \approx \exp\left(-\frac{2\beta\gamma N}{\gamma + i\Delta_a}\right), \tag{2.25}$$

such that the single-pass transmission through the coupled waveguide is given by

$$T_{\text{wg}} = |t_N|^2 = \exp(-4\beta N \frac{\gamma^2}{\gamma^2 + \Delta_a^2}) = \exp(-\text{OD}\frac{\gamma^2}{\gamma^2 + \Delta_a^2}), \tag{2.26}$$

where $OD = 4\beta N$ (for $\beta \ll 1$) is the single-pass optical density on resonance, describing the probe light transmission, known as Lambert–Beer's law [64].

Note that the collective interaction is considered as N individual single-atom contributions t_{at} altering the cavity field. Therefore, we call it a cascaded interaction between the cavity field and a chain of chirally coupled atoms. However, when instead considering symmetric coupling of atoms to the waveguide, the full Hamiltonian introduced in Eq. (2.13) requires numerical methods to be solved.

2.4.2 Empty resonator

In the next step, we look at an empty resonator, realized in our model by setting $t_{\text{at}} = 1$ or alternatively solving the set of eigenequations (2.18) for $V_{\text{at}} = 0$, where we arrive at

$$\begin{aligned} \frac{\phi_d}{\phi_c} &= \frac{t_{\text{rt}} e^{-ikL} - t_1}{t_{\text{rt}} t_1 e^{-ikL} - 1} \\ \frac{\phi_{\text{cav}}}{\phi_c} &= \frac{-it_2}{t_{\text{rt}} t_1 e^{-ikL} - 1}. \end{aligned} \tag{2.27}$$

The power transmission, assuming critical coupling, $\kappa_0 = \kappa_{\text{ext}}$, i.e., $t_{\text{rt}} = t_1 = t$ is then given by

$$\left|\frac{\phi_d}{\phi_c}\right|^2 = \left|\frac{e^{-i\Delta_c/\nu_{\text{FSR}}} t - t}{e^{-i\Delta_c/\nu_{\text{FSR}}} t^2 - 1}\right|^2. \tag{2.28}$$

We find minima of this function for a vanishing numerator, i.e., $e^{-i\Delta_c/\nu_{\text{FSR}}} = 1$, and the resonance condition for the probe-cavity detuning can be formulated as

$$\frac{\Delta_c}{2\pi} = n\,\nu_{\text{FSR}}, \tag{2.29}$$

where $n \in \mathbb{Z}$ is the mode number of a resonance. This is the well-known spectrum of an empty resonator with the spacing between successive resonances being ν_{FSR}. On resonance the power inside the cavity can be calculated to be $|\frac{\phi_{\text{cav}}}{\phi_c}|^2 = 1/(1-t^2) = F$.

2.4.3 Cavity with vanishing finesse

To underline the generality of our derived transmission formula in Eq. (2.22), we show that any lossy resonator can be described accurately up to the extreme point, where the system transforms into just a long waveguide coupled to atoms. This can be done by increasing the coupling between the resonator and the probing waveguide given by t_1, and in the limit of $t_1 \to 0$ we arrive at

$$T = \left|-e^{-i\Delta_c/\nu_{\text{FSR}}} t_{\text{rt}} t_N\right|^2 = t_{\text{rt}}^2 |t_N|^2, \tag{2.30}$$

which is fully consistent with our findings in Eq. (2.26). Note that here t_{rt} describes non-unit transmission of the waveguide due to intrinsic loss.

Having a closer look at $t_1 = \sqrt{1 - \frac{2\kappa_{\text{ext}}}{\nu_{\text{FSR}}}}$, one sees that the transition $t_1 \to 0$ is equivalent with overcoupling the resonator such that $\kappa_{\text{ext}} \to \nu_{\text{FSR}}/2$. For this setting, the coupling waveguide–resonator system reduces to into a long waveguide coupled to atoms. In Fig. 2.3 this transition is shown for the case of atoms coupling to a single mode and many modes of a resonator.

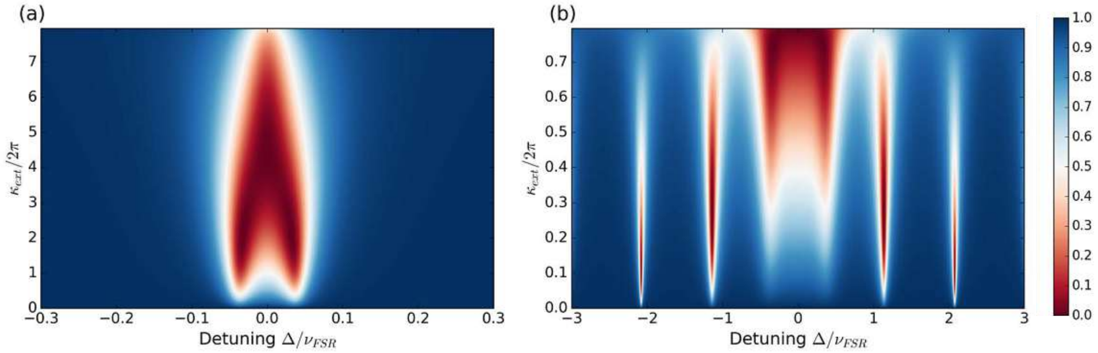

Fig. 2.3 Transmission of the coupled fiber ring resonator as a function of κ_{ext} showing the transition from resonator to single pass waveguide $t_1 \to 0$, when (a) coupling to a single mode and (b) when the coupling strength g_N exceeds the free spectral range. Both panels depict coupling in the collective strong coupling regime, while critically coupled.

2.4.4 Single-atom strong coupling

One of the most discussed and experimentally desired scenarios in cQED is a single atom strongly coupled to a single-mode cavity. In the previous chapter we applied the Jaynes-Cummings Hamiltonian to calculate the output of a probed cavity (see 1.3.2). In this chapter, we applied a real-space Hamiltonian approach in order to derive the transmission spectrum of such a single atom–resonator system, given by

$$T = \left| \frac{e^{-i\Delta_c/\nu_{\text{FSR}}} t_{\text{rt}} t_{\text{at}} - t_1}{e^{-i\Delta_c/\nu_{\text{FSR}}} t_{\text{rt}} t_{\text{at}} t_1 - 1} \right|^2 . \tag{2.31}$$

We can show now that the predictions derived from Jaynes-Cummings are a special case of this transmission formula, i.e., when the atom effectively only couples to one single mode. In this case, we can assume the free spectral range to be the largest characteristic frequency in the system. To do so, for the single-pass transmission we use the quantity $g^2 = 2\beta\gamma\nu_{\text{FSR}}$ to re-formulate t_{at} to be

$$t_{\text{at}} = 1 - \frac{2\beta\gamma}{\gamma + i\Delta_a} = 1 - \frac{2g^2}{g^2 + 2\nu_{\text{FSR}}(\gamma_l + i\Delta_a)} . \tag{2.32}$$

In a single-mode scenario, when $\nu_{\text{FSR}} \gg \Delta_c$ can be assumed, we can approximate for the resonator

$$e^{-i\Delta_c/\nu_{\text{FSR}}} \approx \left(1 - i\frac{\Delta_c}{\nu_{\text{FSR}}}\right) . \tag{2.33}$$

Furthermore, for t_{rt} and t_1 we can approximate $t_i = \sqrt{1 - \frac{2\kappa_i}{\nu_{\mathrm{FSR}}}}$ to become $t_i \approx 1 - \frac{\kappa_i}{\nu_{\mathrm{FSR}}}$. Thus, to first order in ν_{FSR} one arrives at the expression

$$T = \left| \frac{g^2 + (\gamma_l + i\Delta_a)\,(\kappa_0 - \kappa_{ext} + i\Delta_c)}{g^2 + (\gamma_l + i\Delta_a)\,(\kappa_0 + \kappa_{ext} + i\Delta_c)} \right|^2 . \tag{2.34}$$

This finding is identical with the spectrum of a probed resonator predicted by the Jaynes-Cummings approach (see Eq. (1.27)). In Fig. 2.4 the transmission of the full model given by Eq. (2.31) (red line) and the approximation derived here (blue dashed line) is plotted for the case of single mode coupling where $\nu_{\mathrm{FSR}} \gg \Delta_c$, which shows that both models agree perfectly in this parameter range. The deviations between the two models depend only on the choice of the free spectral range and become negligible for $\beta \ll 1/3$.

It is important to mention, that usually in textbook examples, the solution for a strongly coupled atom in a cavity considers for the loss rate due to atomic scattering the parameter γ instead of γ_l. This leads to noticeable deviations of the observed spectral features once $\beta \ll 1/3$ is violated, as shown in Fig. 2.4 (green line).

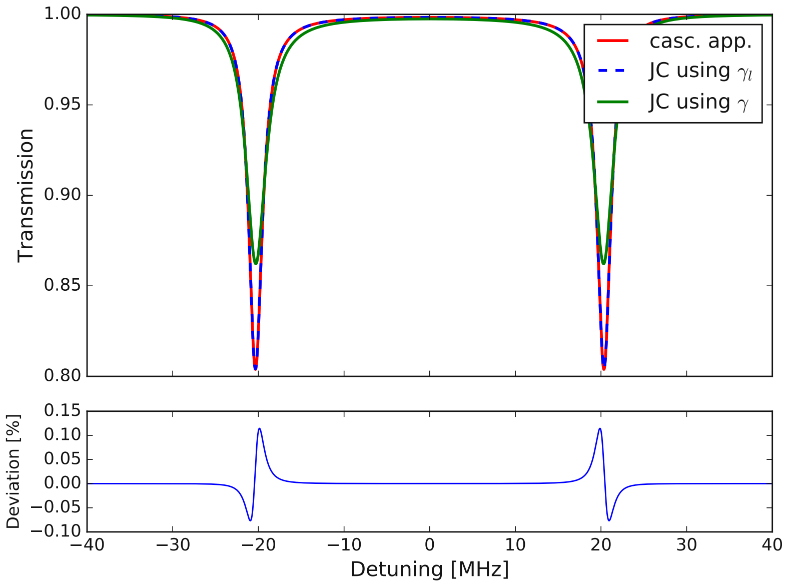

Fig. 2.4 Comparison between the cascaded interaction approach (red) and the conventional strong coupling approach based on the Jaynes-Cumming Hamiltonian (blue dashed) assuming large $\nu_{\mathrm{FSR}} \gg g_N$ and $\beta = 1/3$ for coupling a single atom. These approaches, using γ_l show good agreement (see deviations), where for $\beta \ll 1/3$ the deviations would become sub-permille. Additionally, as a comparison to the textbook scenario, Eq. (1.27) is plotted (green), calculated for an un-altered γ. Here, significant deviations can be observed.

Perfectly coupled single atom

We now discuss the case of strong coupling, where $\beta \approx 1$. For this, we can calculate a maximum coupling rate

$$g_{\max} = \sqrt{2\gamma\nu_{\mathrm{FSR}}}, \tag{2.35}$$

where at the same time the dissipation into non-cavity modes, $\gamma_l = (1-\beta)\gamma \to 0$.

This scenario is clearly violating the restrictions for the atom induced loss rate $g^2/\gamma_l \ll \nu_{\mathrm{FSR}}$, i.e., where $\beta/(1-\beta) \ll 1/2$ needs to be fulfilled. Here, in this scenario of $\beta \to 1$, the quantity g^2/γ_l approaches infinity. Nevertheless, this effect only affects the coupled atom–resonator system for detunings, where $|t_{\mathrm{at}}| = |1 - 2\beta\gamma/(\gamma + i\Delta_a)| \approx 0$ and the effect of the atom becomes small when $t_{\mathrm{at}} \approx 1$. This is the case when the detuning exceeds the atomic linewidth $\Delta_a > \gamma$. For $|t_{\mathrm{at}}| \approx 0$, one will observe significant deviations between the predictions of the Jaynes-Cummings model and the cascaded interaction approach once $\beta \approx 1$, where ultimately our model that considers coupling to adjacent longitudinal modes accurately describes the case of large β coupling.

2.4.5 Collective strong coupling

In a next step we consider collective coupling of an ensemble of atoms to the resonator. Based on the Tavis-Cummings model, for low probing powers the atoms are usually represented by a so-called “superatom”, where the collective coupling is $g_N = \sqrt{N} g_1 = 2\beta\gamma N\nu_{\mathrm{FSR}}$. In Fig. 2.5(a) we see the expected Rabi-splitting of such a coupled single-mode resonator as a function of βN.

When $g_N > \nu_{\mathrm{FSR}}$ we reach the multimode case and we showed in 1.2.3 that the splitting for a coupled superatom saturates at $\nu_{\mathrm{FSR}}/2$. Adding atoms to the resonator still increases the coupling strength g_N but will not increase the splitting. Instead, resonances further detuned from the central resonance $\Delta_c = 0$ will continue to be influenced and shift outwards until the shift also saturates at $\nu_{\mathrm{FSR}}/2$. This behaviour can be shown when numerically solving the multimode Tavis-Cummings Hamiltonian for the systems eigenfrequencies in Eq. (1.17). The results are plotted in Fig. 2.5(b) for an increasing coupling strength. One can see that the shift of further detuned resonances develops a lot slower but eventually saturates as well. Note that here as well the onset of splitting of the central resonance follows $g_N^2 = 2\beta\gamma\nu_{\mathrm{FSR}}$ until it comes of the order of ν_{FSR}.

2.4.6 Collective strong coupling in our model

Finally, we will employ our cascaded interaction approach and discuss the expected spectra for increasing βN and analyse what happens when the conditions $g^2/\gamma_l \ll \nu_{\mathrm{FSR}}$ and $g \ll \nu_{\mathrm{FSR}}$ are no longer valid. For these cases, we will see a significant difference in the spectra compared to the predictions of the Jaynes- and Tavis-Cummings cases discussed before. To this end, we look for eigenfrequencies of the resonator, i.e., modes that (up to loss) are time

TU Bibliothek Your knowledge hub WIEN
Die approbierte gedruckte Originalversion dieser Dissertation ist an der TU Wien Bibliothek verfügbar.
The approved original version of this doctoral thesis is available in print at TU Wien Bibliothek.

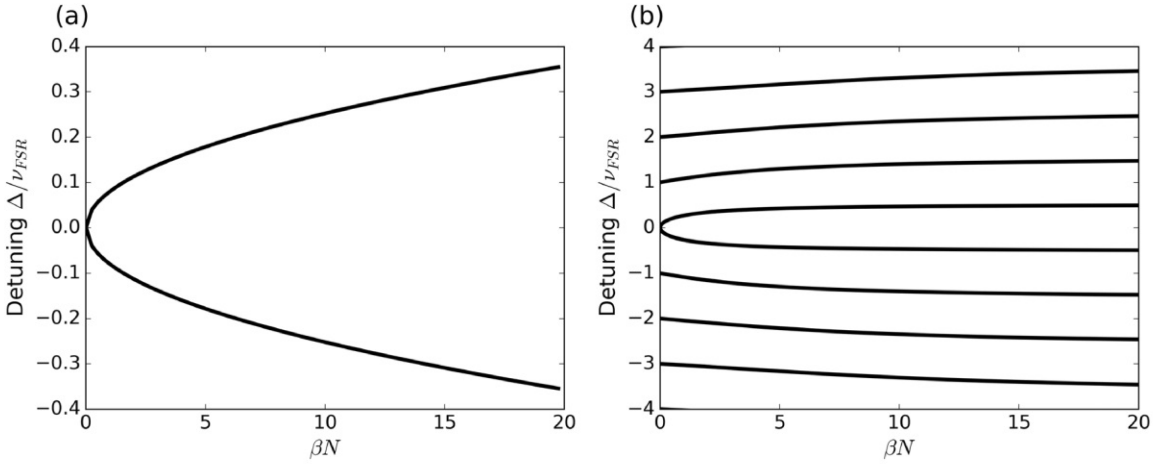

Fig. 2.5 Expected behaviour of a superatom coupling to a single mode (a) and multimode (b) resonator. In the single mode case, the splitting follows the expected $\sqrt{N}$ behaviour, while in the multimode case, the initially split central resonance splits maximally by $\nu_{\mathrm{FSR}}/2$ while adjacent modes will continue shifting for increasing number of coupled atoms (until their shift also saturates).

independent. Using the approximation

$$t_N \approx \exp\left(\frac{-2\beta\gamma N}{\gamma + i\Delta_a}\right) \tag{2.36}$$

we identify the roundtrip phase imparted on the light circulating in the resonator ϕ_{rt} from Eq. 2.22 to be

$$\phi_{\mathrm{rt}} = \phi(\Delta_a, \Delta_c) = \frac{\Delta_c}{\nu_{\mathrm{FSR}}} - \frac{2\beta\gamma N \Delta_a}{\gamma^2 + \Delta_a^2}. \tag{2.37}$$

Assuming a good resonator, where $t_{\mathrm{rt}} \approx 1$ and $t_1 \approx 1$, resonances can be found for

$$\mathrm{Re}\left(\phi(\Delta_a, \Delta_c)\right) = 2\pi \times n \tag{2.38}$$

with the integer number n. We can solve this condition analytically for the case far detuned from atomic resonance $\Delta_a \gg \gamma$. With the approximation $\frac{\Delta_a \gamma}{\gamma^2 + \Delta_a^2} \approx \frac{\gamma}{\Delta_a}$ and using $g_N^2 = 2\beta N \gamma \nu_{\mathrm{FSR}}$ the resonance condition can be written as

$$\Delta_c = \frac{g_N^2}{\Delta_a} + 2\pi n \nu_{\mathrm{FSR}}. \tag{2.39}$$

For the resonant case $\Delta_a = \Delta_c \equiv \Delta$, this can be solved to be

$$\Delta = \pi n \nu_{\mathrm{FSR}} \pm \sqrt{\pi^2 n^2 \nu_{\mathrm{FSR}}^2 + g_1^2 N}. \tag{2.40}$$

This equation clearly shows, that for the coupled resonator described via the cascaded interaction approach, the resonances continue to shift outwards when further increasing the number of coupled atoms, proportional to $\sqrt{N}$. This is a striking difference to the multimode expansion of the Tavis-Cummings model, where the shift saturates for $\nu_{\mathrm{FSR}}/2$. We can observe this behaviour when we probe the system, as for

$$T = \left| \frac{e^{-i\phi(\Delta_a,\Delta_c)} t_{\mathrm{rt}} - t_1}{e^{-i\phi(\Delta_a,\Delta_c)} t_{\mathrm{rt}} t_1 - 1} \right|^2 , \tag{2.41}$$

where $\Delta_a = \Delta_c \equiv \Delta$, we see minima in the power transmission, as plotted in Fig. 2.6(b).

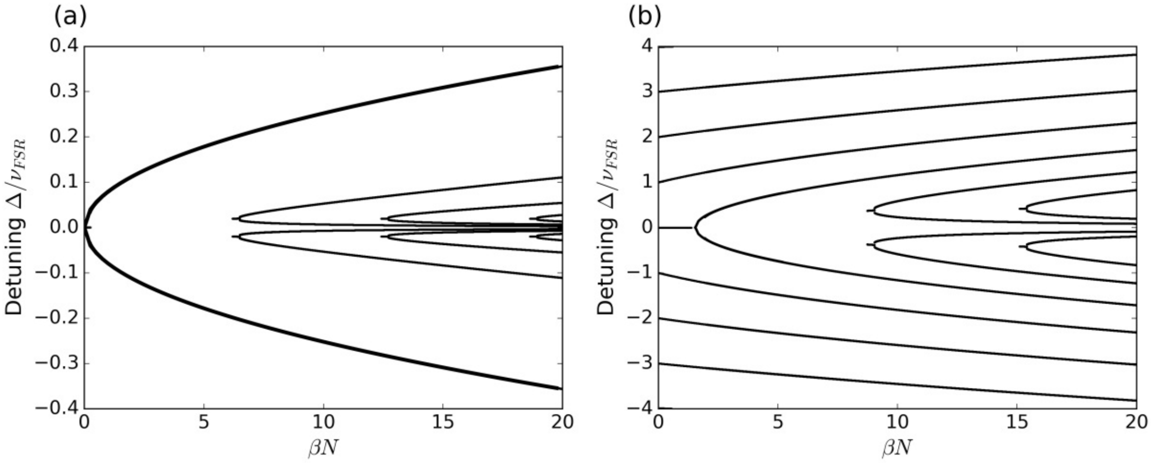

Fig. 2.6 (a) Predictions of the resonances of the coupled atom–resonator system from our cascaded model for the case $\nu_{\mathrm{FSR}} \gg g_N$, where $\nu_{\mathrm{FSR}} = 250\,\mathrm{MHz}$ and $\gamma_l/2\pi = 5\,\mathrm{MHz}$. Here we see new resonances emerging around $\Delta_c = 0$ once $\beta N > 6$. Note that in this regime the Tavis-Cummings approach would still accurately describe the splitting of the outermost resonance, as long as the splitting is much smaller than $\nu_{\mathrm{FSR}}/2$. (b) Predictions of the cascaded approach for a multimode resonator for $\nu_{\mathrm{FSR}} = 10\,\mathrm{MHz}$ and $\gamma_l/2\pi = 5\,\mathrm{MHz}$. Here we observe the splitting exceeding $\nu_{\mathrm{FSR}}/2$ and we expect a continuously increasing splitting with $\sqrt{N}$ as well as the emergence of new resonances in the centre.

New resonances

Interestingly, the cascaded approach predicts the emergence of additional resonances, once $g_N^2/\gamma_l \ll \nu_{\mathrm{FSR}}$ is violated, appearing in the region close to atomic resonance, whose positions can be determined by numerically solving Eq. (2.38) for small detuning $\Delta_a \approx \gamma$. The emergence of new resonances, in between the initial split resonance is a fundamentally different feature of the cascaded approach compared to Jaynes- and Tavis-Cummings, shown in Fig. 2.6 for the "single mode" ($g_N \ll \nu_{\mathrm{FSR}}$) (a) and the "multimode" ($g_N \gg \nu_{\mathrm{FSR}}$) (b) case. This effect is caused by the phase-shift imparted on the cavity field by the atoms during a single roundtrip. While a single strongly coupled atom, or equivalently a superatom, can only impose a maximum phase-shift on the passing light of $\pm\pi$, the cascaded interaction with many atoms in principle allows for any arbitrary phase-shift depending on the number of atoms N. Every additional $\pm\pi$-shift manifests itself as an added optical path length difference of half a wavelength, thus, leading to 4 additional resonance at the output, i.e., 2 new resonances that each split once the phase-shift increases with increasing coupling strength.

The phase-shift imparted on the resonator light passing the atoms is given by

$$\phi(N) = \arg(t_N) \tag{2.42}$$

as shown exemplary in Fig.2.7, where we compare the atom-deduced phase-shifts for the superatom and the cascaded interaction approach. Note that in this figure we do not show the phase-shift the light picks up during a roundtrip through the resonator. In this figure, the phase-shift of an ensemble of atoms coupling with $\beta N = 17$ predicts 8 additional resonances, that can also be observed around atomic resonance in the spectrum plotted in Fig. 2.6.

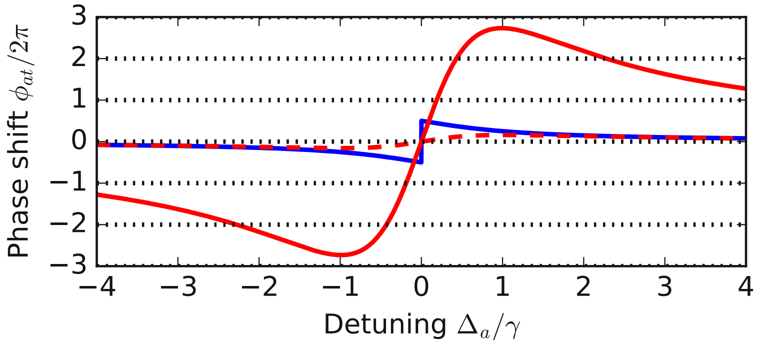

Fig. 2.7 Calculated phase-shifts, where blue depicts the results of the perfectly coupled single atom, $\beta = 1$, while red represents the predictions of our full waveguide description $\beta N = 1$ (red-dashed) and $\beta N = 17$ (red-full) for $\beta = 0.01$, assuming $\gamma < \nu_{\mathrm{FSR}}$. In blue we show the steepest possible phase-shift that is physically possible to be imparted by a single atom, where comparison to the red-dashed line shows a significant discrepancy between the two models, even for this low optical depth of $\beta N = 1$. The cascaded interaction model allows much larger phase-shifts exceeding $\pm\pi$, shown in red for $\beta N = 17$. In the case depicted here, we would see a total of 8 additional resonances when scanning the coupled atom-resonator system.

In the next chapters, I will introduce the experimental setup capable of reaching the multimode strong coupling regime $g_N \gg \nu_{\mathrm{FSR}}$ and I will present experimental observations supporting the constraints of the Tavis-Cummings model, by showing spectra where the splitting does not saturate at $\nu_{\mathrm{FSR}}/2$.

Chapter 3

Optical Nanofibers

In the last decades optical nanofibers received a lot of interest in the optical-scientific community and became a versatile tool widely adapted for diverse applications ranging across nonlinear optics [29, 66–68], nano photonics [44, 56, 57, 69] and quantum optics [58, 59, 70], where for this thesis we are mostly interested in the nanofiber as an excellent interface for coupling light efficiently to quantum emitters such as atoms, molecules or quantum dots [71–73].

An optical nanofiber is made from a standard optical glass-fiber, that has been tapered down to a diameter of several hundreds of nanometres, which is typically smaller than the wavelength of the guided light. A carefully designed adiabatic taper-transition allows for an almost loss-less transition of the guided light from the untapered fiber into the nanofiber waist and back, providing very strong transverse confinement in the waist region. Here, the electromagnetic field can only be guided as a single transverse mode, which travels to largest extend as an evanescent field on the surface of the nanofiber [74, 75]. Thus, emitters that are in close vicinity of the nanofiber surface couple effectively to this mode.

In this chapter, I will introduce basic solutions of the electromagnetic field distribution in optical nanofibers, elaborate on the methods used for manufacturing and characterizing nanofibers and explain in detail the properties of the nanofibers used in our experiment.

3.1 Optical properties of optical nanofibers

To begin with, I will summarize the solution to the single-mode hybrid-electrical (HE) mode of the electromagnetic field guided in a sub-wavelength diameter nanofiber and outline the particularities of its mode structure. Detailed derivations can be found in the works [74, 75].

3.1.1 Electromagnetic fields in the optical nanofiber

We are interested in calculating the electromagnetic field in- and around the optical nanofiber. To this end, we have to find solutions to Maxwell's equations in a dielectric medium without

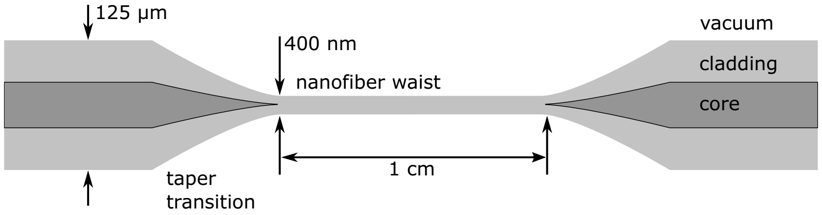

Fig. 3.1 Sketch of the tapered fiber used in our experiment. The unprocessed diameter of 125 μm has been tapered down to 400 nm with a waist length of 1 cm.

charges and currents

$$\Delta \begin{bmatrix} \vec{E}(\vec{r},t) \\ \vec{H}(\vec{r},t) \end{bmatrix} - \mu(\vec{r})\varepsilon(\vec{r})\frac{\partial^2}{\partial t^2}\begin{bmatrix} \vec{E}(\vec{r},t) \\ \vec{H}(\vec{r},t) \end{bmatrix} = 0, \tag{3.1}$$

where $\mu(\vec{r})$ and $\varepsilon(\vec{r})$ are the permittivity and permeability of the medium. Our problem can best be described using cylindrical coordinates, where the z-axis points in direction of light propagation, i.e., along the fiber. For a running wave in the nanofiber, we make an ansatz for the electric $\vec{E}(\vec{r},t)$ and magnetic fields $\vec{H}(\vec{r},t)$ given by

$$\begin{bmatrix} \vec{E}(\vec{r},t) \\ \vec{H}(\vec{r},t) \end{bmatrix} = \begin{bmatrix} \vec{E}(r,\varphi) \\ \vec{H}(r,\varphi) \end{bmatrix} \exp(i[-\omega t + \beta z]). \tag{3.2}$$

Here, $\omega/2\pi$ is the frequency and β the propagation constant of an optical wave in the medium. Note that it is sufficient to solve for the z-components of the electric and magnetic field, where the transverse components are linked to $E_z(r,\varphi)$ ($H_z(r,\varphi)$) via Maxwell's equations. When inserting Eq. (3.2) into Eq. (3.1) we obtain a wave equation for the z-components, given by

$$\left[\partial_r^2 + \frac{1}{r}\partial_r + \frac{1}{r^2}\partial_\varphi^2 + (k^2 - \beta^2)\right]\begin{bmatrix} E_z(r,\varphi) \\ H_z(r,\varphi) \end{bmatrix} = 0. \tag{3.3}$$

In the next step, we can separate the solution into an azimuthal and radial part $E_z(r,\varphi) = E_z(\varphi)\exp(\pm i l\varphi)$, where the integer number l is the mode number. This way we end up with a differential equation for the radial part of the z-component

$$\left[\partial_r^2 + \frac{1}{r}\partial_r + (k^2 - \beta^2 - \frac{l^2}{r^2})\right]\begin{bmatrix} e_z(r) \\ h_z(r) \end{bmatrix} = 0, \tag{3.4}$$

where $e_z(r)$ ($h_z(r)$) are the electric (magnetic) profile functions, respectively.

3.1.2 Solutions of fiber guided modes

To solve Eq. (3.4) one requires boundary conditions to describe the change of refractive index across the optical fiber. For a standard fiber one can assume a stepwise change $n_1 \rightarrow n_2$ for the transition between fiber core and the cladding, where usually for Germanium-doped fibers operating at 850 nm $n_1 \approx 1.447$ and $n_2 \approx 1.442$. For a nanofiber, the light is guided by the index jump between the cladding and the surrounding vacuum ($n_2 = 1$). In the waist region, the initial core diameter is too small to have a significant effect on the light and thus can be neglected for our theoretical considerations. From the boundary conditions of electric and magnetic fields at dielectric surfaces, one can write down an eigenequation for the propagation constant β where one uses modified Bessel functions as an ansatz to describe the modes of propagating fields

$$\left[\frac{J_l'(ha)}{haJ_l(ha)}+\frac{K_l'(qa)}{qaK_l(qa)}\right]\left[\frac{n_1^2J_l'(ha)}{haJ_l(ha)}+\frac{n_2^2K_l'(qa)}{qaK_l(qa)}\right]=\left[\frac{1}{(qa)^2}+\frac{1}{(ha)^2}\right]^2\left[\frac{l\beta}{k_0}\right]^2. \tag{3.5}$$

Here, J_l, K_l, J_l' and K_l' denote the Bessel functions and their derivatives, $h = (n_1^2k^2 - \beta^2)^{1/2}$ and $q = (\beta^2 - n_2^2k^2)^{1/2}$ are introduced as the transverse wavenumbers of the guided mode in the core and the cladding, respectively, a is the fiber radius, and k_0 is the wavenumber of the guided light in vacuum. For the full derivation of the solution, using the nomenclature used here, please refer to [75].

A base set of solutions, shown here for the electric field amplitudes of the guided light, are quasi-circular modes. The term “quasi” is used to highlight the fact that compared to a plane wave in vacuum, here, there are also non-negligible field components pointing in direction of propagation (z-direction). The electric field reads as

$$\vec{E}^{(\omega f l)}_{\text{circ}} = A\left(\hat{r}e_r + c\,l\hat{\varphi}e_\varphi + f\hat{z}e_z\right)\mathrm{e}^{i(f\beta z + c\,l\varphi - \omega t)}. \tag{3.6}$$

Here, $\hat{r}, \hat{\varphi}, \hat{z}$ are the unity vectors in cylindrical coordinates and e_i are the mode profile functions, with $c = \pm$ indicating clockwise or counter-clockwise circulation of the field component with respect to the positive direction of z, $f = \pm$ is the propagation direction, ω is the wavelength of the guided light and A is the amplitude of the field.

When superimposing two quasi-circular polarized modes with opposite polarizations one forms quasi-linear polarized fields

$$\vec{E}^{(\omega f \varphi_0)}_{\text{lin}} = \frac{1}{\sqrt{2}}(\vec{E}^{(\omega f l_-)}_{\text{circ}}\mathrm{e}^{-i\varphi_0} + \vec{E}^{(\omega f l_+)}_{\text{circ}}\mathrm{e}^{-i\varphi_0}), \tag{3.7}$$

with φ_0 giving the angle along which the linear polarization is aligned.

When comparing the intensity distribution of light in the nanofiber to a weakly guiding fiber, one immediately notices an exceedingly different behaviour of intensity. In Fig. 3.2 we show the transition of the intensity distribution $I(r,\varphi) = |\vec{E}(r,\varphi)|^2$ from a fiber with a waist diameter larger than the wavelength of the guided light (a) to a waist much smaller than the same wavelength (b). For the first case the intensity is azimuthally symmetric for all polarizations and decays continuously, while in a nanofiber, looking at quasi-linear polarized light, one finds the cylindrical symmetry broken. The intensity maxima are aligned along the polarization axis of the guided light, where the field intensity has a discontinuity at the fiber surface.

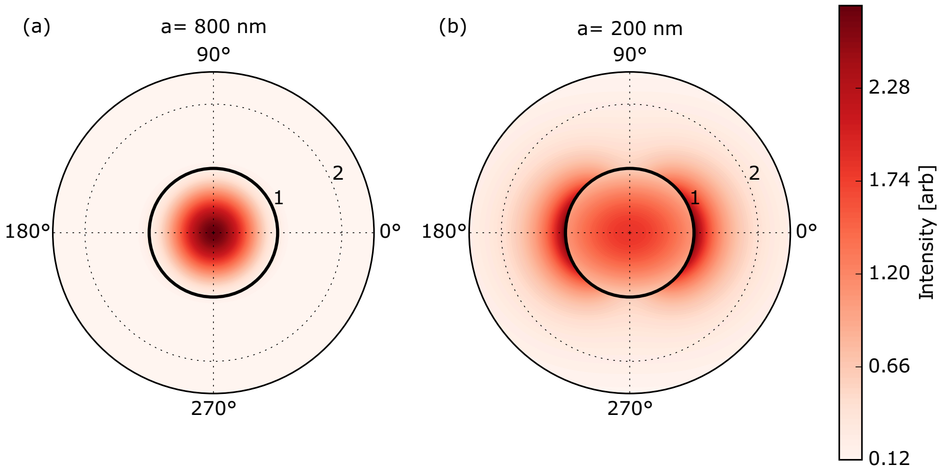

Fig. 3.2 Intensity distribution of the electric field of a linear polarized HE_{11} mode along $\varphi_0 = 0°$ for $\lambda = 850\,\mathrm{nm}$ plotted versus r/a, where a is the corresponding fiber radius, with the fiber surface indicated as black solid line. (a) Optical fiber with a core radius of $a = 800\,\mathrm{nm}$, $n_1 = 1.4469$ and $n_2 = 1.0$, and (b) nanofiber with a fiber radius of $a = 200\,\mathrm{nm}$ for the same refractive indices. Once the fiber radius is much smaller than the wavelength of guided light, the field is mostly guided on the outside of the fiber, and in the case of quasi-linear polarized light the evanescent field is not azimuthally symmetric. Note that the intensity has been normalized to the maximum value of the field in (a).

3.1.3 Mode spectrum of guided light

The guided electromagnetic waves in the nanofiber can be named and ordered using the z-component of the mode profiles of the electric field $\left(\hat{r}e_r + c\,l\hat{\varphi}e_\varphi + f\hat{z}e_z\right)$ and the magnetic field $\left(\hat{r}h_r + c\,l\hat{\varphi}h_\varphi + f\hat{z}h_z\right)$. The corresponding fields are then called HE_{lm} or EH_{lm}, for $h_z > e_z$ and $e_z > h_z$, respectively. Here, l corresponds to the mode number and m counts the number of solutions for β with increasing values of ha.

An important quantity that can be used to characterize the nanofiber is the geometric parameter $V = ka\sqrt{n_1^2 - n_2^2}$, where for $V < 2.405$ the nanofiber only guides a single mode, in particular, the only guided mode in the waist is HE_{11}. Depending on the refractive index of the fiber cladding n_1, this quantity gives an upper bound for the nanofiber radius in order to fabricate a single-mode waist. Furthermore, when calculating the intensity distribution around a nanofiber, it can be shown that for a given power, the guided evanescent field intensity on the surface reaches a maximum for $a/\lambda = 0.23$, where a is the fiber radius and λ the wavelength of the guided light [76]. In our experiment, we chose the radius to be 200 nm, where $a/\lambda \approx 0.235$ and $V \approx 2.12$.

3.2 Manufacturing of nanofibers

There are several different ways of tapering optical fibers mostly by pulling while heating or chemical etching. These methods include flame-brushing, ceramic heaters, and CO_2-lasers [77–81], as well as etching with hydrofluoric acid [82–84].

3.2.1 Method

In our group we specialized on the flame-brushing technique, where the fiber is moved slowly back and forth over a static hydrogen-oxygen flame providing a variable area the fiber is heated while being stretched at the same time. This method allows for a precise control of the heating area, that is changed over time, as shown in Fig. 3.3 and 3.4. A loss-less transition from a single mode guided light into the HE_{11}-mode of the nanofiber is generally possible providing a taper transition fulfilling the adiabaticity criterion (see for details [85–87])

$$\left|\frac{dr}{dz}\right| \leq \frac{r(\beta_1 - \beta_2)}{2\pi}. \tag{3.8}$$

Here, r is the radius of the fiber, z the position along the taper and β_i the propagation constant of the fundamental mode and the mode it is most likely to be scattered into, respectively.

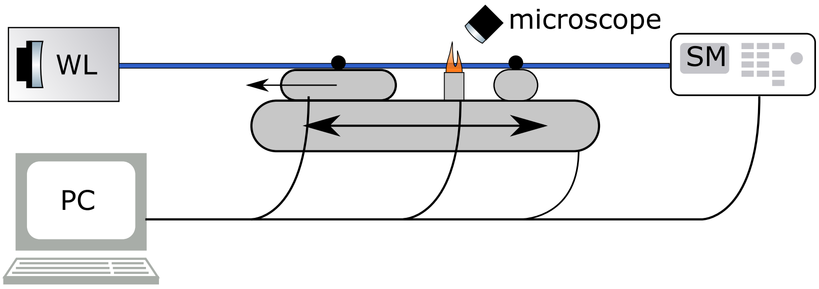

Fig. 3.3 Sketch of the established fiber pulling rig with its two translation stages in piggy-back configuration. One translation stage moves the fiber across the flame, while the other stage only stretches the fiber. The transmission is monitored with a white-light source and an optical spectrometer. Additionally, a microscope is imaging the centre of the waist region to check for a correct placement and possible contamination of the fiber before the pull.

In principle there are many taper shapes that fulfil this adiabaticity criterion, as for example [88, 89]. However, for manufacturing, the simplest approach employs a stationary flame while the fiber is stretched, creating an adiabatic taper with exponentially decreasing radius. A shortcoming of this approach is that the overall taper length is much larger than theoretically necessary to keep the transition adiabatic. Thus, it is mostly infeasible for actual experimental implementations. Thus, we employ a variable heating area where one creates quasi-linear tapers as a succession of very small exponential taper slopes. To this end, one can solve in reverse for the required variable heating area and start position of the flame for the pulling process, given the flame width (for us 1 mm), the taper transition and waist radius as constraints [87]. The outcome is translated into trajectories for the translation stages of our pulling rigs. Typically, this calculation includes an optimisation to realize the desired waist radius as good as possible for the capabilities of the pulling rigs. Final optimization of the fiber transmission requires finding suitable parameters for taper angles and transition radii [90] that can be found through successive pulling attempts.

With our rigs, we mostly pull fibers with two or three linear taper transitions. At the fiber positions where the difference between propagation constants of the fundamental mode and higher-ordered modes is small, it is likely that higher ordered modes are launched. Around the corresponding radii, the taper will be kept at shallow angles to avoid accidental launching of such modes and thus, prevent loss. A higher order mode cannot transfer into the single mode guided in the waist and will be scattered from the taper once the fiber radius becomes smaller. Everywhere else, the taper can be much steeper, which allows to create shorter fibers. Note that alternatively to pulling with a succession of linear tapers, it is possible to fabricate adiabatic tapers of shortest lengths possible, using locally varying taper angles allowing to always fulfil the adiabaticity criterion [91], or manufacturing glass fibers with a refractive index variation that allows for implicit adiabatic transition, independent of the taper transition [92].

There are two fiber pulling rigs in our group, both using the flame-brushing technique. The original rig was developed in our group [78] and is set up in a piggy-back configuration of two translation stages (see Fig. 3.3), to decouple the stretching of the fiber from moving the flame across the fiber.

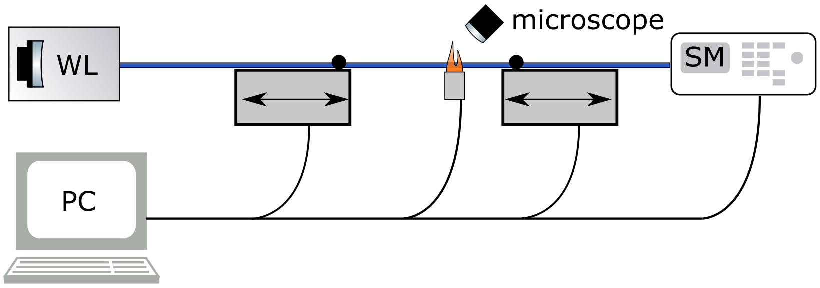

Fig. 3.4 Sketch of newly set up pulling rig with two individual translation stages.

The second pulling rig (see Fig. 3.4) was recently set up and consists of two individual translation stages, where each performs a convolution of moving and stretching the fiber [93]. A possible disadvantage of this setup is potential synchronization issues in the turnaround of the stages. This would introduce parasitic stretching or sagging of the fiber. Nevertheless, these stages have a very good resolution of positions and are well calibrated. We monitor the pulling, among other things, with a microscope, imaging the fiber section above the flame. During the pulling process we cannot perceive any movement of the fiber, underlining the superior calibration. Additionally, this setup allows for much smaller gas pressures, hence lower temperatures of the flame and therefore, slower and smoother pulling. Note that for both of our fiber rigs, known problems in the final pulling steps are the fiber sagging due to its own weight, placing it closer to the flame while at the same time the gas pressure of

TU Bibliothek WIEN Your knowledge hub
Die approbierte gedruckte Originalversion dieser Dissertation ist an der TU Wien Bibliothek verfügbar.
The approved original version of this doctoral thesis is available in print at TU Wien Bibliothek.

the flame pushing the much lighter waist of the fiber up. Both effects introduce parasitic stretching of the fiber. Judging by the transmission of fibers we pulled so far, it appears as if the overall quality of processed fibers from the new rig is much higher. Presumably, this is given by the slower dynamics offering more control in the turnaround, and the lower gas pressures that can be used, where tiny misplacements in the final pulling steps are not as crucial and the gas pressure will not push the nanofiber significantly.

3.2.2 Monitoring and optimising the pulling process using the new rig

The experiment presented in this thesis was the first one in our group to receive fibers pulled in the new rig. Here, I will briefly present my work on calibrating the new pulling rig and compare its performance to the original rig. I would like to point out that our group technician Thomas Hoinkes is the main responsible for both our fiber rigs, who moved the new rig from Universtität Bonn and set it up in Vienna. He implemented the optimisation routines, used by the software of the established rig to calculate translation stage trajectories, to be compatible with the software routine of the new setup. After this update, the versatile new rig could pull nanofibers with three linear taper sections and a much higher sampling rate of individual steps, taking full advantage of the capabilities of the high-end translation stages.

To monitor the performance of the pulling process, we usually measure the spectrum of a white-light source transmitted through the fiber throughout the pulling process. This allows us to judge the quality of the fiber by measuring the absolute transmission at our probing and potential trapping wavelengths, as well as observing the launch of higher ordered modes during the tapering process. The presence of higher ordered modes can be observed as a beat signal in transmission (see Fig. 3.5) that indicates local steep changes in the taper transition, thus it is necessary to further optimise the pulling process. We eventually found a combination of gas pressure and O_2/H_2-ratio, as well as pulling speed for our established 500 nm diameter [57, 90] and new 400 nm diameter fibers, where throughout the pulling process only very little beating between the fundamental and higher ordered modes was observed. Here, we estimated that less than 0.5% of energy was coupled to higher ordered modes. Furthermore, after careful optimisation, within the resolution of the spectrometer we could not measure any loss after tapering.

In order to measure transmissions more accurately than the white-light source and spectrometer allows, we installed a 852 nm laser for a calibrated absolute measurement of the transmission through the fiber as part of a bachelor thesis on this experiment [94]. The best ever transmission for one of our later used nanofibers of 400 nm diameter and 1 cm length was measured to be $99.69 \pm 0.12\%$ (see Fig 3.5). Eventually, we returned to monitoring the tapering with the white-light source, mostly because using the laser created a lot of overhead time in the preparation of the transmission measurement during which the cleaned bare fiber could easily get polluted prior to pulling.

Lastly, to make sure the new pulling rig is up to the standards of the established rig, we pulled several fibers and measured the diameter using a secondary electron microscope (SEM), that we could use as part of a TU collaboration with USTEM (“Universitäre Service-Einrichtung für Transmissions-Elektronenmikroskopie"). Figure 3.6(a) shows an image of

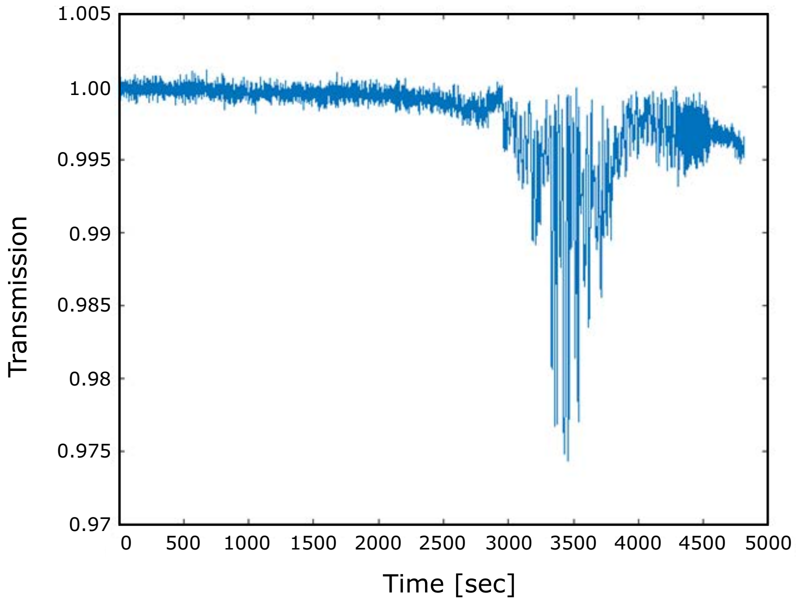

Fig. 3.5 Fiber transmission over time of a 850 nm laser during the pulling process. The laser light was split using a 50:50 fiber beamsplitter, where one arm goes through the pulled fiber and the other arm is used to normalize the transmission. The intermodal beating of transmission after about 3000 seconds is a clear signature of higher ordered modes being launched during the tapering process. The transmission recovers afterwards and settled at $99.69 \pm 0.12\%$. This indicates that steep taper transitions only occurred as intermediate steps in the pulling process.

a small section of a 500 nm fiber with a 5 mm waist. To be able to get a SEM image of a nanofiber, the waist is glued to a silica waver with conducting glue and coated with a gold-palladium compound, estimated to be of 4 nm thickness. This process prevents excessive charging of the sample, which would eventually spoil the quality of the image. In Fig. 3.6(b) we show the inferred fiber radius vs. waist length, measured from a manual scan across the waist. As one can see, the centre of the waist is slightly thicker than the transition from taper to waist, which presumably is due to the longer time the flame stays in this regions during the turnaround. This is not an unexpected finding and is also observed from fibers pulled with the established rig and similar findings are reported in [70]. The measurement shown fits the fiber diameter estimation after optimisation of the pulling rig well and the inferred diameters compare very well with those of nanofibers pulled in the established rig.

3.2.3 Mounting of the fibers

The mounting of the nanofibers onto a suitable fiber mount is done inside the pulling rig, directly after pulling. The mount is carefully placed underneath the fiber and lifted using a stage with a micrometer screw such, that the fiber is barely touching the mount before we apply UV-light curable and ultra-high vacuum (UHV) compatible glue. In our setup we need to bring the front of the fiber to the back of the chamber where the UHV feedthroughs

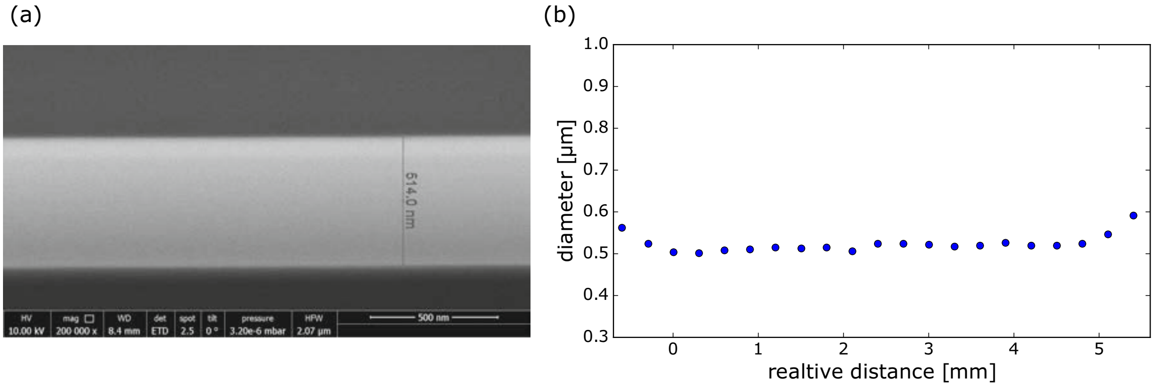

Fig. 3.6 (a) Demonstration of the radius measurement from a SEM image. The radius was inferred using a succession of in-software ruler readings. In order to image the fiber, the sample is coated with a 4 nm gold-palladium compound, that according to USTEM, should not significantly alter any length measurements, since the measurement uncertainty is $\lesssim 5$ nm. (b) Inferred waist diameter of the nanofiber in (a), with a target target diameter of 500 nm, simulated by the optimisation routine to be pulled to be 513.94 nm with the new pulling rig. The transmission was measured to be 95.5% with a mean measured diameter of 515 nm.

are located. A loose fiber-loop would lead to the fiber touching the inside of the glass cell, possibly inducing loss or unexpected behaviour, e.g., wrapping or twisting. In contrast, a too tight loop leads to excessive bending loss. Therefore, during bending and gluing we were still monitoring the transmission. We continue to constrict the loop radius until we observe an onset of transmission loss at around 930 nm. At this point, we glue the fiber on the side of the mount (compare Fig. 3.7). This way the loss can be controlled and the fiber is not hanging in the way while screwing the mount onto the fiberarm when inserting it into the vacuum chamber. After gluing, the nanofiber can be released from the pulling rig's fiber fixation and the mount can be placed into a vacuum chamber or in a suitable storage environment.

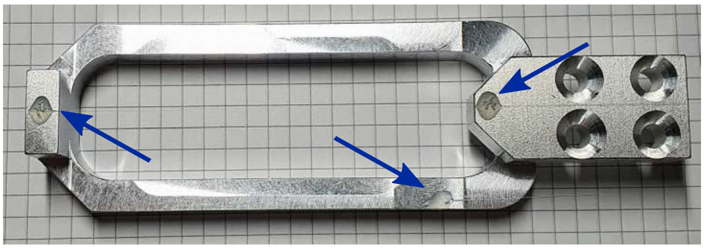

Fig. 3.7 Picture of the fibermount used for the first fiber, after it has been replaced in Berlin. One can clearly see the two glue points placed centrally to fix the fiber and one on the side of the frame to safely guide the fiber to the back of the chamber.

Die approbierte gedruckte Originalversion dieser Dissertation ist an der TU Wien Bibliothek verfügbar.
The approved original version of this doctoral thesis is available in print at TU Wien Bibliothek.
TU Bibliothek WIEN Your knowledge hub

3.2.4 Conclusions regarding new pulling rig

To summarize, we managed to set up a fiber pulling rig and pull fibers with transmission performance as good as that of the established pulling rig. The transmission for fibers with 400 nm diameter and 1 cm length are on average above 99%. The biggest advantage in the new rig is the low temperature of the flame and the excellent accuracy in positioning of the translation stages, allowing for much slower pulling speed. These are excellent conditions for pulling fibers with longer waists or more challenging types of nanofibers with extremely small waist radii. Possible displacement of the fiber, i.e., sag due its weight, excessive blowing away of the waist and parasitic stretching in the turnaround of the translation stages will not have such a drastic impact, resulting in overall better transmission outcome. A possible downside of the new rig is that pulling a single high-quality nanofiber takes much longer than in the established rig. Note that at this point of optimisation of both pulling rigs the limiting factor for an excellent installed nanofiber is the fiber handling. Especially removing the fiber coating completely and cleaning the bare fiber before pulling and keeping the waist and taper unperturbed during the installation are key for good transmission performance. Standard nanofibers should in my opinion be pulled in the established rig, in order to keep the time of exposing the nanofiber to the environment as short as possible, allowing the new rig to be used for pulling more challenging nanofibers.

3.3 Experimentally implemented nanofibers

For our experiment we use optical nanofibers with a target waist diameter of 400 nm and 1 cm waist length. For the taper we optimized the transmission using two linear sections of 3 mrad and 2 mrad angle of incline before exponentially transitioning into the waist. The change for the two transitions is set to occur at 40 μm radius. Simulating and optimizing our pulling process resulted in an overall length of the tapered fiber to be 77.76 mm with a simulated waist radius of 204.37 nm.

The two fibers used in the experiment were measured to have transmissions at 852 nm of $99.0 \pm 0.1\%$ (Fig. 3.8(a)) and $98.2 \pm 0.3\%$ (Fig. 3.8(b)), measured after pulling. Note that our pulling process in principle allows for taper transitions with the transmission easily exceeding 99.5%, but for this experiment a pulling configuration compatible with the asymmetric fiber holder was required. In this setting the fiber can sag more than usually which eventually leads to less ideal placement with respect to the flame in the final pulling steps.

In our experiment we use a *Fibercore SM800(5.6/125)* single-mode fiber, specified for an operating wavelength of 830 nm. The actual fiber patch we use has specifically been selected by the manufacturer, to have its cut-off wavelengths outside 685 nm and 935 nm. These wavelengths were calculated to be magical wavelengths when trapping Cs atoms in a dipole trap via the evanescent field of the guided modes close to the nanofiber surface. This way the trap fields will not induce AC-Stark shifts with respect to the resonant probe light for the trapped Cesium atoms [24, 95]. So far, trapping atoms has not yet been implemented for this experiment, but was already considered during fiber fabrication and left as an option similar to [23].

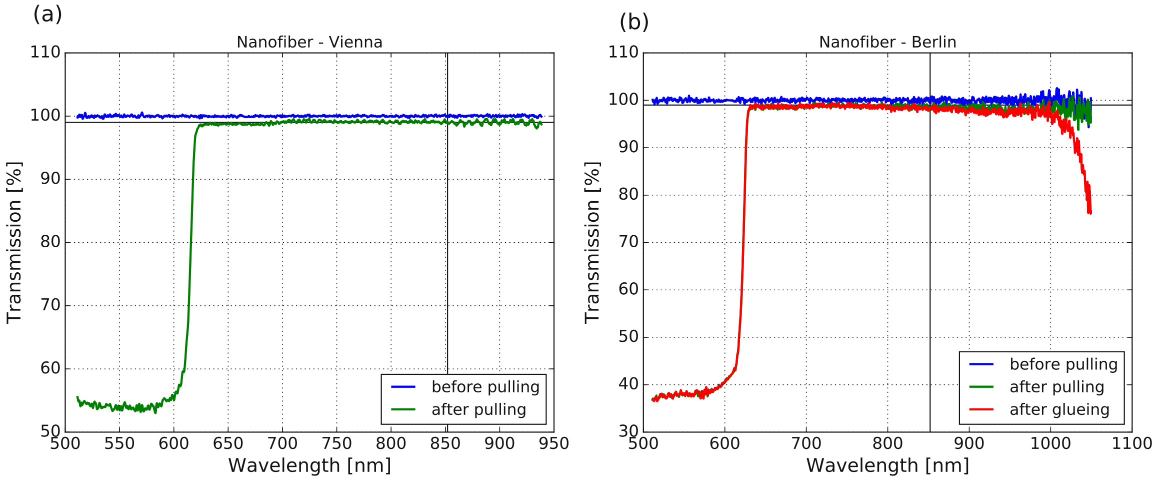

Fig. 3.8 Transmission spectrum through the implemented nanofibers in our experiment. The spectra were taken with a white-light source and a broadband spectrometer before (blue) and after (green) the pulling process. (a) The nanofiber pulled and placed into vacuum at TU Wien features a transmission for our probe wavelength of 852 nm at $99.0 \pm 0.1\%$.
(b) The nanofiber inserted at HU Berlin features a transmission for our probe wavelength at $98.2 \pm 0.3\%$ after it was glued to the mount (red). For both fibers, the steep transmission loss at around 620 nm is due to the cut-off wavelength of the *SM800* fiber and lays well below our optional trapping fields at a wavelength of 685 nm. The drop in transmission close to the upper cut-off wavelength of the fiber, around 980 nm, is due to bending and gluing part of the fiber onto the mount to guide it back safely towards the vacuum feedthroughs.

Chapter 4

Experimental implementation of the fiber ring resonator

The experiment presented in this thesis is centred around long fiber ring resonators with integrated optical nanofibers. After I have discussed the properties of our nanofibers and their role in interfacing cold atoms, I want to dedicate this chapter to the discussion of the implementation and characterization of our resonators. To start with, I will discuss the polarization properties of a fiber ring resonator and how we use the Hänsch-Couillaud method to lock it [96]. Based on this, I will introduce the experimental implementation of our resonators and present a characterization and discussion on their performance regarding intrinsic loss rates and presumable origin of the loss.

4.1 Polarization properties of light in fiber ring resonators

In order to understand the locking method based on the Hänsch-Couillaud method, I want to first discuss the polarization properties of a fiber ring resonator. Our resonator consists of non-polarization maintaining fiber that due to the fabrication process possess local imperfections and stress in the fiber core. Thus, light propagating through the fiber experiences polarization dependent phase-shifts and if the ends of this fiber are connected to a loop, one forms a birefringent resonator. The field guided in the fiber can be described using the Jones-formalism [97], given by a Jones-vector

$$\vec{E} = \begin{pmatrix} A_\mathrm{H} \\ A_\mathrm{V} e^{i\phi} \end{pmatrix} e^{i(\omega t - kz)}. \tag{4.1}$$

Here, light with frequency ω and wavenumber k is propagating in z direction along the fiber, where the amplitudes of horizontal (vertical) polarization are given by A_H (A_V). Most importantly there is a phase ϕ between these two components. Using the Jones-formalism we can calculate the effect of the resonator on light after one roundtrip to be

$$T_\mathrm{Res} = R - TC(I - RC)^{-1}T, \tag{4.2}$$

where the first term describes the light directly reflected form the input coupler and the second term describes the light output from the resonator, as depicted in Fig. 4.1. Here, C is the polarization transformation inside the resonator, I is the unity matrix, and R and T are the reflectance the transmittance of the input coupler, given by

$$R = \begin{pmatrix} r_H & 0 \\ 0 & r_V \end{pmatrix} \quad T = \begin{pmatrix} t_H & 0 \\ 0 & t_V \end{pmatrix}. \tag{4.3}$$

The eigenvalues of T_{Res} are given by

$$t^i_{\text{Res}}(\omega) = r_i - \frac{t_i^2 c_i(\omega)}{1 - r_i c_i(\omega)}, \tag{4.4}$$

where t,r and c are the eigenvalues of T,R,C in Eq. (4.2) for the eigenpolarizations $i = a,b$. Note that for positive real eigenvalues of $t^i_{\text{Res}}(\omega)$ the fiber guided light in the ring will be resonant. In general, this occurs at different frequencies ω, which one can observe as two sets of resonances (a,b) when measuring the transmission spectrum.

For our application we use in-fiber polarization controllers inside the fiber ring resonator to manipulate the resonators birefringence such that the two eigenpolarizations are resonant at frequencies maximally split from each other, being $\Delta\omega = \omega_{\text{FSR}}/2$.

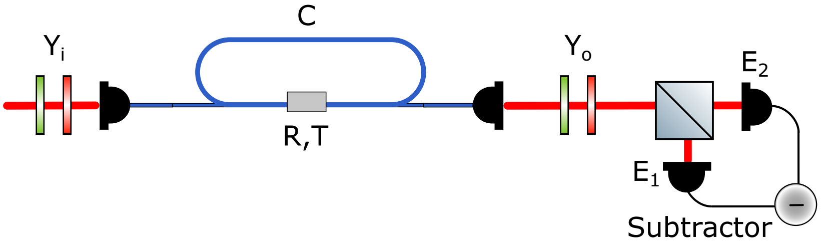

Fig. 4.1 Sketch of the fiber ring resonator with indicated polarization controllers for the in- and output, given by the Jones-matrices $Y_{i,o}$. The fiber beamsplitter is characterized via its reflectance R and transmittance T, and the birefringent resonator is is represented by the matrix C.

4.2 Locking the resonator

For small deviations of a resonator's optical length $\Delta L_{\text{opt}} \approx \lambda$, the light being resonant inside the resonator will exhibit large phase-shifts, having an impact on the position of its resonances. Therefore, it is necessary to implement a method to lock the resonator to fix it spectrally with respect to the probing laser and hence, to the atomic transition. To this end, we change the resonator's length according to a feedback generated from polarization spectroscopy, as introduced in [98]. For our setup this is done by stretching a small part of the ring resonator with a piezo-controlled fiber stretching setup, discussed in detail below.

For the feedback, we generate an error signal making use of the birefringent nature of the fiber ring resonator. For this, the polarization at the in- and output of the resonator can be set using $\lambda/4$ and $\lambda/2$ waveplates. At the output, a polarising beamsplitter (BS) separates the eigenpolarizations of the resonator and two photodiodes (PD) measure the intensity of the corresponding fields. The desired error signal is proportional to the difference of these signals $\Delta_{\text{err}} \propto |E_1|^2 - |E_2|^2$, where the projections of the field onto the basis of the polarizing BS are given by

$$\begin{aligned} E_1 &= \begin{pmatrix} 1 \\ 0 \end{pmatrix} Y_o T_{\text{Res}} Y_i \vec{E}_{\text{Laser}} \\ E_2 &= \begin{pmatrix} 0 \\ 1 \end{pmatrix} Y_o T_{\text{Res}} Y_i \vec{E}_{\text{Laser}}. \end{aligned} \tag{4.5}$$

Here, $Y_{i,o}$ are the Jones-matrices of the in- and output waveplates and $\vec{E}_{\text{Laser}}$ is the locking laser field with $|E_0|^2$ being the input intensity. With this definition the error signal can be calculated to be

$$\Delta_{\text{err}} = |E_1|^2 - |E_2|^2 = E_0^2 \,\text{Re}\left\{ \left(t^a_{\text{Res}}(\omega)\right)^* t^b_{\text{Res}}(\omega) e^{i(\gamma+\phi)} \right\}, \tag{4.6}$$

where γ and ϕ are the phase-shifts set by the input and output waveplates.

If we assume, that the polarization transformation $t^{a,b}_{\text{Res}}$ inside an experimentally realized birefringent resonator is unknown, Eq. (4.6) shows that a suitable error signal can still be achieved by correctly choosing γ and ϕ. This occurs when the in- and output phase-shifts are set to counteract the phase-shift picked up during a resonator roundtrip, which in our case of maximally separated resonances can be achieved for $\gamma + \phi \approx \pm\pi/2$. In this case, the difference signal Δ_{err} corresponds to the imaginary part or the resonator's transmission spectrum, featuring steep zero crossings at the position of the resonances, making it an ideal error signal. In Fig. 4.2(b) we show such an obtained error signal for a critically coupled resonator with maximally separated and equally excited eigenpolarizations.

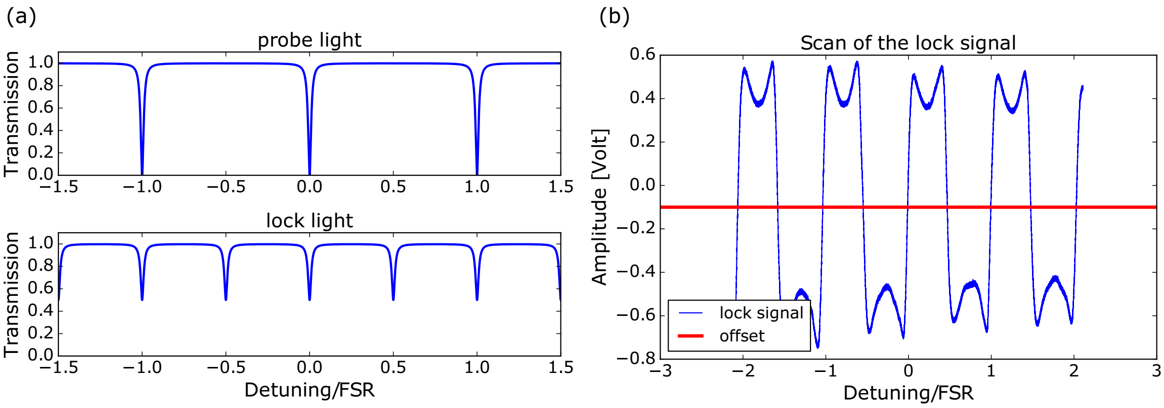

Fig. 4.2 (a) Sketch of the transmission signal of the probe light, where only one eigenpolarization is excited and lock light, where both eigenpolarizations are excited. (b) Experimentally obtained error signal of the resonator set up in Berlin. The polarization controllers have been aligned to maximally separate and equally excite the resonator's eigenpolarizations when interfaced with the lock light, as depicted in (a). Note that due to an imperfect beamsplitter setup the signal inferred on one PD is slightly higher, hence the offset error-signal.

4.3 Implementation of the resonator

During the course of this thesis two resonator setups were implemented. We took advantage of the group's move from Technische Universität Wien to Humboldt Universität zu Berlin to upgrade the setup by exchanging the fiber ring resonator and including a new nanofiber into the vacuum chamber.

In general, both fiber ring resonators are realized by closing a long optical fiber containing a nanofiber section to a loop. The key element of these resonators is the optical nanofiber that is placed inside the UHV chamber. Experimentally, to integrate it into the resonator, the tapered fiber's pigtails, that are fed trough vacuum tight ferules, are joined to a form a resonator via splicing it to a variable fiber beamsplitter (FBS) (see Fig. 4.3). The two individual resonators used in this thesis had a length of 29.3 m and 45.5 m and are characterized in detail in the back of this chapter. Below, I will in detail introduce the different elements of our resonators and their role for interfacing and locking the resonator.

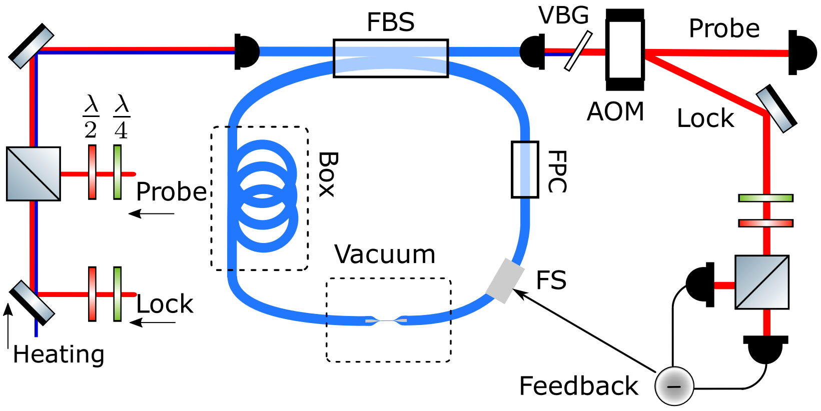

Fig. 4.3 Experimental realization of the fiber ring resonator with a nanofiber section inside a vacuum chamber. The light is coupled into the resonator using a fiber beamsplitter (FBS). The light inside the resonator can be manipulated using in-fiber polarization controllers (FPC) necessary to prepare the polarization to allow for locking of the resonator. The error signal is obtained in the polarization spectroscopy setup at the resonator output, where a suitable feedback is sent to a fiber stretcher (FS) integrated into the resonator.

Beamsplitter

Another important element of the resonator is a variable fiber beamsplitter that is used to couple probe light to the resonator. The FBS[1] allows for setting the splitting ratio between the coupling fiber and the resonator continuously. In this way we were able to both, critically couple the incoming light to the empty resonator ($\kappa_0 = \kappa_{\text{ext}}$) and fully overcouple the resonator ($\kappa_{\text{ext}} \gg \kappa_0$). The two settings allow us to measure the single-pass optical density of the atomic ensemble when the resonator is fully-overcoupled, and study strong atom–resonator coupling when the resonator is critically coupled.

---

[1] Newport F-CPL-830-N-FA

Lock setup

In this experiment a master laser, locked to the resonant D2-hyperfine transition of Cesium, is used for probing and locking the resonator. For locking the laser, we use Doppler-free absorption spectroscopy through a Cesium vapour reference cell and Pound-Drever-Hall locking [99, 100] (details in ch. 5). In this way, it is sufficient to lock the resonator to the laser for having a fixed relation between the atomic transition and the resonator spectrum while probing.

Our experimental realization of the lock involves the control of the resonator's eigenpolarizations, which could be attained via in-fiber polarization controllers (FPC) containing part of the resonator fiber, as well as a set of waveplates at the in- and output of the resonator. For the active stabilization of the resonator, we change its optical path length using a piezo-controlled fiber-stretcher (FS) that is integrated into the fiber ring resonator and provides the feedback evaluated in the lock setup, as depicted in Fig. 4.4.

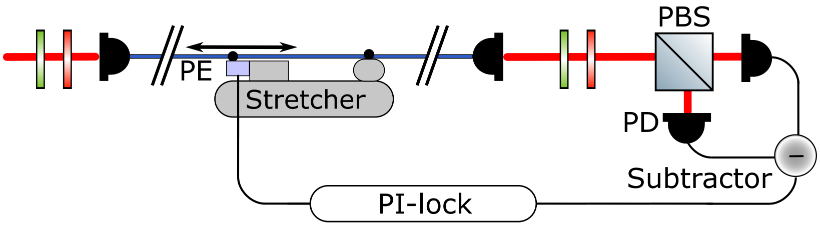

Fig. 4.4 The lock consists of a polarization spectroscopy setup, generating an error signal of the measured eigenpolarizations at the output of the resonator, where in a PI-loop a suitable feedback is calculated. The feedback is forwarded to a fiber stretching mount integrated into the fiber ring resonator. Here, a piezoelectric element (PE) glued to the fiber changes the length of the resonator accordingly.

Interfacing and locking our resonator is done with two independent light fields, a weak probe light for measurements of the interaction with the atomic ensemble and a far more intense field for locking of the resonator frequency that requires the excitation of both resonator eigenpolarizations. To control these fields separately, we need to be able to set a fixed phase relation between these two fields. To do so, we first interface the resonator using probe light and set the in-fiber polarization controllers inside the resonator such that, at the output of the resonator, the measured transmission spectrum shows both eigenpolarizations maximally separated. Next, the input polarization of the probe light is set to be aligned to only one of the resonator's eigenpolarizations. At the same time, the input polarization of the lock light is set to equally excite both eigenpolarizations, as seen in Fig. 4.2(a). In a last step, the output polarization of the lock light is set as explained above to reveal a suitable error signal (Fig. 4.2(b)). Now, by choosing the polarity of the error signal one locks to the eigenpolarization that was initially set to be the one interfaced by the probe light.

While in Vienna, the error signal was fed into a National Instruments (NI) card, where a software-based PI-loop generated the feedback signal for the resonator. The feedback was amplified and sent to a translation stage glued to the fiber ring resonator controlled via a piezoelectric element, where this stage then changed the elongation of the fiber. The bandwidth of the lock including the actuator was measured to be $\sim 30\,\mathrm{Hz}$, sufficient to compensate for slow temperature drifts, locking the resonator successfully. In Berlin, we use a faster analogue PI-loop and an updated amplifier driving a piezoelectric element that is now directly glued to the fiber, resulting in a bandwidth $\gtrsim 1\,\mathrm{kHz}$.

Mechanical setup

Except for the nanofiber and its pigtails, the whole resonator setup is placed on a breadboard inside a Styrofoam insulated double-walled wooden box, depicted in Fig. 4.5. In this way we realize very stable conditions, minimizing perturbations that could cause fast erratic changes or excessive long-term drifts of the resonator's length. The double walled box is sturdily fixed to the optical table. In order to access and interface the resonator, the box has holes for fibers leading to the vacuum chamber, for connections controlling the lock actuator and for the adjustment screw of the variable beamsplitter. All parts are fixed sturdily to the breadboard and most of the fiber resonator itself is wound around a massive metallic spool, acting as thermal bath and fiber fixture. We assume that by doing so, the temperature of the fiber is in equilibrium with the bulk metal and temperature deviations across the resonator are kept small. Furthermore, we noticed that twisted and strongly bent fiber sections are likely to pick up of stress induced strain when they are mechanically excited. We observed that such excitations lead to fast erratic fluctuations distorting the spectral features in our transmission measurements. Therefore, we took special care to not put the fiber under any excess stress, e.g., winding too tight around the spool, crossing fibers on the spool, too small bending radii, and any obvious twisting of the fiber. The first fiber spool was 6.4 cm in diameter and we noticed, that this still induces significant bending loss ($\sim 4\%$), which is why for the second setup of the fiber ring resonator a wider and broader spool of around 15 cm diameter is used. Thus, the bending radius is reduced and the fiber was only wound in a single layer around the spool, avoiding excess stress when crossing.

4.4 Interfacing the resonator

In the experiment, we inject three individually controlled light fields into the resonator. There is 852 nm probe light with a maximum power of $1\,\mu\mathrm{W}$ and approximately $30\,\mu\mathrm{W}$ of lock light, both derived from the same laser locked to the D2 cycling transition of Cesium. Furthermore, there is heating light at 780 nm at around $500\,\mu\mathrm{W}$ present in the resonator to keep the nanofiber surface hot and reduce the probability of Cesium adsorption. A detailed description of the laser specifications can be found in chapter 5.

Our experimental sequence alternates between preparation of the ensemble of laser-cooled atoms and probing them, while during the longer preparation phase the resonator is locked. An example sequence for this interleaved locking is shown in Fig. 4.6. The probing intervals are sufficiently short, such that the free running resonator is barely moving, and the lock can easily continue after the short pause. The interleaved locking is necessary to prevent the intense lock light to enter the detection setup, eventually saturating and possibly destroying our single photon detectors. The optical setup for mixing and injecting all light

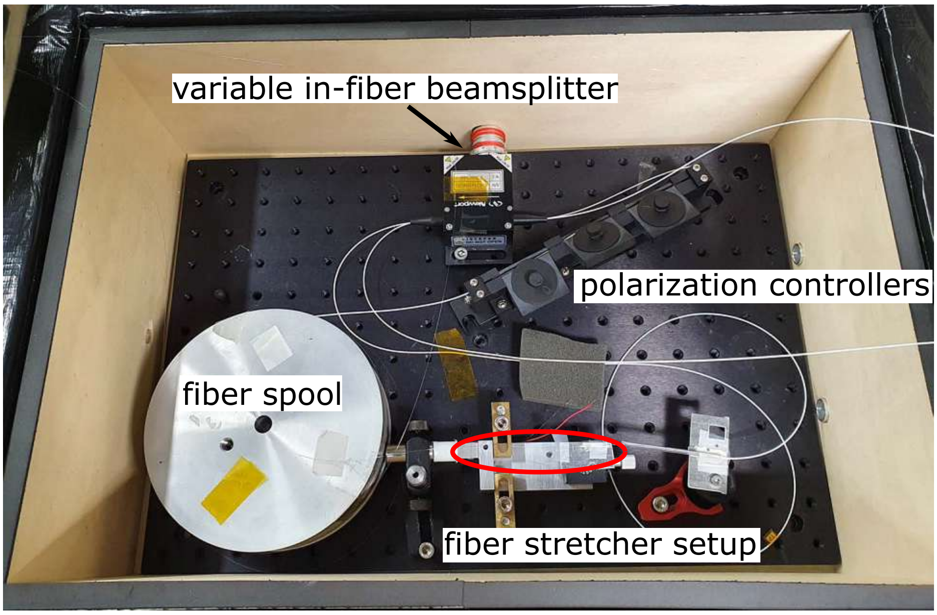

Fig. 4.5 Picture of the insulating box with a sturdy breadboard, the fiber spool and the stretched fiber on the fiber stretcher indicated in red. All loose fiber-parts as well as in-fiber polarization controllers are fixed to the breadboard. The resonator and the box have been assembled as part of the bachelor thesis [101].

fields into the resonator and separating them at the output, including the detection and locking setup is detailed in Fig. 4.7.

Lock, probe, and heating lasers are overlapped using a 50:50 beamsplitter and a dichroic short pass mirror before injecting them into the resonator. On the resonator output we use an acousto-optical modulator (AOM) to switch between guiding light towards the locking and the detection setup. A second detection setup to detect light that is reflected from the coupled atom–resonator system is installed at the resonator input, accessible via a 90:10 beamsplitter, where the 90% port guides light reflected from the resonator towards the backwards detection setup.

In both detection setups a volume Bragg grating (VBG) is installed to filter 852 nm light from the background, mostly consisting of the 780 nm heating light. In the forward detection a 50:50 beamsplitter divides the light onto two single photon counting modules (SPCM). Each SPCM is equipped with an 852 nm bandpass filter to avoid spectrally broad light that is emitted during the SPCM's electron avalanches to scatter back into the setup and the other SPCM. In backwards direction one SPCM is sufficient for our intended measurements.

The lock setup too consists of an 850 nm longpass filter to filter out the 780 nm heating light as well as of two waveplates and a polarizing beamsplitter adjusted such that they separate the resonator's eigenpolarizations onto two arms with a photo diode in each arm. The detected signals are used for the generation of the error signal for the resonator's lock.

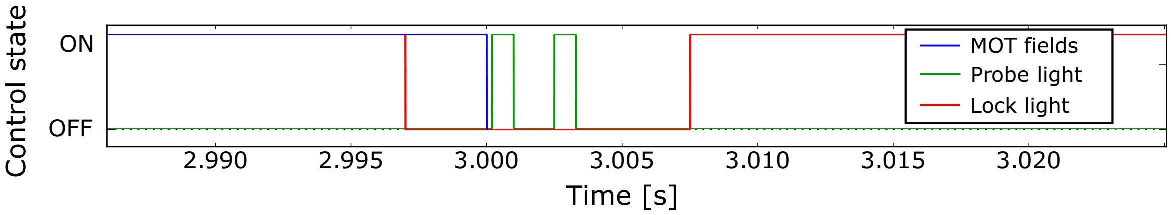

Fig. 4.6 Sequence for interfacing the resonator, depicting the status of each field versus the sequence time. Shortly before the preparation of the atomic ensemble is finished (blue), the resonator lock light is switched off (red). At the same time, an AOM deflects the light leaving the resonator towards the detection setup, where the photon detectors are switched on. During the two consecutive resonant probe pulses (green), all fields except of the heating laser are kept off. When the probing is done and the detectors are switched off, both, the lock light and the AOM are brought back to their initial configuration.

4.5 Characterization of the resonator

In this section I summarize the most important characteristics of the two resonators that were used throughout the course of this thesis.

4.5.1 Resonator 1 - TU Wien

The first implementation of our fiber ring resonators, having a length of $l \approx 27.5\,\mathrm{m}$, was characterized without an integrated nanofiber. By scanning the probe light with an AOM across several free spectral ranges of the resonator, we recorded spectra on a photodiode using a high bandwidth oscilloscope. First, the resonator was critically coupled by setting the beamsplitter such that the transmission dips of the scanned light reached a minimum transmission $T \approx 0$. By fitting the transmission of an empty resonator to the spectra, we inferred a finesse of 37.5 and a free spectral range of $\nu_{\mathrm{FSR}} = 7.51\,\mathrm{MHz}$. From this we could determine the roundtrip loss of the critically coupled resonator to be 8.4%. We attribute this loss to insertion loss in the variable fiber beam splitter (2.5% according to the manufacturer's specification), bending loss in the 6.4 cm diameter fiber spool (4%, measured) and propagation loss including the four in-loop fiber splices (total of 1.9%, inferred via subtraction).

In a next step, the resonator was cut open and the optical nanofiber, that was placed inside the vacuum chamber before, was spliced into the resonator. The nanofiber insertion caused the total roundtrip loss to increase by 36.5%. A measured transmission spectrum for the resonator with integrated nanofiber is shown in Fig. 4.5. Up to this point, it is not exactly clear where the excess loss came from. The biggest threat to diminishing the transmission through the nanofiber are dust particles and similar small pollutants that settle on the waist or taper during fiber installation. In the worst case such a pollutant can cause fusing of the waist when fiber guided light heats up the particle. Without sufficient heat dissipation channels, like it is the case in an UHV environment, the temperature of such a particle can exceed the

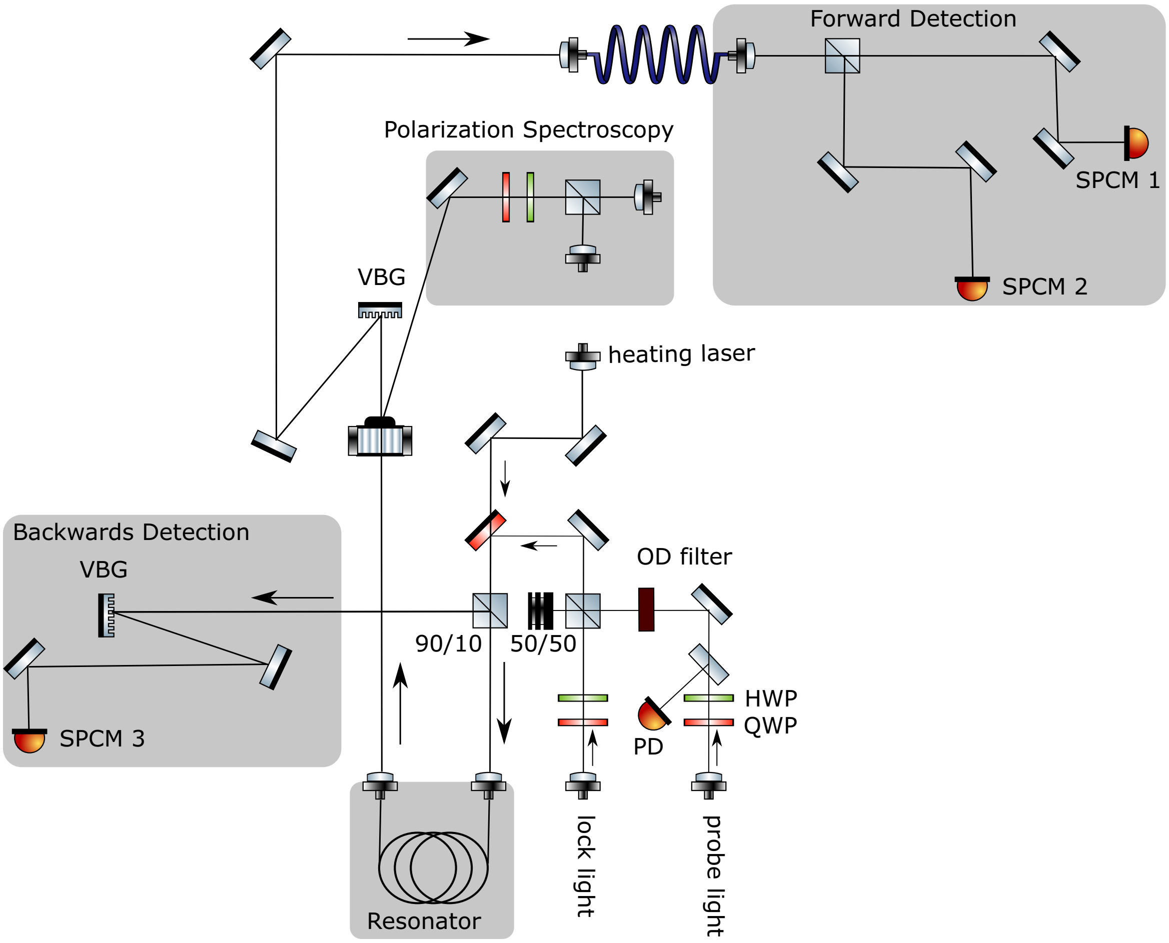
Forward Detection
Polarization Spectroscopy
SPCM 1
SPCM 2
VBG
heating laser
Backwards Detection
VBG
OD filter
90/10
50/50
HWP
QWP
PD
SPCM 3
Resonator
lock light
probe light

Fig. 4.7 Optical setup around the resonator. On the bottom we see the mixing of resonant, strongly attenuated probe light with the lock light, both being injected into the resonator. During the MOT preparation the AOM at the resonator output guides the lock light into the polarization spectroscopy arm, while during probing, the lock is switched off and the AOM guides light towards the detection setup. Notice, both detection setups are equipped with a volume Bragg grating (VBG) to filter out the 780 nm heating light.

melting point of silica. To circumvent this from happening the fiber insertion is performed in clean environments (see chapter 5 for details).

Other candidates that can explain the discrepancy of the resonator roundtrip losses before and after evacuation are switching on the ion pump and Cesium dispensers, which might have sputtered unknown pollutants onto the tapered fiber. Furthermore, Cesium is known to adsorb on the nanofiber, which is why we took care that there was always blue-detuned heating light of around 500 μW injected into the fiber. Experience showed that a hot nanofiber is less likely to adsorb Cesium.

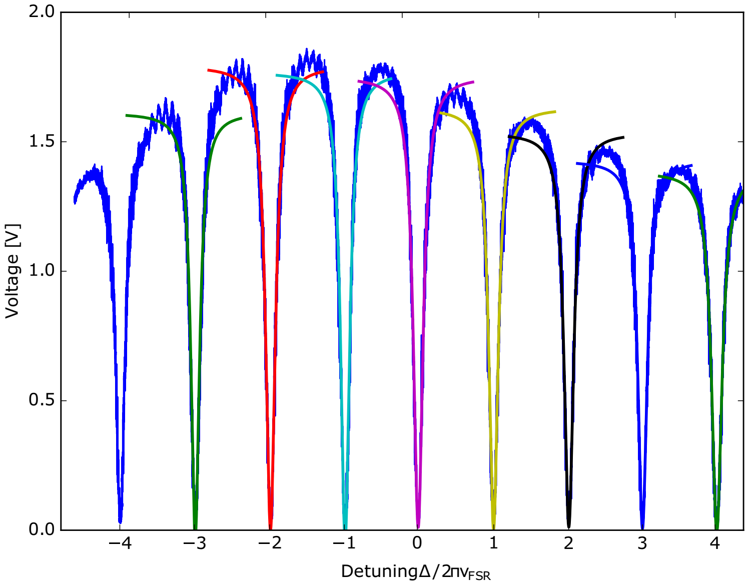

Fig. 4.8 First measured transmission-spectrum of the resonator in Vienna including the nanofiber. This measurement was conducted using a photodiode at the output of the resonator, before we installed an intensity calibration of the probe laser. To obtain the cavity's characteristics, we fitted Lorentzian functions to each individual resonance. The finesse has been inferred to be 6.64 ± 0.07.

To conclude, presumably, the sudden increase in loss must have happened, due to a pollutant settling on the waist of the nanofiber, which remained unnoticed during fiber installation, moving the chamber to its final position or chamber pump down, where switching on the ion gauge and pump could have outgassed some detrimental pollutants. Furthermore, final tightening of the ferules, getting the chamber UHV tight, could have caused either excessive stress induced loss or bending loss from twisting the fiber ends tightly around each other. In principle, however, we can conclude from our measurements that it should be possible to prevent such detrimental effects from occurring, which is why we decided to exchange the fiber after the move to Berlin.

4.5.2 Resonator 2 - HU Berlin

In Berlin, we replaced the nanofiber inside the chamber and spliced it to an upgraded longer resonator of 43.4 m length. This setup comes with a bigger metallic spool for mounting the resonator fiber, reducing bending losses and a newer version of the variable beamsplitter, that we experimentally found to have a more reproducible setting of the coupling ratio. Note that after a year of daily use, we noticed some hysteresis of the setscrew of the initially installed variable beamsplitter.

The updated resonator was built as part of a Bachelor's thesis and a finesse of 25.2 and a free spectral range $\nu_{FSR} = 4.8\,\text{MHz}$ were measured [101]. To identify the origin of the resonator losses, we monitored the resonator transmission spectrum while mounting the fiber

Die approbierte gedruckte Originalversion dieser Dissertation ist an der TU Wien Bibliothek verfügbar.
The approved original version of this doctoral thesis is available in print at TU Wien Bibliothek.
TU Bibliothek WIEN Your knowledge hub

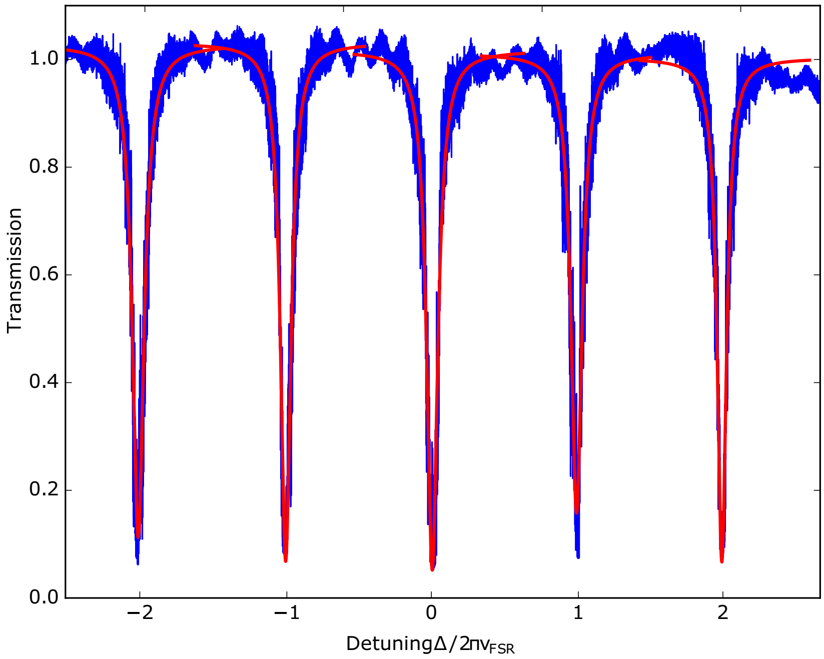

Fig. 4.9 Measured transmission-spectrum of the resonator in Berlin including the nanofiber. To obtain the cavity's characteristics, we fitted Lorentzian functions to each individual resonance. The finesse has been inferred to be 11.40 ± 0.10.

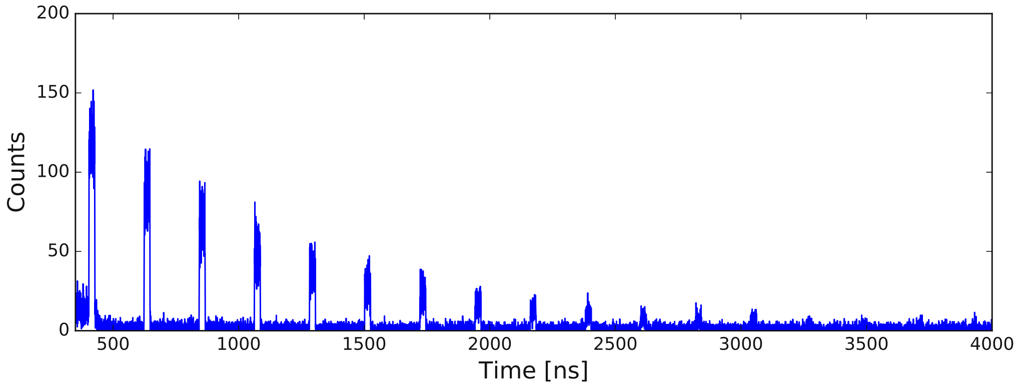

Fig. 4.10 Pulse-train measured at the output of the critically coupled resonator in Berlin, after sending a 25 ns pulse. The counts decay proportional to $\exp(-nF/2\pi)$, where n is the number of roundtrip, agreeing well with the fitted finesse.

into the vacuum chamber and during evacuation. The idea was to characterize losses inflicted from tightening the Teflon ferules during pumpdown of the chamber as well as switching on the Cesium dispensers. To do so, before pumpdown, we mounted the new nanofiber into the vacuum chamber and spliced it into the resonator. This step reduced the resonator's finesse to 11.40 ± 0.10. After the Teflon ferules were tight and the chamber pumped down to almost 10^{-10} mbar we measured $F = 11.24 \pm 0.17$. After trapping the MOT, i.e., when the fiber was exposed to Cesium, the finesse settled at 10.01 ± 0.077 after which it remained stable for the next months. From the final finesse, we infer total roundtrip losses of 31.4%, an increase of 18.9% compared to the resonator without optical nanofiber. Note that although there has been only very little degradation of finesse during the pump down, activation of Cesium amounts for at least 5.3% loss. Furthermore, from this calibration, we infer the transmission through the nanofiber to be 85%. The initial transmission after nanofiber production and gluing to the fiber mount was 98.2%. Note that this 85% transmission includes losses from two splices where there is a fiber type mismatch between the nanofiber part and the rest of the resonator. A possible reason for the low fiber transmission can be the almost 4 months of storage of the fiber in a sealed box before installation[2]. We know fibers have been shipped successfully all over the world via mail in such boxes, still, it is possible that at some point in time a scatterer was deposited on the nanofiber part. A summary of characteristics of all resonator implementations can be found in table 4.1.

	length	ν_{FSR}	linewidth	finesse	L_{rt}	$\kappa_0/2\pi$
res 1, no ONF	27.5 m	7.5 MHz	200 kHz	37.5	8.4%	0.05 MHz
res 1, inc. ONF, Cs on	29.3 m	7.1 MHz	1.07 MHz	6.6	47.28%	0.27 MHz
res 2, no ONF	43.4 m	4.8 MHz	190 kHz	25.2	12.45%	0.048 MHz
res 2, inc. ONF	45.5 m	4.6 MHz	412 kHz	11.4	27.6%	0.103 MHz
res 2, inc. ONF, Cs on	45.5 m	4.6 MHz	459 kHz	10.0	31.38%	0.114 MHz

Table 4.1 Summary of resonator characteristics before and after including the nanofiber as well as before and after Cs exposure to the nanofiber. The roundtrip loss inside the fiber has been calculated to be π/F. Note, for the calculation of κ_0, we assumed a critically coupled resonator, $\kappa = \kappa_0 + \kappa_{\mathrm{ext}}$.

4.6 Discussion

4.6.1 General discussion of implementation of the resonators

Lock stability and resonator interfacing While performing initial measurements we soon noticed that there are some limits to the lock's performance. For the initial resonator implementation, probe and lock light were taken from the same laser that is also used for the magneto optical trap. Using Pound-Drever-Hall we stabilize this laser using an error signal derived from a Doppler-free atomic spectroscopy. This stabilization requires a fast modulation of the laser current to generate the frequency sidebands for the error signal. These sidebands caused distortion of the laser's linewidth to a point where it was impossible to resolve the cavity resonances fully. Instead, using the spectroscopy signal directly, locking to the positive slope of the spectroscopy signal of an atomic transition (so-called side of fringe locking), the measured resonator linewidth was decreased. We noticed though, that this locking scheme came with reduced long-term frequency stability of the laser since it depends on its (slowly changing) output intensity.

---

[2] Before moving to Berlin, it was unclear when to expect the fiber pulling rigs to be fully operational. To arrange for the nanofiber replacement independently from the setup of the rigs, this nanofiber was still pulled in Vienna.

Resonance fluctuations During the first test of the lock's performance on an empty resonator without an optical nanofiber, we observed erratic fluctuations distorting the spectral features in our transmission measurement. The source of this behaviour could be identified to be mechanical excitation of our master laser. Using a portable speaker, we acoustically excited different parts of the setup, such as the optical setup, resonator housing and parts of the vacuum chamber. By sweeping the acoustic frequency we observed a significant increase of resonance fluctuations in the transmission spectrum for an excitation at 140 Hz, when pointing the speaker directly at the external cavity of the laser. When not actively excited, the resonance fluctuations are on the order of the resonator's linewidth, which causes broadening of our spectra, when accumulating data of several experimental realizations. To counteract this broadening, we pre-processed our data before in-depth analysis. To this end, we took the individual empty resonator spectra of each experimental realization as a reference to shift and overlap the recorded coupled atom–resonator spectra before averaging. Note that by doing so, effectively we fix the laser–resonator detuning, but in turn introduce an uncertainty in the atom–resonator and atom–laser detuning. Nevertheless, this uncertainty is less detrimental to fitting theory to the empty resonator transmission spectra than without this overlapping algorithm. This could be seen by the overall smaller linewidth and deeper resonances after this pre-processing of data.

Updated laser and lock Fortunately, broadening due to distortion of the spectral features in our transmission signal originating from the laser became obsolete when upgrading the experiment to a separate probe laser. Furthermore, this laser is equipped with an additional narrow interference filter inside the external laser cavity, reducing the linewidth of our probe light by a factor of 5. This laser is locked via the Pound-Drever-Hall method by modulating the laser frequency in a separate arm using an EOM. Additionally, with the higher Q resonator realized in Berlin, we also updated the resonator's lock. This upgrade resulted in a much smaller laser linewidth, got rid of the parasitic modulation from the laser's lock and realized a more stable resonator. This allowed for overall better resolution when interfacing the resonator, resulting in narrower and deeper spectral features when measuring transmission spectra.

Nevertheless, with the narrower laser and resonator linewidth we observed smaller and faster oscillations that could not be seen in the initial experimental setup. These perturbations presumably originate from heating of the nanofiber, thus exciting fast vibrations or torsion in the waist of the nanofiber [102, 103]. The amplitude of the oscillations depends strongly on the power of fiber guided lock light and reduces on the order of minutes when switching the lock light off. By installing more sensitive photodiodes into the polarisation spectroscopy setup we could reduce the required level of lock light significantly. Furthermore, with the updated lock setup in Berlin, the lock's bandwidth was increased, thus we could reduce the amplitude of these residual oscillations drastically. Note that still if we increase the power of lock or heating light during the measurements above a certain threshold, the lock will fail, because the fast erratic resonance shifts become to large for the lock actuator to counteract. This will make it necessary to upgrade to a different locking method that can react much faster if more powerful light fields would be used, for example, when implementing dipole-trapping of atoms close to the nanofiber.

Interleaved locking Here, I want to discuss a minor shortcoming of the interleaved locking method. The lock is switched off about 2 ms before probing the resonator in normal sequences and is switched back on after probing, where the resonator can drift for about 10 ms that the lock is switched off (compare Fig. 4.6). We measured the frequency shift of the resonator to be about one resonator linewidth ($\leq$ 500 kHz) during this time by comparing the probe spectra to the reference spectra recorded at the beginning and the end of the probe sequence. As this shift is small compared to our typical signal width, we did not further improve this behaviour, especially since for the first probe pulse, where we interface the atomic ensemble, the resonator-laser detuning was measured to be less than 100 kHz.

Influence of splicing and fiber types It is evident that a significant degradation of finesse for both resonators must have happened during the installation of the nanofiber. We cannot say with certainty that a scatterer on the fiber is the reason for this loss, although it is the most likely candidate. We cannot say at what point in time the pollution (could have) occurred due to the technical inability of uninterruptedly monitoring the transmission through the nanofiber for the whole process of fabrication and insertion into the chamber. Other sources of loss, such as bending radii and local stress, where mostly identified and reduced during the experimental update of the nanofiber and the resonator including its lock.

Something that still remains to be carefully quantified is the importance of splicing quality. Throughout testing several implementations of the resonators, we noticed that the induced loss from splicing can vary drastically from try to try and can reach up to 20% loss per splice, inferred from successive finesse measurements after re-splicing the resonator. These observations were confirmed by several group members working on different experiments, using a variation of fiber types. Note that most commercially available splicing devices are optimized for Telecom-wavelength fibers with a core diameter of 9 μm. Although our high-end splicer has been optimized for splicing near infra-red single-mode fibers, we noticed that it is not capable of correctly imaging the fiber core of 4μm diameter, a prerequisite for optimal core alignment of the cleaved fiber pig tails. Furthermore, we do not know whether splicing of different types of optical fiber is detrimental regarding loss.

For resonator 1, the fiber ring and nanofiber both were made from *Fibercore SM800 (5.6/125)*, specified with a 5.6μm mode field diameter at 830 nm. The fiber inside the variable beam splitter is presumably a *Corning HI780*[3] with a 4μm core diameter. We noticed that splicing different fiber types definitely has a higher likelihood of resulting in lossy splices than using the same type. The reason might be the change of core or mode field diameter, possibly leading to a mode mismatch and scattering of cladding guided light before merging into the single-core-mode. Moreover, we experienced our patch of *Fibercore SM800(5.6/125)* fiber is way more sensitive to mechanical instability such as bending and twisting regarding loss, compared to other fibers. Therefore, the second resonator was entirely built from *Corning HI780* fiber, where we believe it matches the fiber in the beamsplitter and is in general more stable. Nevertheless, the nanofiber was still produced from *Fibercore SM800(5.6/125)* since we were under a time constraint before the move and had no optimized trajectory for pulling the corning fiber at that time. Building the next resonator generation entirely from the same type of fiber and further optimizing our splicing routine for smaller core single-mode fibers should allow to significantly increase the resonator finesse.

---

[3] Newport support did not want to clarify

4.6.2 Length considerations for the resonators

Finally, to calculate for which resonator lengths we enter the regime of single-atom or multimode strong coupling, we can use the relation $g_N^2 = 2\beta\gamma\nu_{\mathrm{FSR}}$. Here, g_N is the required collective atom–resonator coupling strength, $\beta\gamma$ is the photon emission rate from the atom into the resonator and ν_{FSR} the free spectral range of the resonator (see chapter 2).

To reach the regime of single-atom strong coupling, for which $g > \gamma$ is required, we need to fulfil $\nu_{\mathrm{FSR}} > \frac{\gamma}{2\beta}$. For our channelling efficiency $\beta = 0.005$ (for details see 5.5) such a resonator must have a length of at most 13 cm length. This is not achievable with our resonator design.

More important for us, is the limit of reaching the multimode strong coupling regime $g_N/2\pi > \nu_{\mathrm{FSR}}$, for which we can formulate the condition

$$\nu_{\mathrm{FSR}} < \frac{\mathrm{OD}}{8\pi^2}\gamma_l. \tag{4.7}$$

For our experimental setup we estimated from experience to be able to achieve single-pass optical densities of nanofiber-coupled cold atoms in a magneto optical trap to be OD $\approx$ 35. For this OD, a resonator with a free spectral range of $\nu_{\mathrm{FSR}} \approx 7.2$ MHz, being below 30 m long, would just enter the multimode strong coupling regime. Thus, for our first resonator we decided to implement a circa 30 m fiber ring, where we eventually replaced it by a longer resonator once we have tested and improved the locking mechanism and upgraded to a laser of narrower linewidth compared to the one we used at the beginning of setting up the experiment. The upgraded, longer resonator built in Berlin ($\sim$ 45 m) allows for entering the multimode strong coupling regime already for optical densities as low as OD $\approx$ 22, which can place us deeper into this regime for the optical densities achievable in our setup.

Chapter 5

Experimental setup

Conducting the experiment presented in this thesis, required the assembly of a new setup, intended as a continuously operating experimental apparatus for several generations of researchers. In this chapter I will discuss details of the implementation, the original ideas behind the design, important benchmarks, suggestions for further improvements as well as mention a few particularities of this setup. Note that the experimental design is inspired by a twin setup in this research group, presented in [104, 105], where I spent a year during my masters project, setting up and characterizing the magneto-optical trap (MOT) setup as well as designing a setup imaging the MOT and the nanofiber [106]. The base design for the vacuum chamber and the optical and magnetic setup of the MOT in the experiment introduced in this thesis have been replicated and improved upon the experience gained in the twin experiment during initial set up and first year of operation.

In this chapter, I will outline the vacuum chamber design, centred around a glass cell hosting the nanofiber, elaborate on the MOT setup and introduce the methods used for monitoring the MOT's size and optical density of the nanofiber coupled atomic ensemble. Finally, I will summarize the current implementation of the laser setup and discuss the experimental control hard- and software.

5.1 Vacuum chamber and glass cell

Creating a dense cloud of cold atoms requires an ultra-high vacuum (UHV) to avoid heating of the laser cooled atoms due to collisions with atoms not participating in the cooling processes. To this end, our chamber is designed to achieve base pressures as low as 10^{-10} mbar. The attached glass cell provides good optical access, while at the same time allowing the magnetic coils to be very close to the optical nanofiber (ONF), minimizing required currents for appropriate trapping fields.

5.1.1 Chamber design

The 30 cm diameter main chamber[1] hosts the connections for the vacuum pumps, an ion gauge, and an attachment for the Cesium dispensers (see Fig. 5.1). The front flange of the chamber has the glass cell attached, which hosts the nanofiber. The back flange hosts the mount for the fiberholder as well as optical and mechanical feedthroughs. Note that for orientation in the experimental setup, all directions are referenced to the vacuum chamber. The base is given by the fiber axis with the other two directions being referred to as vertical and horizontal.

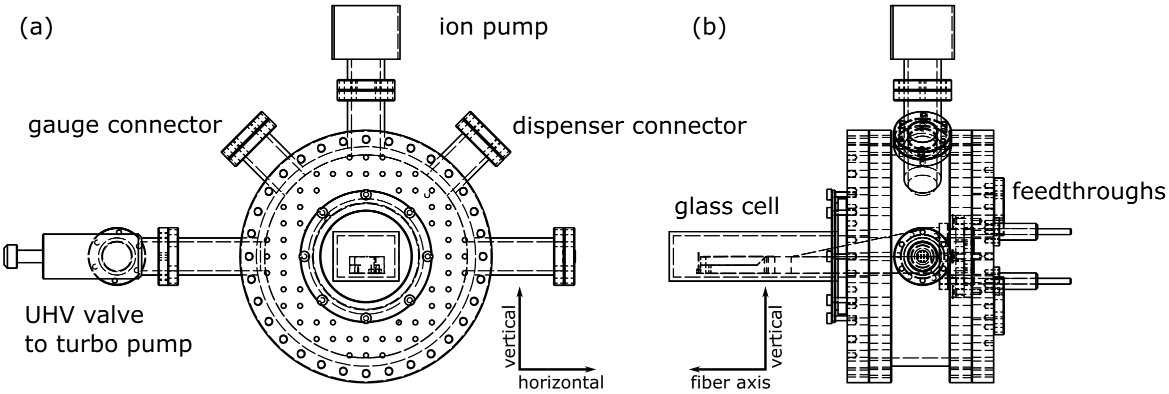

Fig. 5.1 (a) Front view of the main chamber with the attachments for the turbo pump, ion gauge, ion pump and Cs dispensers. (b) Side view of the chamber, where one can see the attached glass cell in the front and the mechanical feedthroughs in the back.

The initial pump down of the chamber is performed by a turbo pump[2] achieving high vacuum (up to 10^{-8} mbar), where the final pressure is achieved using an ion-getter pump[3] accomplishing UHV pressure. In order to reach low final pressure, the chamber was baked while pumping for a full week, where we took care to slowly change temperatures in order to prevent temperature gradients, especially across the attached glass cell. During cooling, a full metal UHV valve between the turbo and the main chamber is closed and the chamber is only pumped by the active getter material of the ion getter pump. The achieved pressure before using the Cesium dispensers was measured to be below the ion gauge measurement range, specified down to 10^{-10} mbar.

Monitoring the pressure inside the chamber is done by conversion of the measured ion pump operation current or an additional ion gauge[4]. The parallel measurement is necessary, since the ion pump tends to form Cesium whiskers connecting the filaments in the pump, eventually leading to an unexpected high measured current, where we observed temporary mismatch between the pressure readings of the pump and the gauge of up to 2 orders of magnitude. Furthermore, the ion pump is positioned behind the getter material so it will always measure a different environment than the ion gauge. Most importantly, the additional ion gauge is necessary during bake-out of the chamber and activation of the getter material inside the ion getter pump to know the pressure during this procedure. Note that during getter activation the ion pump needs to be switched off.

---

[1] CF250 flange

[2] Pfeifer - HiCube Eco 80 DN40 ISO-KF pump stand incl. pre- and turbo pump

[3] SAES - Nextorr D100-5

[4] Vacom - ATS40C

To provide the Cesium background inside the vacuum necessary to load the MOT, we use alkali metal dispensers[5]. A controlled and reproducible alkali evaporation rate can be assumed, when providing a calibrated current across the dispensers [107]. Note that the MOT is loaded solely from background Cesium in the chamber. Using an electrical vacuum feedthrough, five dispensers are connected in a star configuration to ground, to be used one after each other, preventing the need of reopening the chamber, once a dispenser is empty. The dispensers are heated using a programmable current source, usually ramping up the current in the morning to a fixed value and switching off the current during the night (unless there is ongoing measurements) to prolong the dispenser lifetime, that can be used like this for about a year before it needs replacement. In case all dispensers are empty, there is an UHV gate valve between the main chamber and the dispenser attachment. The valve has been installed such that the closed valve maintains UHV inside the main chamber. To prevent the chamber and nanofiber from being contaminated during dispenser activation, the whole bundle of dispensers was activated during initial baking after which the UHV valve has been closed for fiber insertion. When inserting the nanofiber, we noticed that this valve does not work equally well in both directions. Note that the valve's manufacturer specifies a vacuum side, which we put facing the main chamber. Thus, for fiber insertion, when the dispenser chamber should remain evacuated, but the main chamber is under ambient pressure, the valve is mounted the wrong way around. After the fiber has been inserted and we pumped the main chamber down again we re-opened this valve and observed an increase of chamber pressure for about 5 minutes for ~ 2 orders of magnitude. Nevertheless, afterwards the pressure came down quickly again and we reached base pressure, where we could establish a MOT.

5.1.2 Glass cell and fiber arm

At the centre of the experimental setup, there is a mirror mount like construction with an attached arm, reaching into the glass cell, as can be seen in Fig. 5.2. On the end of this arm the fiberholder containing the nanofiber is attached. The mount is screwed to the inside of the back-flange of the chamber allowing pivoting the fiberarm using two micrometre screws fed through the back of the metal chamber. This way, the construction allows to overlap the waist of the nanofiber with the cloud of cold atoms optimally, which enables us to reach optical densities of the nanofiber-coupled ensemble exceeding $\mathrm{OD} = 50$.

We use a rectangular glass cell of dimensions (83x63x216) mm on a 15 mm thick glass foot of 135mm diameter, that is attached to the front of the chamber using an indium seal between the chamber wall and the cell in order to make the contact UHV tight [108]. To keep the cell in place the glass foot is pressed against the seal using an aluminium ring and Viton as a buffer (see Fig. 5.2(c)). The chamber itself is joined together via optical bonding and is anti-reflection coated for 850 nm on the outside[6].

---

[5] SAES - CS/NF/12.8/40 FT10+10

[6] manufactured by Hellma-Analytics

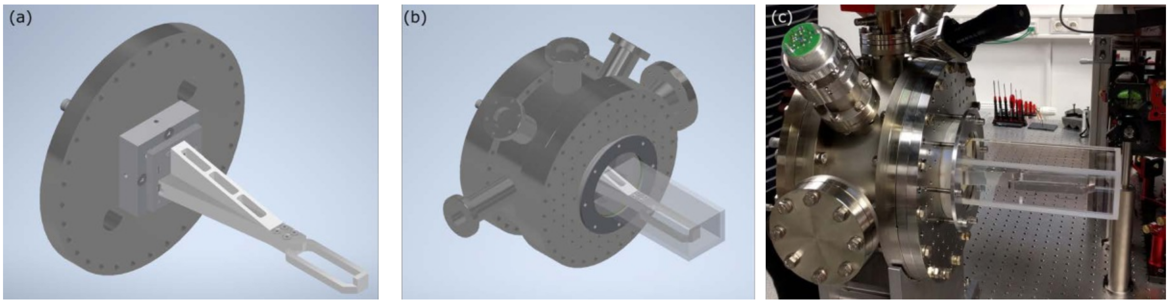

Fig. 5.2 CAD image of the fibermount. (a) The fibermount is attached to an extended arm, connected to a mount on the inside of the back flange. Two mechanical feedthroughs allow for precise placement of the fiber in the chamber to maximize the overlap with the MOT. CAD image (b) and assembled vacuum chamber (c) with glass cell and the fibermount.

During the first attempt of sealing the glass cell the foot of the glass cell broke off. Presumably we applied too much strain across the foot due to uneven tightening of the screws pressing the cell against the chamber. Since the rectangular part of the cell broke clean off the glass foot, we glued the cell using epoxy[7]. Curing was done in a new, carefully cleaned oven, where we took special care to keep the temperature stable and ramp it slowly to prevent local temperature gradients along the cell. The attempt turned out to be successful – the aforementioned best base pressure was achieved with the glued class cell.

5.1.3 Insertion of nanofiber

The most important requirement for a successful experiment is the installation of a nanofiber without detrimental pollutants on the waist or taper, that otherwise could lead to excessive loss or in the worst case, fusing of the fiber due to local heating at the absorber, where the fusing temperatures have been determined in [109]. In order to minimize the probability of contamination, the fiber is pulled, handled and installed exclusively in flow boxes providing a laminar flow of filtered air (see Fig. 5.3).

For the first nanofiber, that was pulled and installed into the chamber in Vienna, the chamber sat next to the pulling rig and the fiber could be installed without delay right after being pulled, which is the preferred method, where the fiber installed in Berlin was pulled and stored in a sealed plastic box for transportation. Nevertheless, for both fiber installations, we mounted a portable flow-box around the vacuum chamber, such that especially the chamber opening is always shielded well from dust in the environment. To hold the heavy back flange in place we attached an aluminium cage to the flange. This aids in lifting it up, prevents it against tipping over and allows us to slide the back flange exactly into position to align the knife edges of the CF-flanges.

Starting from an opened chamber, inserting the nanofiber is done by mounting the fiber holder with the attached nanofiber to the fiber arm using non-magnetic steel screws. Secondly, the aluminium cage is used to slide the back flange with the fiberarm halfway into the glass cell, shielding the fiber from the environment and protecting it against pollution. The fiber pigtails are each fed through a Teflon ferule carefully pressed into a through-hole connector[8] on the back flange using a restraining nut [110]. By tightening the ring, the Teflon is pushed into the conic feedthrough, closing the tiny holes around the fiber. For the second nanofiber, we spliced the fiber pigtails to the adjustable fiber-beamsplitter to form a resonator already during nanofiber installation, shortly before tightening the ferules. This way we could measure transmission spectra and infer the resonator's finesse at regular intervals during tightening of the ferules and chamber pumpdown (for details see chapter 4). Finally, the chamber is closed by sliding the back flange towards the main chamber and connecting the flanges. Note that closing the upright standing heavy back flange is quite challenging to close UHV tight, which is why we used thin metal sheets of several micrometre thickness in combination with torque drivers to prevent uneven tightening.

---

[7] Epo-Tek H77

Once the fiber is installed, we begin the pumping process by pumping down the chamber via the pre-pump through a tiny needle valve to limit the pumping speed, preventing any turbulence inside the chamber that could harm the fiber or stir up dust particles. Once the pressure is not reducing any more the needle valve is bypassed by a larger opening valve. At the same time, the turbo pump is switched on and we continue with our pump down procedure, including ion-getter pump activation. After approximately a week of pumping we observed a steady pressure. The Cesium dispensers, that were activated during chamber bake-out, are switched on and we commenced with operation of the MOT setup.

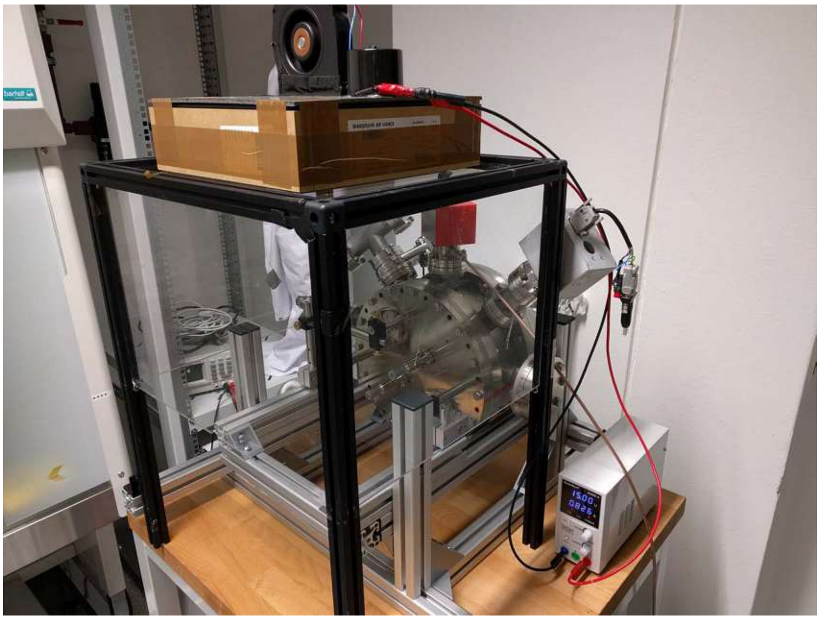

Fig. 5.3 Flowbox assembly on top of the aluminium rig to allow opening and closing the vacuum chamber carefully. Note that the setup is right next to the fiber pulling flowbox to minimize exposure of the nanofiber to unfiltered lab air.

---

[8] Swagelock 1/4" connector

5.2 Magneto optical trap

The MOT in our experiment provides an ensemble of cold atoms, where we estimated in a previous chapter (4.6) it was necessary to achieve optical densities above OD ≈ 35 for the nanofiber coupled atomic ensemble. Our approach with the setup design is the generation of a strongly elongated MOT that aligns along the nanofiber axis to increase the overlap between the waist of the nanofiber and the atomic ensemble. This way the distance the nanofiber guided light runs through the atomic ensemble can be maximized, thus maximizing the clouds optical density. With this method, we can achieve a MOT that has up to an OD ≈ 50 for fiber guided light (see chapter 6). The MOT extends around 5 mm along the nanofiber after loading and will be stretched shortly before interfacing to cover the whole 1 cm of the nanofiber waist. The diameter across the cold atom cloud is at most ~ 3 mm, measured with the calibrated imaging setup, and mostly depends on the amount of Cs in the chamber.

Furthermore, an absorption imaging system has been installed to measure the approximate number of atoms in our MOT and allows for time-of-flight measurements. The temperature of the MOT was measured after initial optimization to be $80 \pm 2\mu$K, reported in detail below.

5.2.1 Principle

The idea of a magneto optical trap is to combine laser cooling using the right choice of polarization and an overlapped magnetic field gradient to trap and accumulate cold atoms. For complete discussion of the underlying cooling processes see [19, 111, 112].

1D cooling The laser cooling of an atom is facilitated by a force due to momentum transfer from repetitive scattering of light. Considering an atom moving towards a laser beam, absorbing light from the laser and re-emitting it into full 4π-space, a recoil force in opposite to the direction of atom movement proportional to the atom's scattering rate R_{scatt} is applied to the atom. This results in a change of the atom's velocity depending on the atom-laser detuning. The force is given by

$$\begin{aligned} F_{\text{scatt}} &= \hbar k R_{\text{scatt}} \\ R_{\text{scatt}} &= \frac{\Gamma}{2} \frac{I/I_{\text{sat}}}{1 + I/I_{\text{sat}} + 4\Delta_a^2/\Gamma^2} \, , \end{aligned} \tag{5.1}$$

depending on $\Gamma = 2\pi \times 5.2\,\text{MHz}$ the Cs atom's decay rate, I_{sat} the saturation intensity and Δ_a the detuning from atomic resonance. To cool a moving atom along one dimension one needs two counter-propagating cooling lasers, each red-detuned to the atomic transition in order to compensate for the Doppler-shift of light seen by the moving atom. The force on the atom by one beam pair is given by

$$F_{\text{mol}} = F_{\text{scatt}}(\omega - \omega_0 - kv) - F_{\text{scatt}}(\omega - \omega_0 + kv) \approx -2 \frac{\partial F_{\text{scatt}}}{\partial \omega} kv \equiv -\alpha v \, , \tag{5.2}$$

and depends, for a given detuning, on the atom's velocity, which is why this is considered a friction force, giving this method the name optical molasses. The lowest temperature that can be reached using this method is called Doppler temperature, given by

$$k_{\mathrm{B}} T_{\mathrm{D}} = \frac{\hbar \Gamma}{2}, \tag{5.3}$$

which is $T_D = 125.61\,\mu\mathrm{K}$ for the Cesium D2 line [51]. At this temperature, the mean squared velocity of the atom has a minimum, where the sum of momentum of the isotropic spontaneously emitted photons is zero, i.e., there is an equilibrium between the cooling (absorption) and heating (re-emission) processes, that in the end solely depends on the linewidth of the cooling-transition.

1D trapping To accumulate the cooled atoms, the counter-propagating beams are overlapped with a magnetic field gradient, with a zero-crossing in the centre, as depicted in Fig. 5.4(a). For a simple description of the trapping process, we consider a two-level atom,

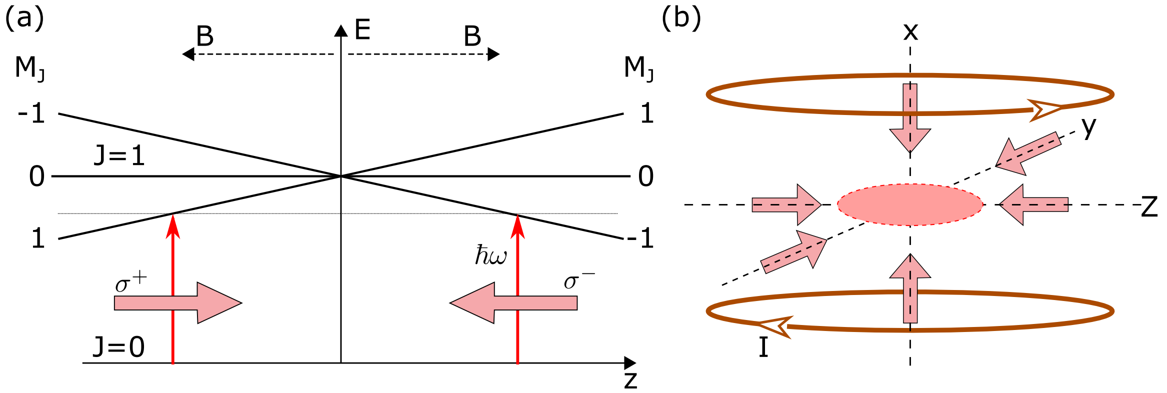

Fig. 5.4 (a) Scheme of the magnetic field leading to a position dependent splitting of the degenerate m_J sub-states. Circular polarized light can be absorbed, once the position dependent detuning is resonant with the atomic transition. (b) Sketch of a typical MOT setup, where three pairs of laser beams intersect the magnetic gradient field centre.

where we excite a transition $J = 0 \rightarrow J' = 1$, where J is the angular momentum of the atom. The magnetic field splits the m_J sub-states of the $J' = 1$ excited state, where the energy spacing changes with distance to the centre (see Fig. 5.4(a)). When using circular polarized light, the atom can be excited once the level-splitting and the velocity dependent detuning sum up to be resonant with the cooling transition. When this happens, the absorbed photon's recoil kicks the atom into opposite direction. This way, additionally to the aforementioned velocity dependent detuning force, now one also obtains a position dependent force. For red-detuning, the atoms will successively be cooled and trapped, thus accumulate around the centre of zero-magnetic field. The total position dependent force exerted on the atom by two counter-propagating beams (in 1D) is given by

$$\begin{aligned} F_{\text{MOT}} &= -2\frac{\partial F}{\partial \omega}(kv+\beta z) = -\alpha v - \frac{\alpha\beta}{k}z \\ \beta &= \frac{g\mu_{\text{B}}}{\hbar}\frac{\mathrm{d}B}{\mathrm{d}z}, \end{aligned} \tag{5.4}$$

where the first term accounts for the velocity dependent friction force introduced before and the second one for the position dependent trapping force. Here, μ_{B} is the magnetic moment of a single atom, g is the Landé factor and z the position of the atom.

3D cooling and trapping Ultimately, when one uses a configuration of three pairs of counter-propagating beams, atoms are cooled and trapped in all 3 dimensions, when entering the overlap region of all beams. Here, the cloud of cold atoms accumulates to be interfaced with the nanofiber later (see Fig. 5.4(b)).

Experimentally, we will cool and trap using the hyperfine transition $6^2S_{1/2}F = 4 \rightarrow 6^2P_{3/2}F' = 5$. While driving this transition, there is a probability for atoms to decay into the $F = 3$ ground state due to a finite probability of exciting the $F' = 4$ excited state with the red-detuned cooling laser. Therefore, a successful implementation of a MOT requires a second laser, the so-called “Repumper” pumping atoms from $F = 3 \rightarrow F' = 4$ from which they can spontaneously decay to $F = 4$ allowing these “dark” atoms to continue taking part in the cooling transition, as depicted in Fig. 5.5(a).

Sub-Doppler cooling There is an additional process that allows to cool the atoms below Doppler-temperature. Considering again a 1D scenario, the counter-propagating MOT-beams create a standing wave of position dependent polarization, thus, atoms moving along this standing wave experience a change in polarization, where their m_J sub-states split accordingly, as seen in Fig. 5.5(b). The atom will lose energy as it moves to a potential maximum, where the atom is likely to undergo a cooling cycle as described above, ending up in a lower laying m_J energy level. Moving further along the standing wave this process repeats, leading to an additional cooling mechanisms to take place, called Sisyphus cooling [19]. This process in principle allows the atom to be cooled down close to its recoil limit

$$k_B T_{\text{rec}} = \frac{\hbar^2 k^2}{M}, \tag{5.5}$$

which is $T_{\text{rec}} = 193.34\,\text{nK}$ for Cesium ([51]). This temperature corresponds to the kinetic energy imparted on the atom by the recoil of a single photon scattering event.

5.2.2 Experimental Realization

The experimental realization of the MOT setup consists of two parts, control of the cooling fields and a magnetic coil setup.

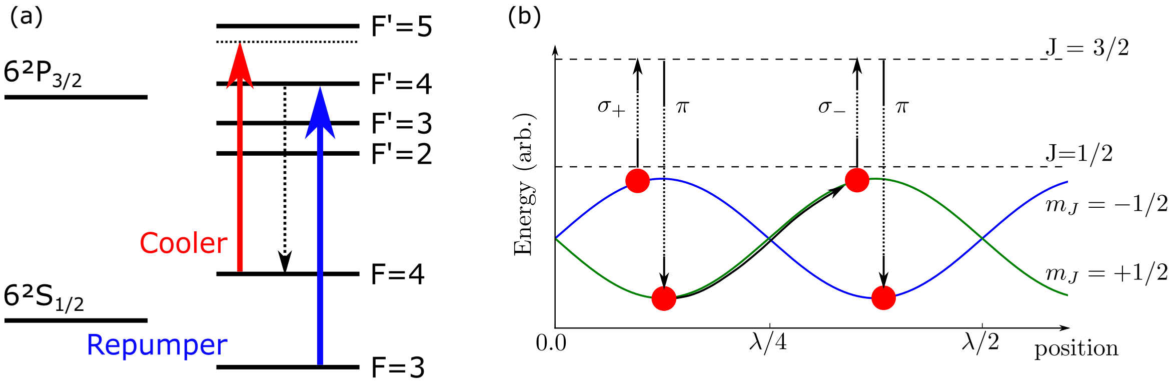

Fig. 5.5 (a) Atomic level structure of the Cesium D2-transition. The cooling light is red-detuned to the resonant transition to be resonant with moving atoms. The repump laser is necessary to pump back atoms to $F' = 4$ state to continue taking part in the cooling transition after undergoing spontaneous emission to $F = 4$. (b) Scheme of the Sisyphus cooling mechanism, where an atom moving to the right, runs up a potential hill and is optically pumped into a lower laying state. The energy-sublevel modulation is caused by the position dependent polarization standing wave.

Magnetic coils The design of the magnetic coil setup, depicted in Fig. 5.6(a) was developed by [104, 105] and consists of 3 pairs of coils. The design is intended to provide an elongated MOT cloud along the fiber waist to increase the number of atoms coupled to the nanofiber, which should be realized by elliptically shaped coils stretching the quadruple field. The main quadrupole field for trapping is generated by the two main coils ("MOT coils"), aligned along the vertical axis. The second pair ("bias coils") is aligned along the horizontal axis and is operated in Helmholtz configuration to manipulate the Zeeman-splitting between the m_F-sublevels of the ground and excited state in our probing transition. The last coil pair was intended to position the MOT along the waist of the fiber but was changed to be used in anti-Helmholtz configuration to stretch the atomic cloud along the waist even further.

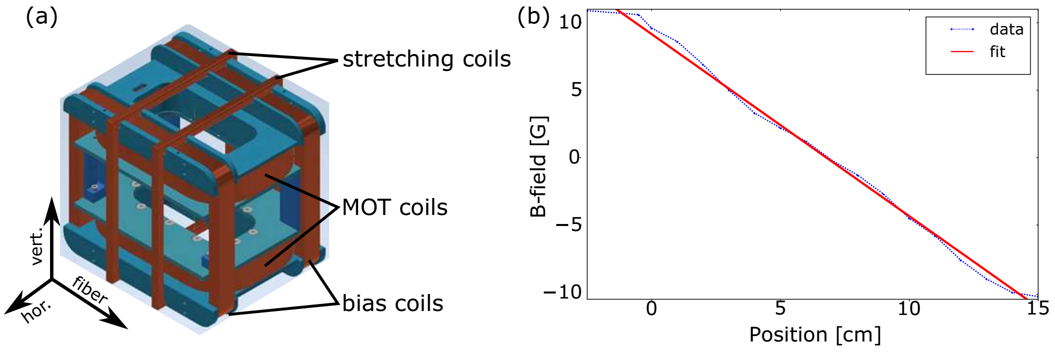

Fig. 5.6 AutoCAD of the magnetic coil holder including all coils (a) and the measured B-field along the vertical axis, paraxial to the MOT coils, for 2 A supplied to the coil pair (b).

Following feedback from the cited authors above, we slightly modified the design and reduced the number of windings to 112 for each MOT coil, 70 for the bias coils and 50 for the coils stretching the MOT along the fiber. By doing so, while using the same current drivers for the coils, we have a finer control of the magnetic fields and the size and weight of the constructed frame hosting the coils made handling and placing it around the glass cell easier. The design of the mount including all coils is depicted in Fig. 5.6(a) and placed inside the experimental setup shown in Fig. 5.7(a).

The field calibration (see Fig. 5.6(b)) of all coils was done supplying 2 A and measuring along the corresponding axis. For the quadruple field we measured a gradient of 1.35 G/cm with a maximum field of 100 G for 8.6 A measured at the centre of the top coil. For the mean field of the bias coils (orthogonal to the MOT coil and fiber axis) we measured 11.3 ± 0.3 G and for the field along the fiber axis, that at this time was operated in Helmholtz configuration, we measured a field of 6.5 ± 0.2 G. A linear scaling of the field for higher supply currents could also be experimentally verified. The additional compensation coils can supply up to 1 G in each direction, sufficient to compensate for the earth's magnetic background.

Note that by choosing a smaller number of windings we have to use twice the current for the same field gradient, resulting in twice the heating of the coils (assuming half the resistance of coils), which should however not lead to significant heat production that would require additional cooling of the coils. After setting up the experiment we measured the temperature during operation by placing a thermocoupler on the inside of the coil mounts, facing the glass chamber. We applied 10 A, the highest current our drivers can supply, to the main coils and 7 A to the bias coils. Note that these high currents were never used during actual experiments, where we only apply 5 A to the main coils with the other coils switched off. The whole system heated up to about 50°C, while the usually used currents heated the system to at most 30°C. From this, we concluded, that additional cooling of the coils is not necessary. Nevertheless, we observed a shift of the MOT cloud position over the course of 30 minutes when switching on the current after the MOT coils had been off for longer. We confirmed that the coils have a circa 30 minutes thermalization time after switching them on. With this in mind, the coils are permanently supplied with a current and only switched off during the short probing intervals. This way, the whole setup is kept at thermal equilibrium (∼30°C) without any obvious shifts of the cloud of atoms using this method. Note that the coils are powered such, that the two main MOT coils are connected to one power supply each, thus they can be independently controlled, and we do not need additional compensation coil pairs for this direction. The bias and stretching coils are connected pairwise to one supply each. This way we can supply an offset field to move the centre of the field gradient, misplacing the atomic cloud, changing the overlap between the cloud and the fiber, effectively controlling the coupling strength.

MOT cooling light optics The nanofiber inside the glass cell is located at a height of about 30 cm above the optical table. A rigid two-story aluminium rig is set up around the cell to support the magnetic coil frame and breadboards hosting the MOT alignment optics, as shown in Fig. 5.7(a). The optical MOT setup extends over the whole breadboard construction, consisting of the optical table, where the beams are separated into horizontal and vertical beams, two breadboards on the same height as the glass cell, hosting the horizontal beam alignment optics, and one breadboard above the glass cell, for the vertical alignment optics. Furthermore, the breadboards next to the chamber host the main imaging setup, as introduced in the following section (5.2.3). As an example, the setup for beam distribution and expansion of the horizontal cooling beams is depicted in Fig. 5.7(b). Note that we took extra care to rigidly connect the breadboards to the optical table, being supported by an asymmetrically ordered set of posts, to prevent the possibility of high-pitched mechanical vibration excitation.

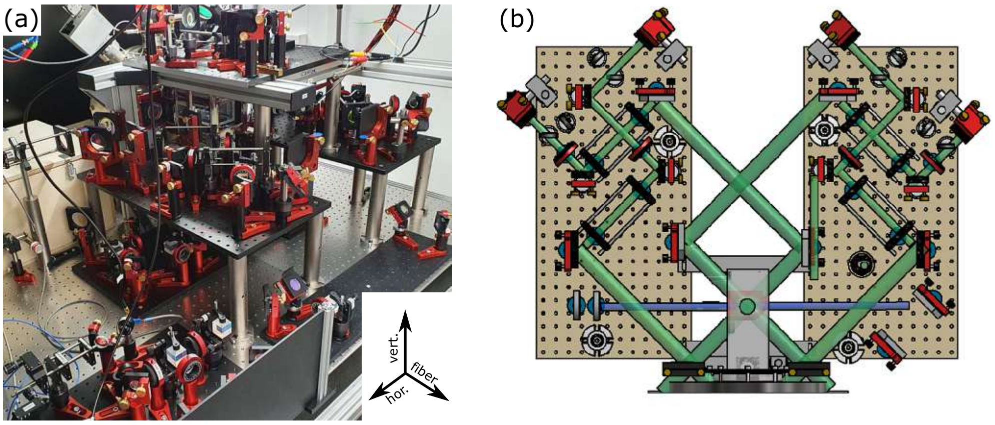

Fig. 5.7 (a) Picture of the experimental setup with MOT optics centred around the glass cell (visible in the centre). The Cooler and Repumper lights are injected in the bottom left, overlapped and then distributed across the breadboard construction. Note that the vacuum chamber in the back is hidden by the setup. (b) Sketch of the horizontal beam distribution on the breadboards next to the glass cell (shown centrally), with the cooling beams indicated in green. On each breadboard, we use two telescopes to expand the beams and a $\lambda/4$ waveplate to align the circular polarization. Afterwards a set of two mirrors is used to align the 2" beams. The absorption imaging is indicated in blue, where the beam comes from the right, passing the glass cell with the MOT cloud, being imaged by a pair of lenses to the left (camera not shown).

The cooling and repumping light fields for the MOT are overlapped using a beamsplitter. The combined fields are separated and guided towards the nanofiber to provide counter-propagating beams of equal power and opposite circular polarization, where in the vertical beam pair we supply twice the power compared to the horizontal beams. Thus, the elongated magnetic quadrupole field in combination with having the horizontal beam pairs cross at an obtuse angle leads to a cigar-shaped atomic ensemble, elongated along the nanofiber.

We set the circular polarizations of the MOT beams to be left-handed circular for the horizontal beams and right-handed circular for the vertical beams. The polarization is measured using a polarimeter and defined by looking towards the beam's origin. Before entering the glass cell, the beams are expanded to a diameter of 5 cm, where they are overlapped with the counter-propagating beam.

MOT optimization To optimize the cooling beam overlap, MOT position and loading, as well as the density of atoms around the nanofiber, we use fluorescence and absorption imaging for feedback introduced in the next section below. Once we obtain sufficient overlap between the atom cloud and the nanofiber waist, we additionally use optical density measurements (see 5.5) through the fiber to find the optimal cooling laser detuning and power, as well as magnetic offset fields. Finally, for further optimization, the position of the nanofiber can be changed using the fiber arm of the chamber in order to maximize the overlap between an optimized MOT and the waist of the nanofiber.

As it turned out, the size of the MOT does not directly influence the number of atoms that can be interfaced through the fiber and our approaches of increasing the number of interfaced atoms by increasing the density of atoms close to the nanofiber were not successful (e.g., dark spot MOT [113]). Alternatively, we stretch the MOT along the nanofiber waist using a magnetic quadruple field aligned along the fiber axis, ramping it up in the final 100 ms of MOT cooling. In this way, atoms in the outskirts of the cloud could be redistributed along the fiber waist, closer to its surface, and the whole MOT is stretched to overlap the waist of the nanofiber completely. Ultimately, this leads to optical densities above 50, where we observe MOT dimensions of about 1.2×0.5 mm.

The values obtained through optimization for operating our experimental apparatus are 4.99 A in the top and 5.02 A in the bottom coil, where we ramp the current of the stretching field to 6 A in the last 100 ms of the MOT loading sequence. The cooler laser is injected into the MOT setup with ~ 250 mW at a red detuning from the atomic transition of $\Delta_a \simeq 12$ MHz. The repumping laser requires no detuning and is injected into the MOT setup with ~ 20 mW.

5.2.3 Imaging and optical density

In order to characterize the MOT, we used absorption imaging, which allows us to determine the clouds size, position and optical density up to OD 6 as a function of time-of-flight after release from the MOT, in order to, e.g., determine the clouds temperature. For final optimization of the MOT and day-to-day calibration we measure optical density through the nanofiber for the fully overcoupled resonator.

Imaging optics

The design of the imaging system used in this thesis was first designed and implemented by me as part of my master thesis [106]. Here, I will only outline the design specifics and exemplary characterization of the atomic cloud. The design consists of two parts allowing for horizontal and vertical imaging. The main imaging is done horizontally, as shown in Fig. 5.7(b). We use fluorescence imaging for day-to-day monitoring of the cloud, while the more involved absorption imaging is only used during characterization and optimisation processes. The vertical imaging can only be used for absorption imaging, since its beam path is integrated into the vertical MOT beam setup, where it would be impossible to separate fluorescence photons from the MOT beam.

In both imaging designs we use a combination of 2-inch aspheric lenses placed such that the nanofiber is imaged onto a CCD chip. The setup allows for imaging scattered light from the nanofiber and fluorescence of the loaded MOT. Alternatively, we installed a telescope that sends collimated light resonant to the atomic transition along the optical axis of the imaging system, see Fig. 5.8.

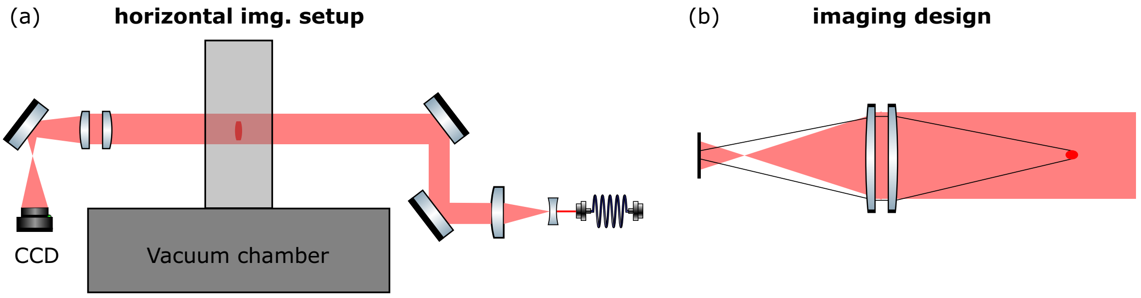

Fig. 5.8 (a) Sketch of the horizontal optical setup of imaging the MOT from the side, where resonant fiber-guided light is widened to about 5 cm before being sent through the chamber. (b) The imaging design allows both, directly imaging the fluorescence of the MOT, or its shadow when performing absorption imaging (black line). Note, due to spatial constraints, the imaging lenses have been put together as close as possible, still being able to collect light from the illumination beam to be imaged on a larger surface as the MOT-shadow to enable good contrast for absorption measurements (red).

The details of the used lenses and characteristic parameters of the imaging setup are summarized in table 5.1. We can measure the amount of light being absorbed by the MOT-atoms by taking three images, with (I_{atoms}) and without (I_{img}) atoms as well as without any light (I_{dark}). From this we can determine the local optical density according to

$$OD = \ln \frac{I_{\text{img}} - I_{\text{dark}}}{I_{\text{atoms}} - I_{\text{dark}}}. \tag{5.6}$$

Here we assume excitation intensities much lower than the atomic saturation intensity and absorption according to Beer's law

$$I = I_0 e^{-N\sigma z} = I_0 e^{-OD}, \tag{5.7}$$

where we define $Nz = n$ as the column density, which is the number of atoms in an infinitesimal (usually pixel size of imaging CCD chip) thin column of height z and $\sigma = \hbar\omega\Gamma/2I_{\text{sat}}$ is the absorption cross-section of a Cs atom. From this quantity we can infer the number of atoms in the MOT, by integrating column densities over the clouds cross-section. The number of atoms is given by

$$N = \int_{-\infty}^{+\infty} \int_{-\infty}^{+\infty} n(x,y)\mathrm{d}x\mathrm{d}y = \frac{A}{\sigma} \int_{-\infty}^{+\infty} \int_{-\infty}^{+\infty} OD(x,y)\mathrm{d}x\mathrm{d}y, \tag{5.8}$$

where A the imaged cross-section of a corresponding pixel in the CCD chip.

	horizontal	vertical
focal length l1 [mm]	300	125
focal length l2 [mm]	150	250
resolution [μm]	6.16	10.2
magnification	0.5	0.6
field of view [mm]	12.6×10.5	17.4× 14.5

Table 5.1 Summary of characteristics for the horizontal and vertical imaging setup.

Particularities of the absorption imaging While our absorption imaging system is a good tool to determine optical densities in the initial steps of MOT optimisation, it reaches its limits when the MOT cloud approaches OD ≈ 6.5. This limit is due to the 10-bit resolution of our imaging CCD chip, where the smallest measurable value is $I_0/1024$. Once the OD approaches this limit, the measurement becomes inaccurate. To measure larger OD's, it is required to release the cloud from the MOT such that it expands until the density lowers or install a different CCD chip. Note that for our experiment determining number of atoms and optical densities via absorption imaging was only of interest during the initial optimisation, until the MOT was visible interfacing the optical nanofiber. Afterwards all optimization was done directly by probing via the nanofiber. One huge advantage of absorption imaging over imaging just the fluorescence of the MOT is that the spatial distribution of atomic density in the MOT can be made visible, useful during optimisation of the MOT. As example see a comparison of cloud images during optimisation in Fig. 5.9.

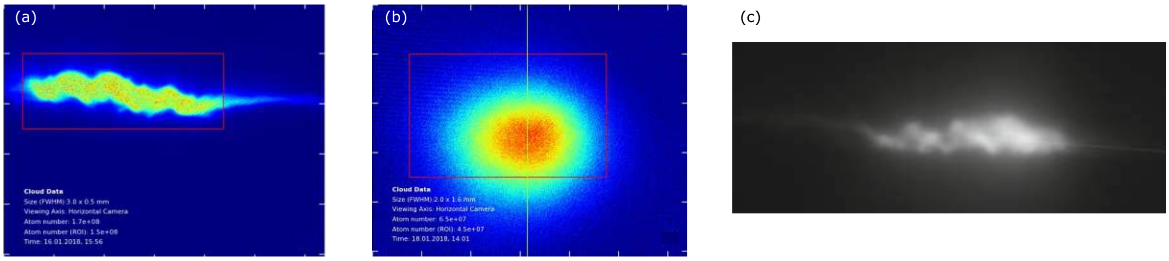

Fig. 5.9 Absorption images taken during first optimization of the MOT, for a trapped cloud of atoms (a) and after 30 ms TOF (b). On the right (c) we see a fluorescence image of a recent implementation of an optimized MOT the fiber, resulting in an OD of approximately 20.

TOF and temperature of the MOT

To measure the mean temperature of the atoms in the MOT cloud and confirm sub-Doppler cooling, we release the cloud from the trap and take a series of absorption images, varying the time between release and imaging. The cloud will fall due to gravitation while expanding like an ideal gas according to the ensemble's velocity distribution centred around the atoms mean quadratic velocity $\overline{v}^2$. The temperature of the cloud is defined via the mean kinetic energy of the atoms $\overline{E_{\text{kin}}} = \frac{m}{2}\overline{v}^2 = 3/2k_BT$, where k_B is the Boltzmann constant and m the mass of a Cs atom. The velocity distribution of atoms in the gas can be assumed to be Boltzmann velocity-distributed

$$f(v)\mathrm{d}v = \sqrt{\frac{m}{2\pi k_B T}} \exp\left(-\frac{mv^2}{2k_B T}\right) \mathrm{d}v\ . \tag{5.9}$$

If a gas of non-interacting particles with a given velocity distribution expands freely, its position distribution in one dimension is a Gaussian distribution too, given by

$$f(x,t)\mathrm{d}x = \frac{1}{\sqrt{2\pi\sigma(t)^2}} \exp\left(-\frac{x^2}{2\sigma(t)^2}\right) \mathrm{d}x, \tag{5.10}$$

thus, we can link the expansion of the cloud to its temperature via $\sigma(t) = \sqrt{k_B T/m}\, t$. In experimental realizations, the initial size of the atomic cloud is typically $\sigma(0) \neq 0$, where the width of the cloud evolves as

$$\sigma(t) = \sqrt{\sigma(0)^2 + \frac{k_B T}{m} t^2}. \tag{5.11}$$

When we now determine the width $\sigma(t)$ of the Gaussian position distribution for a cut through the atomic ensemble for different times after release from the MOT, we can determine the mean temperature of the atoms in the cloud.

After initial MOT set up, the temperature could be measured to be $113 \pm 4\mu$K, corresponding to $\bar{v} \approx 14.4$ cm/s and after optimisation of cooling beam alignment and polarization we measured $80 \pm 2\mu$K, where $\bar{v} = 12.7$ cm/s. Note that cooling further requires molasses cooling, which, however, would result in a decrease of the density of atoms in the cloud. Since the minimizing temperature is not critical for our experiment, we did not further investigate an optical molasses.

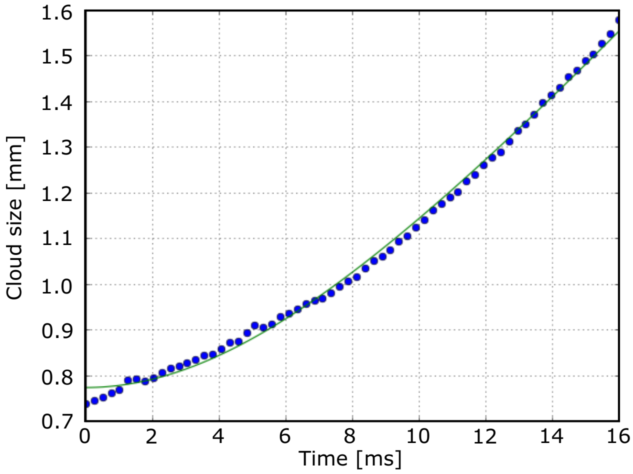

Fig. 5.10 Expansion of a falling atom cloud, measured using images taken over 16 ms with a temperature inferred to be $113 \pm 4\mu$K. The pressure was at 3.3e-9 mbar. Note that in the first millisecond the cloud had a non-Gaussian shape, leading to the kink in the curve.

5.3 Laser systems

This experiment consists in total of 4 different lasers, where in the following sections I will introduce the lasers tasks, its locking and means of optical control.

5.3.1 MOT lasers - Cooler and Repumper

For the generation of a magneto optical trap, two light fields are necessary: a very powerful cooling laser of a few hundred mW power (“Cooler”) and a laser (“Repumper”) that pumps atoms from a dark state back to take part in the cooling cycling transition. The Cooler laser is a diode laser using a tapered amplifier to generate a 2 W output, operating at 852 nm[9]. It is locked using a Pound-Drever-Hall (PDH) method [99]. As reference, we use the crossover between the Cs $6^2S_{1/2}\,F=4 \rightarrow 6^2P_{3/2}\,F'=3$ and $F'=5$ transition revealed in a Doppler-free spectroscopy. This transition is 226.12 MHz red-detuned from the resonant $F=4 \rightarrow F'=5$ probing transition, where we use an AOM in double-pass configuration to shift the probing light frequency into resonance. We use a commercially available compact spectroscopy device[10], measuring the transmission spectrum of Cesium via a built-in vapour cell. From this spectrum the laser’s controlling unit can directly process an error signal and appropriate feedback allowing for completely integrated on-board locking. Note that for the PDH-lock fast modulation of the laser current is performed to generate frequency sidebands. Thus, this laser is not suitable for interfacing the resonator with its narrow resonance lines, where the unlocked laser linewidth, specified by the manufacturer to be ~ 300 kHz, is already on the order of the resonator’s resonances (~ 1.1 MHz for resonator 1 in Vienna, ~ 460 kHz for resonator 2 in Berlin). The locked Cooler light can be scanned and attenuated using an AOM in double-pass cat-eye configuration and is injected into a polarization maintaining (PM) fiber and guided towards the MOT setup, described above.

For the Repumper, we use a self-built extended cavity diode laser (ECDL) [94, 114] that is locked to the $6^2S_{1/2}\,F=3 \rightarrow 6^2P_{3/2}\,F'=3$ and $F'=4$ crossover. Here, for locking via Doppler-free spectroscopy, we use self-built electronics generating an error signal using the PDH method by modulating the lasers current. From the obtained error signal an analogue PID loop generates a feedback controlling the laser’s external grating. Due to the limited optical power of this laser, we only use a single pass AOM, shifting the locked laser light ≈ 100 MHz to be resonant with the repumping frequency. Furthermore, the AOM allows for controlling the power injected into a PM fiber that is guiding the light towards the MOT setup.

5.3.2 Lasers for interfacing the resonator - Probe, Lock and Heating

To interface the resonator, we need in total 3 light fields: 2 independently controlled resonant light fields for probing and locking the resonator, taken from a locked narrow diode laser and a far blue detuned heating light at 780 nm, taken from a self-built external cavity laser

---

[9] Toptica - TA pro

[10] TEM Messtechnik - Cosy

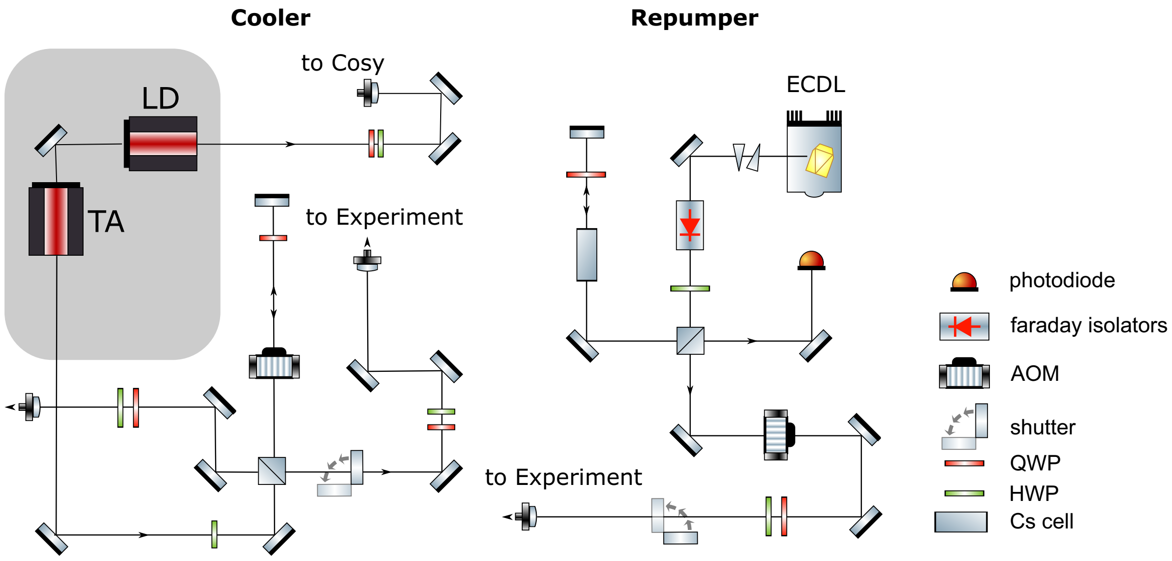

Fig. 5.11 Sketch of the Cooler (left) and Repumper (right) setup.

(ECDL) to keep the nanofiber surface hot, intended to reduce Cs adsorption. The injection and detection setup for light interfacing the resonator has been already introduced in chapter 4. Here we focus on the origin and initial control of light, as shown in Fig. 5.12.

Our narrow-linewidth probing laser[11] is locked using the Pound-Drever-Hall method also locked to the crossover of the Cs $F = 4 \rightarrow F' = 3$ and $F = 4 \rightarrow F' = 5$ transition via Doppler-free spectroscopy, where an AOM in double-pass configuration shifts the light into resonance. In order to generate the error signal, we externally modulate the light before entering the spectroscopy using a phase EOM in a separate spectroscopy arm. This way, we avoid frequency modulation of the optical probe light which otherwise would increase the frequency width of the laser. To further narrow the laser's bandwidth and improve the lock stability, we feed the error signal into a two-step fast analogue lock module[12], supplying fast feedback to the laser's current and a slower feedback to the grating, preventing long term drifts. According to the manufacturer, using the narrow linewidth option laser and the fast feedback setup introduced here, we can reduce the short-term linewidth of the laser from 100 kHz (specified for the ECDL) to 50 kHz. The laser output is then split into two separate setups manipulating the fields, referred to as the Probe and the Lock.

The Probe is injected into a fiber-guided intensity modulator based on a Mach-Zehnder interferometer with integrated EOM that is used for generating fast (0.25 - 25 ns) optical pulses before being fed into a setup consisting of a double-pass cat-eye AOM for frequency and amplitude adjustment. Before the light is injected into the resonator interfacing setup (see 4.4), a photodiode is used to measure the transmission through the EOM-switch. This is necessary to calibrate the so-called bias voltage of this switch, that is setting the switch into a state of zero light transmission and is drifting over time.

---

[11] Toptica - DL pro, narrow bandwidth option

[12] Toptica - Falc 100

In the Lock setup, a part of the light is separated for absorption imaging of the MOT, amounting to $\approx 3.2\,\mathrm{mW}$, that for the beam size of $\sim 5\,\mathrm{cm}$ diameter in the imaging setup corresponds to 10% of saturation intensity of the probing transition. Most of the lock light is used for locking the resonator, where two AOMs, each in a double pass configuration, are used for controlling the light. Note that the first AOM is solely for switching, while the second allows for frequency scanning and attenuating the light. This way, having two AOMs, we can suppress the background of lock light sufficiently from $35\,\mu\mathrm{W}$ when both AOMs are on to 3600 ct/s (both off) measured using the SPCMs ($\approx 10^{-15}\,\mathrm{W}$) during probing the resonator. Note that a shutter would perform better but does not switch as fast as required. The lock light is injected into a PM-fiber and guided towards the resonator injection setup (see chapter 4).

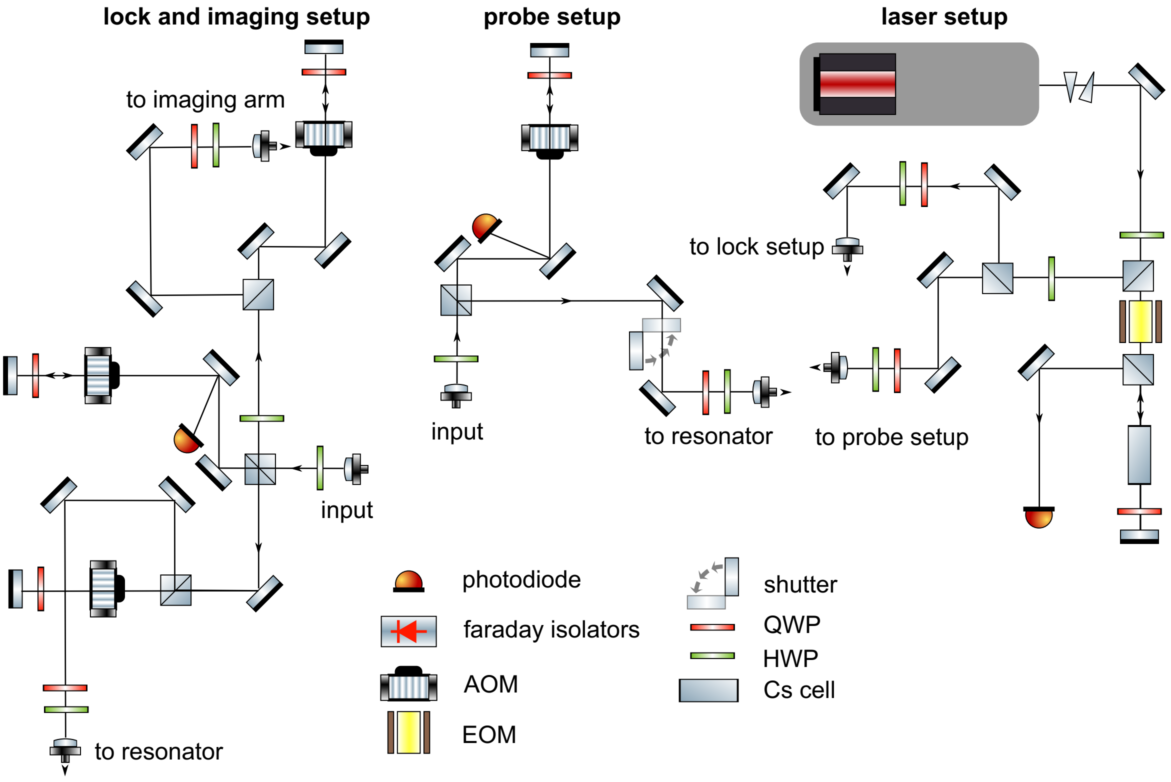
lock and imaging setup
probe setup
laser setup
to imaging arm
to lock setup
input
to resonator
to probe setup
input
to resonator
photodiode
faraday isolators
AOM
EOM
shutter
QWP
HWP
Cs cell

Fig. 5.12 Probe laser and setup for probe, lock, and resonant imaging light

5.4 Experimental control environment

The experimental control and data acquisition is centred around an experimental control system called AdWin[13], a standalone real-time computation unit that provides controlling and processing a variety of fast modules allowing for synchronized analogue in- and output as

---

[13] Jäger Computergesteuerte Messtechnik GmbH - AdWin Pro II, Pro-CPU-T12, 1GHz + variety of I/O modules

Die approbierte gedruckte Originalversion dieser Dissertation ist an der TU Wien Bibliothek verfügbar.
The approved original version of this doctoral thesis is available in print at TU Wien Bibliothek.
TU Bibliothek Your knowledge hub WIEN

well as digital output. The analogue outputs control, e.g., our AOM drivers and magnetic field current drivers, allowing to ramp field amplitudes and laser frequencies. The digital outputs are used to trigger shutters, SPCMs and our timetagging FPGA that records timestamps of photon detection events at the SPCMs. Furthermore, AdWin's clock is used to synchronise all data acquisition software, such as imaging, locking routines and EOM calibrations by sharing its status with the local lab-network using Ethernet. To save memory and computational time, the time resolution of our sequences is typically set to 1 μs - 5 μs, depending on the experimental demand, but the 1GHz CPU allows in principle for higher timing resolution.

To establish a versatile and easy to use software-platform controlling the experiment, for the previous realization of this experimental setup [104, 105], a graphical user-interface (GUI) based on python has been programmed to make the use of AdWin more intuitive. The programme operates in two main settings. The first, so called “calibration mode” runs AdWin in a cw-operation, where all output ports are assigned to a static value set in the GUI. This is ideal for maintaining or setting up the experiment allowing to quickly switch experimental parameters having one central panel to control the state of the whole experiment.

The second, “sequence mode” allows for writing a python script containing a succession of values assigned to AdWins output boards. I would like to point out, that the current implementation of our user interface compiles such a sequence once and forwards it to AdWin's CPU, where it will be executed independently. This means, that the control PC is not blocked during the sequence, but AdWin will not respond to any changes during performing the experimental run, making any real-time on-board feedback impossible. Part of my work on the experimental control environment included adding functionality to the base-coding of our user-interface and AdWin's routines, to implement reacting to input voltages during an experimental run. This way we can successfully implement fast feedback loops inside the experimental control, allowing for more versatile and complex sequences. As an example, real time calibration of the fiber-integrated EOM generating pulses of probe light is now possible without interrupting an experimental run, leading to substantial speed up and automation.

The data acquisition is mainly done by an FPGA[14], collecting and processing data streams of our SPCMs that detect the photons transmitted or reflected from the cavity. Control and pre-analysis of acquired data is done in homebuilt control software accessing data via suitable APIs, allowing for immediate interpretation of the state of the experiment.

Additionally, to monitor the experiments environment, such as laboratory temperature, humidity, chamber pressure or power of light picked up on monitoring photo diodes in the setup, we installed a standalone mini-PC hosting a 32-port National Instruments card providing permanent data acquisition and display.

---

[14] Swabian Instruments - TimeTagger 20

5.5 Coupling atoms to the nanofiber

5.5.1 Optical density trough the nanofiber

One of the most essential parameters on which the outcome of our experiments depends on is the optical density (OD) of the atomic ensemble for the transmitted probe light trough the nanofiber. With this number we can determine the coupling strength $g_N = \sqrt{N}g$ of our atoms to the resonator using

$$g_N^2 = \frac{OD}{2}\gamma\nu_{\mathrm{FSR}}. \tag{5.12}$$

To determine the OD, we record the frequency-dependent transmission of nanofiber guided light by scanning the probe laser across atomic resonance ω_0 and fit the theoretically expected transmission calculated from Beer-Lambert law to the recorded data (see also 2.4.1)

$$\begin{aligned} T(\omega) &= \exp\left(-\mathrm{OD} f(\omega)\right) \\ f(\omega) &= \frac{(\Gamma/2)^2}{(\omega-\omega_0)^2+(\Gamma/2)^2}. \end{aligned} \tag{5.13}$$

Comparing the inferred coupling strengths from OD measurements to coupling strengths inferred from coupled resonator spectra shows this method works sufficiently well for not too-high OD.

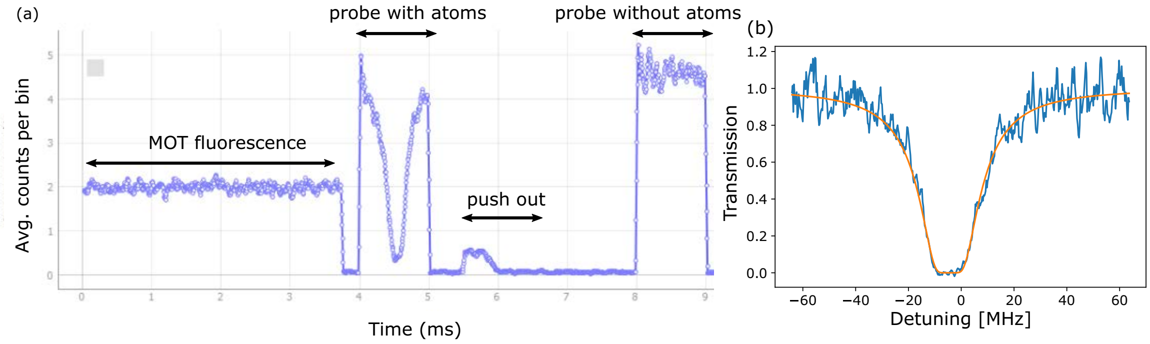

Fig. 5.13 (a) Example of the accumulated real-time histogram of detected photons provided by the timetagger software. First, we see fluorescence photons picked up during loading the MOT. After the MOT lasers have been switched off, we wait for the fluorescence to vanish before scanning the probe laser across atomic resonance twice, once with and once without atoms. In between the probing pulses one can see the fluorescence emitted from atoms during the push-out, initiated by external resonant imaging light. (b) Example of a measured transmission through the fully-overcoupled resonator (blue). The orange curve is a fit using Eq. (5.13) yielding an OD $= 21 \pm 0.3$.

To measure the single-pass transmission, the resonator has to be fully overcoupled turning the setup efficiently into a long waveguide containing an optical nanofiber. After loading the MOT, we use the probe laser to send two frequency sweeps of 1 ms length. Between these so-called probe and reference pulses, we use a burst of strong resonant imaging light from the side to push away the atoms from the fiber. Note that between releasing and probing the MOT, we wait for 0.2 ms such that fluorescent light from the MOT will not be picked up by the photon detectors. An example of collected photons on the SPCM during this sequence is shown in Fig. 5.13(a). For data analysis, the signal is background reduced and we divide the probe count rate by the reference count rate and the resulting transmission spectrum is fit with ω_0 and OD as free parameters. An example of an OD measurement is shown in Fig. 5.13(b).

Deviations between theory and data occur for higher OD when we start recording asymmetric transmission spectra. We believe this is due to the MOT being switched off before probing, such that the atomic cloud falls while probing, effectively changing the number of atoms being interfaced during a frequency sweep. Furthermore, we run into technical problems for measuring ODs above 50, as the limited frequency range accessible with the AOM does not allow to fully resolve the wings of the transmission dip all the way to 100% transmission. This leads to large errors in the OD estimation and we rely mostly on fitting loaded resonator spectra determining coupling strengths, which provides a much cleaner signal.

5.5.2 Atom number calibration

The most relevant quantity that influences the coupling strength g_N, is the factor $\beta N = \mathrm{OD}/4$. Note that in our setup we cannot control β as it strongly depends on the distance of atoms from the nanofiber surface and the atoms are not trapped in our experiment. To get an estimate of the average single atom coupling strength $g_1 = 2\beta\gamma\nu_{\mathrm{FSR}}$, we have to either measure the effective channelling efficiency of spontaneous emission into guided modes β or the number of atoms N responsible for the measured spectra.

For acquisition of β, we attempted to measure the transmission of probe light over time while pumping the atomic ensemble into a dark state, as shown in [115] and described below. This approach turned out to be not applicable for our setup, where there is a constant input flux of ground-state atoms from the surrounding cloud of atoms perturbing the pumping dynamics. Eventually, we moved on to measure the second-order correlation function $g^{(2)}(\tau)$ of photons emitted into the resonator. Here, the photon statistics of the light gathered from an excited ensemble of atoms strongly depends on the contributing number of atoms [116, 117], which allows one to get an estimate of N from the temporal shape of $g^{(2)}(\tau)$. In the following, I will present our findings for the two methods used for measuring β and N. Firstly, pumping the atomic ensemble trough the nanofiber into a dark state and secondly, exciting the atoms via resonant probe light with an external beam from the side and analysing $g^{(2)}(\tau)$ of the photons scattered into the resonator.

5.5.3 Pumping the ensemble through the fiber

First approach At first we attempted to determine the channelling efficiency β based on recording the atom number dependent transmission through the nanofiber over time, exciting the $F = 4 \rightarrow F' = 4$ transition, proposed by [115]. Excited atoms can either decay to the

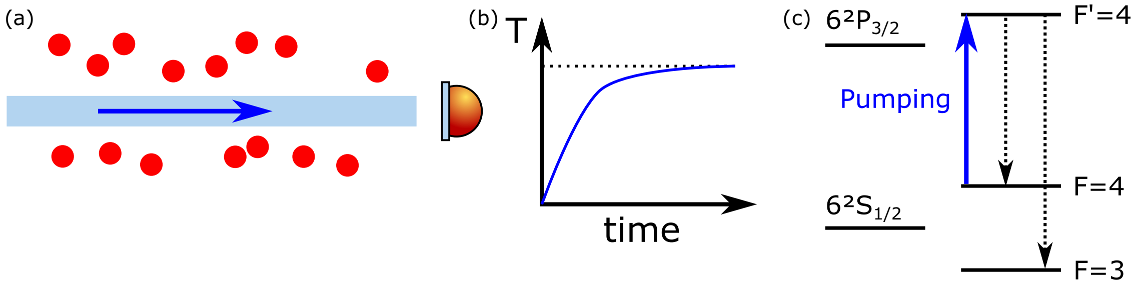

Fig. 5.14 (a) The ensemble of randomly distributed atoms around the nanofiber is excited with fiber guided light on the $F = 4 \rightarrow F' = 4$ transition, where we record the time-evolution of the transmission signal (b) on an SPCM. (c) Level scheme of Cesium, where atoms excited to the $F' = 4$ can spontaneously decay into the $F = 3$ ground state after which they are transparent for the probing light.

$F = 3$ or $F = 4$ ground state, with a fixed branching ratio, as depicted in Fig. 5.14(c). Cesium atoms in the $F = 3$ ground state are 9.192 GHz detuned from the probing transition, hence do not absorb any photons from the probing light. Thus, when probing continuously, the number of atoms partaking in this pumping circle will decrease over time, where the time-evolution of the transmission signal, will increase (see Fig. 5.14(b)) and is given by

$$T\left(N,\beta,t\right) = \frac{1}{1 + \left[\exp\left(4\beta N\right) - 1\right]\exp\left(-\beta\Phi_{\mathrm{in}}t/k\right)}. \tag{5.14}$$

Here, Φ_{in} is the input photon flux and k is the wavenumber of the probe light. Experimentally, after measuring the optical density of an ensemble, we record the transmission while sending a pulse of 12 μs length through the ensemble, for up to 4 different input photon fluxes, shown in Fig. 5.15.

We immediately observed that depending on the probe power, the transmission saturated at different levels, but never reached $T = 1$ as would be expected from Eq. (5.14) for $t \rightarrow \infty$. As it turned out, while this method was introduced to calibrate atom numbers for ensembles of trapped atoms with small deviations of β, this approach is not suitable for our experimental realization, since we experience a permanent flux of atoms in the $F = 4$ ground state entering the interaction volume during our attempt to pump the ensemble.

Second approach To reduce this effect of the atoms entering and leaving the effective interaction region around the nanofiber, we tried to pump all atoms into the dark state faster than the expected transit time of atoms passing the optical nanofiber, which is on the order of 1 μs (0.9 μs could be inferred from the following coincidence measurements). However, this proved to be technically problematic since the switch-on time of the probing AOM is much slower than the time-evolution of the transmission signal for the required input flux. Due to these problems we decided to use a different approach which is described in the following section.

Die approbierte gedruckte Originalversion dieser Dissertation ist an der TU Wien Bibliothek verfügbar.
The approved original version of this doctoral thesis is available in print at TU Wien Bibliothek.
TU Bibliothek WIEN Your knowledge hub

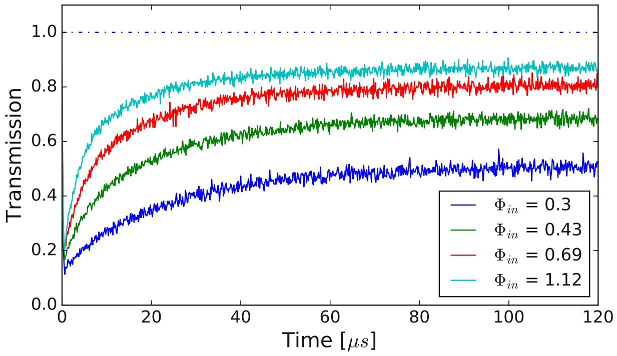

Fig. 5.15 Measured transmission as a function of time for 4 different photon fluxes $\phi_{in} = [0.3, 0.43, 0.69, 1.12] \times 10^9$ photons/s. As can be clearly seen, the transmission saturates below 1.0 and the saturation level strongly depends on the input photon flux.

5.5.4 Correlation measurements

Correlation measurements are a useful tool to experimentally determine the photon statistics and coherence properties of light emitted by a system, see for examples [118–120]. For our purpose to accurately determine the number of coupled atoms, we use a method introduced by [116, 117], that analyses the second-order correlation function of fluorescence photons emitted into the nanofiber. Together with the known OD of the coupled ensemble, this method allows us to infer both, the contributing number of atoms N and the channelling efficiency β. As this measurement operates in cw-mode, it yields much better results than the measurement described in the previous section.

The normalized second-order correlation using the photon creation (annihilation) operator $\hat{a}^\dagger$ ($\hat{a}$) can be interpreted as the probability to detect two photons with time delay τ at two detectors [121, 122] and is defined by

$$g^{(2)}(\tau) = \frac{\langle \hat{a}^\dagger(t)\hat{a}^\dagger(t+\tau)\hat{a}(t+\tau)\hat{a}(t)\rangle}{\langle \hat{a}^\dagger(t)\hat{a}(t)\rangle\langle \hat{a}^\dagger(t+\tau)\hat{a}(t+\tau)\rangle}. \tag{5.15}$$

For our purpose, we are interested in measuring correlations of fluorescence photons scattered from the excited atomic ensemble into the nanofiber, as depicted in Fig. 5.16.

Note that for this experimental scenario, where the fluorescence of emitters is collected via a nanofiber, we expect to observe in the measured ensemble $g^{(2)}(\tau)$ correlation an interplay between the single-atom first- and second-order correlation functions $g_1^{(1)}(\tau)$ and $g_1^{(2)}(\tau)$ of the contributing atoms. This is different for other experimental implementations, where the fluorescence photons from a few emitters are collected for larger solid angles [123, 124]. Here, the first order-coherence is usually washed out due to averaging photon counts that have been emitted into many different spatial modes. Thus, the measured $g^2(\tau)$ reveals only information on the second-order coherence. The analytic expression of the second-order

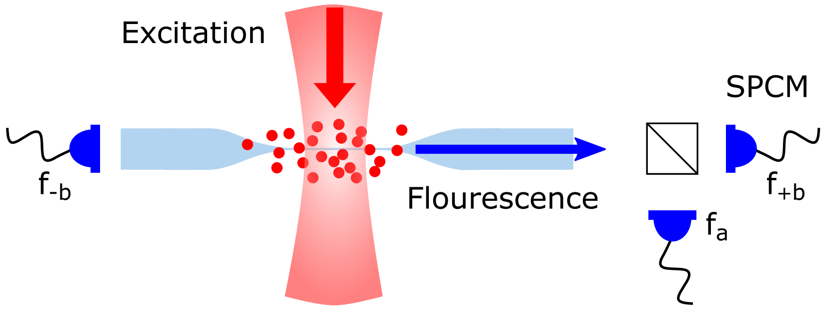

Fig. 5.16 Schematic of the correlation measurement setup, where the MOT beams resonantly excite the ensemble of atoms. Fluorescence photons emitted into the nanofiber are being detected in a Hanbury Brown-Twiss type detection at the output of the resonator.

correlation for our scenario, depending on $g_1^{(1)}(\tau)$ and $g_1^{(2)}(\tau)$ is given by (see [125])

$$g^{(2)}(\tau) \propto N g_1^{(2)}(\tau) + N(N-1)\left[\mu_0 + \mu \left|g_1^{(1)}(\tau)\right|^2 \delta_{f_a,f_{+b}} + \mu' \left|g_1^{(1)}(\tau)\right|^2 \delta_{f_a,f_{-b}}\right], \qquad (5.16)$$

where $\delta_{f_a,f_{\pm b}}$ denote the observation direction. In this expression, μ_0, μ and μ' are geometrical factors that depend on the mode profile function of the nanofiber guided light the fluorescence photons couple to, the position of emitters around the fiber and the orientation of their dipole-moments. Analytical values for μ_0 and μ are hard to determine for our experimental situation but were determined through simulation in [117] by assuming a Poisson atom distribution in the MOT and averaging over random positions of atoms around the fiber.

As one can see in Eq. (5.16), the single-atom second-order correlation function $g_1^{(2)}(\tau)$ governs the behaviour of $g^{(2)}(\tau)$ for small atom numbers ($N \lesssim 2$), where it describes the contribution of single atoms coupling to the nanofiber. Here, one observes a minimum delay of $1/\gamma$ for a free-space atom before emitting a second photon, a behaviour that is leading to antibunching, shown in Fig. 5.17. The first-order correlation $g_1^{(1)}(\tau)$ becomes more dominant for larger ensembles, where it describes the contributions from atom pairs, hence scaling with N^2. In this regime $g^2(\tau)$ experiences bunching and two-photon interference, that facilitates stimulated emission of the light into the fiber, becomes substantial. However, once $N \approx 20$, the expected bunching (and width of bunching) becomes very insensitive to the atom number. In between those two extremes, a transition from antibunching to bunching occurs in $g^2(\tau)$, that is very sensitive to the number of atoms. This is the region we want to operate in, making it ideal for us to determine the number of coupled atoms accurately. Note that for atom number correlation we are not interested in the term proportional to $\delta_{f_a,f_{-b}}$, correlating atoms being scattered in opposite directions into the nanofiber, since this contribution always shows antibunching that is very insensitive to the number of atoms [125].

Measuring $g^{(2)}(\tau)$ for different atom numbers and fitting Eq. (5.16) to the normalized data yields N independent from β. Additionally, once the number of atoms for an experimental realization is known, β can be calculated from the optical density, where we assume that the average β does not depend on the ensemble's size and hence the number of coupled atoms.

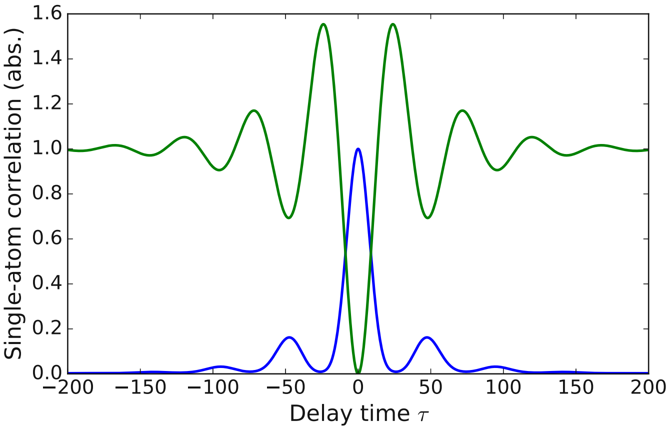

Fig. 5.17 Plots of the single-atom correlation functions versus delay time τ, where we assumed a Rabi frequency of $\Omega = 4\Gamma$, for the spontaneous decay rate Γ of Cesium. The green line corresponds to $g_1^{(2)}(\tau)$ showing antibunching at $\tau = 0$ and the blue line shows $|g_1^{(1)}(\tau)|^2$ featuring a clear bunching at $\tau = 0$.

Experimental realization

Experimentally we measure $G^{(2)}(\tau)$, the non-normalized second-order correlation from which we obtain the normalized second-order correlation $g^{(2)}(\tau)$ during data analysis (see below). For the measurement, we stroboscopically change between trapping and exciting the atomic cloud, allowing for high repetition rates of the experiment. In the experimental sequence we apply an initial phase of magneto-optical trapping for 2 seconds, long enough to provide a MOT that is not getting bigger if we trap longer. Afterwards, the sequence switches back and forth between a 20 μs long fluorescence phase and a 200 μs recapturing phase to prepare the atom cloud for the next run. For the excitation, we switch the MOT beams into resonance with the atomic transition, where the intensity of the MOT beams exceeds the saturation intensity of probed transition $I \approx 1.1 I_{\text{sat}}$ (for σ-polarized light [126], assuming uniform illumination). This way we can collect a sufficient number of fluorescence photons in short times. Note that before and after each experimental run (typically 200 000 individual measurements) for a realized number of coupled atoms, we also have to separately measure the optical density of the probed atomic ensemble to obtain β and check that the optical density has not changed over the course of the measurement.

For detection, the photons emitted into the nanofiber are collected at the output of the resonator, where they are forwarded to a Hanbury Brown-Twiss type detection setup consisting of a 50:50 beamsplitter and two SPCMs [118], as depicted in Fig. 5.16. In order to not perturb the measured correlation function, it is important to prevent “technical” photons created by the electron avalanche inside the SPCM, to emit back into the detection setup, where they could add to an accidental detection event. This can be done using narrow 850 nm bandpass filters in front of each SPCM, filtering out most of this broad flash. Finally, data acquisition is done by assigning timetags to the individual clicks of the SPCMs by our timetagger.

Data analysis

We obtain a non-normalized second-order correlation function $G^{(2)}(\tau)$, by evaluating the time difference of each detected timetag of one SPCM to every timetag of the other SPCM and histogram the outcome in 2 ns bins. This bin size is the smallest before significant aliasing effects occur due to the timetagging FPGA. In a next step we normalize, and background correct our coincidence measurements.

Firstly, we divide the obtained data by the triangular slope arising due to the limited measurement time of $20\,\mu$s. To this end we fit a linear slope to our data for time differences larger than $2\,\mu$s, indicated in Fig. 5.18(a). This can be safely done, since all these measurements were performed for a fully overcoupled resonator, hence we do not expect any signatures at multiples of the roundtrip time. In the obtained correlation function (Fig. 5.18(b)) we still see bunching with an exponential decay on the order of $\tau \approx 1\,\mu$s. We attribute this to a classical bunching that arises from intensity fluctuations of the fluorescence photons caused by having non-stationary emitters that transit the mode of our nanofiber. The width of this bunching contribution depends only on the temperature of the atomic ensemble as described in [116]. We are only interested in signals around $\tau \approx 100$ ns, on the order of a few lifetimes of the excited transition, thus we subtract this bunching from our signal, where we could fit an exponential decay with a decay time $\tau = 0.9\,\mu$s to this bunching signal, as seen in Fig. 5.18(b).

Independently from these contributions, we observe a substantial photon background in our measurements. This can be explained by photons scattering from the MOT beams directly into the nanofiber and correlations caused by detector dark counts. These photons arrive at the detectors uncorrelated and lead to a reduction of contrast of the measured $g^{(2)}(\tau)$-function [127]. We correct for this effect, assuming a constant Poisson background flux B, where a correlation function including this background is given by

$$g_B^{(2)}(\tau) = 1 + \frac{1}{\left(1 + \frac{B}{\langle I \rangle}\right)^2} \left(g^{(2)}(\tau) - 1\right). \tag{5.17}$$

Here, $g^{(2)}(\tau)$ is the normalized background-corrected second-order correlation function we are interested in. Note that B was determined by measuring the countrate of photons arriving at the SPCMs when the MOT beams are on and no atoms are present (cw-countrate ~ 12 kHz per SPCM) and $\langle I \rangle$, the average intensity of the photon flux, can be determined by counting the photons arriving at the detector during the correlation measurement (cw-countrate ~ 23.5 kHz per SPCM).

In order to fit Eq. (5.16) to the normalized correlation function, we use the calculated single atom correlation functions from [125], given by

$$\begin{aligned} g_1^{(1)}(\tau) &\propto \frac{\Omega^2}{2\Omega^2+\gamma^2}\left[\frac{\gamma^2}{2\Omega^2+\gamma^2} + \frac{1}{2}e^{-\gamma\tau/2} + \frac{1}{2}e^{-3\gamma\tau/4}(P\cos\kappa\tau + Q\sin\kappa\tau)\right] \\ g_1^{(2)}(\tau) &\propto \frac{\Omega^4}{(2\Omega^2+\gamma^2)^2}\left[1 - e^{-3\gamma\tau/4}\left(\cos\kappa\tau + (3\gamma/4\kappa)\sin\kappa\tau\right)\right]. \end{aligned} \tag{5.18}$$

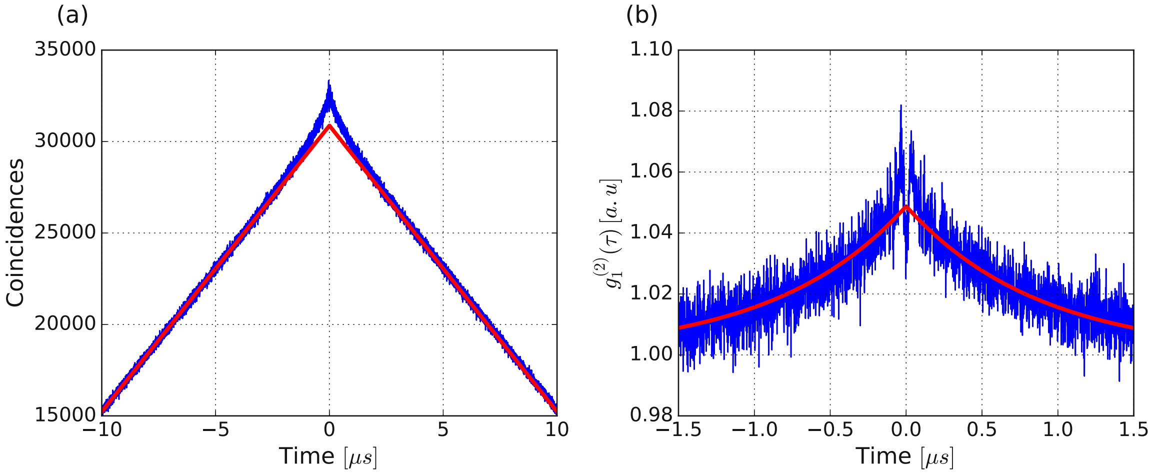

Fig. 5.18 Example of normalization procedure. (a) Triangular shape of coincidence measurements originating from a 20μs long pulse (zoom into ±10μs correlation shown). (b) Fit of transit time of atoms close to the nanofiber, with an inferred decay $\tau = 0.9\mu$s.

Here, $P = \left(2\Omega^2 - \gamma^2\right) / \left(2\Omega^2 + \gamma^2\right)$ and $Q = (\gamma/4\kappa)\left(10\Omega^2 - \gamma^2\right) / \left(2\Omega^2 + \gamma^2\right)$ with Ω being the Rabi frequency of the probing field at the position of the atoms. Furthermore, $\kappa = \sqrt{\Omega^2 - \gamma^2/16}$ is an effective frequency and γ is the overall spontaneous decay rate of the probed atomic transition.

Furthermore, for the fit we used restrictions for the geometric factors $\mu_0 = 0.33 - 0.37$ and $\mu = 0.17 - 0.35$, respectively [117] and left the Rabi frequency as a free fitting parameter. Note that the exact intensity at the position of the atom is different for every atom due to the complex intensity pattern of the MOT light around the nanofiber. Thus, in our fitting routine we only consider an average Rabi frequency that is approximately known. From our analysis, the uncertainty in fitting atom numbers is mostly governed by the uncertainty of the geometric factors μ_0 and μ. Nevertheless, since we used reasonable constraints on their values as discussed above, we found our fitted values for these numbers lead to an outcome that agrees well with the theoretical predictions.

Observations

Figure 5.19 shows the $g^{(2)}(\tau)$-functions obtained for optical densities varied from $\mathrm{OD} = 0.06$ to 0.20 and normalized as described above. Note that the OD was measured separately before the coincidence measurements for a single pass of probe light through the fully overcoupled resonator. From the measured, normalized coincidence measurement for $\mathrm{OD} = 0.06 \pm 0.01$, shown in Fig. 5.19(a) the fit yields an average atom number of $N_{\mathrm{avg}} = 2.7 \pm 0.3$. Here the single atom spontaneous decay is still visible in the overall shape of the signal and the measured data reveals slight antibunching for $\tau = 0$. For the highest OD in this set of data, shown in Fig. 5.19(c), the fit yields $N_{\mathrm{avg}} = 9.5 \pm 0.5$. We observe a clear bunching signal, as expected for increasing atom numbers. For intermediate OD, depicted in Fig. 5.19(b), we inferred $N_{\mathrm{avg}} = 4.3 \pm 0.3$. As seen in the figure, the data agrees well with the fit, but shows slight deviations for the highest OD dataset. Presumably, in this regime re-absorption of fiber-guided photons leads to perturbations in $g^{(2)}(\tau)$ not considered in the model. From the OD measurements, we determined the optical density per atom to be on average $\mathrm{OD}_1 = 0.022 \pm 0.005$, leading to a channelling efficiency $\beta = 0.0055 \pm 0.001$.

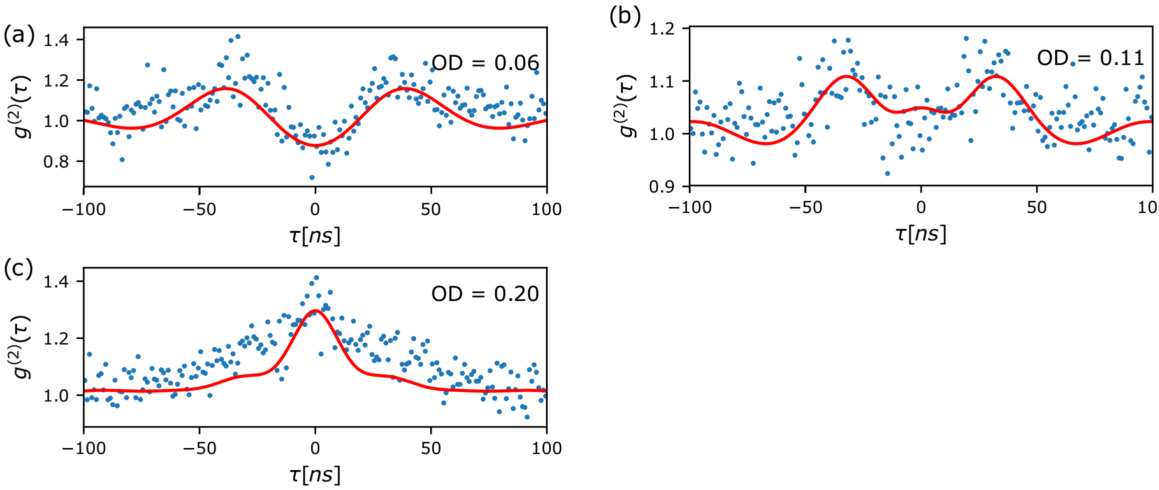

Fig. 5.19 Measured second-order correlation function and fit for different optical densities. The fit yields an average number of coupled atoms of 2.7, 4.3, and 9.5, respectively. (a) For small atom numbers $g^{(2)}(\tau)$ drops below 1 showing a signature of anti-bunched sub-Poissonian photon statistics. (b) For intermediate atom numbers, $g^{(2)}(\tau)$ still shows anti-bunching, but $g^{(2)}(0)$ remains above 1, thus corresponding to super-Poissonian photon statistics. (c) $g^{(2)}(\tau)$ exhibits bunching, with $g^{(2)}(0)$ clearly above 1, revealing super-Poissonian photon statistics as well.

5.5.5 Correlation measurements with the cavity switched on

In a next step, we were curious to obtain $g^{(2)}$-correlations of fluorescence photons emitted into the nanofiber for the case where the resonator is present. Figure 5.20(a) shows $g^{(2)}(\tau)$ for the case where the resonator is switched on and off for $\mathrm{OD} = 16.2 \pm 0.4$ and Fig. 5.20(b) shows the ratio of these two implementations. For both measurements at $\tau = 0$, we observe strong bunching, as expected from Eq. (5.16). At time delays corresponding to integer photon roundtrips through the resonator $\tau = 1/\nu_{\mathrm{FSR}}$, we observe bunching revivals. Supposedly, these bunching events stem from photon pairs emitted into the nanofiber [65], where one photon scatters out of the resonator at the beamsplitter, while the other photon continues inside the resonator and leaving the resonator after (at least) one roundtrip. A closer investigation with the updated resonator in Berlin is not yet on the agenda, since although having a higher finesse, we do not to expect anything else than more bunching peaks at delay times of higher multiples of the roundtrip time. Alternatively, to further investigate the temporal dynamics and photon statistics of the coupled atom–resonator system, we excite the ensemble with pulses much shorter than the Cs spontaneous decay time ≈ 30 ns, as described in chapter 6.3.

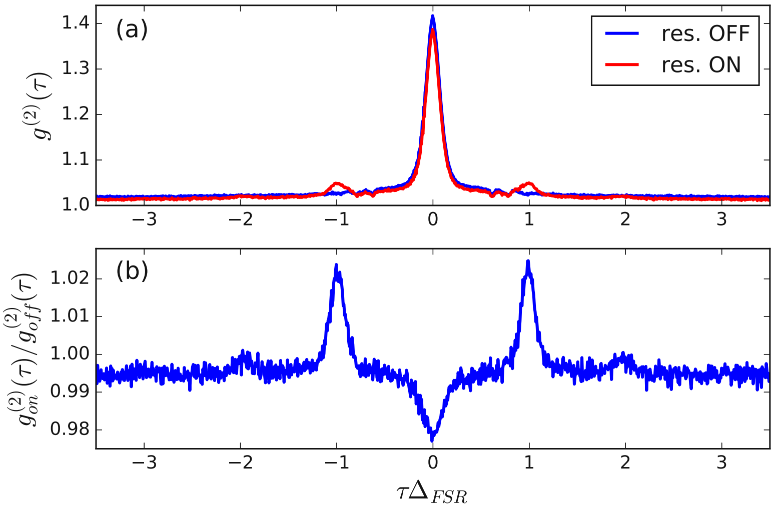

Fig. 5.20 (a) Measured $g^{(2)}(\tau)$ of fluorescence photons scattered into the resonator with the resonator being critically coupled (red) and fully overcoupled (blue). (b) Ratio of the two correlations functions from (a), which helps to reveal revivals of bunching after time delays corresponding to one and two roundtrips.

5.6 Possible experimental improvements

In this final section I would like to briefly discuss a few suggestions for possible improvements of the experimental setup that can be considered in a new generation of the experiment.

Fiber splicing and vacuum feedthroughs As already mentioned in the previous chapter, I would suggest looking into optimizing the splicing procedure for single-mode fibers operating at 850 nm and characterizing the loss when splicing different fiber types, since it seems as if splicing losses in our system are underestimated.

Going through the process of feeding fibers through the Teflon ferules a few times during my PhD and master work in this group, I found a few shortcomings of this approach. We could show, at least in one case, that tightening of the ferule does not harm the fiber transmission significantly, but it happened before that fibers broke during closing of the feedthrough. From my observations, a huge improvement to handling and minimizing the possibility to damage the fiber would come from using single-hole Teflon ferules. The fiber pigtails would be spatially separated, thus they cannot be twisted around each other during ferule tightening, which could be a cause for bending losses. An alternative suggestion would be flanges with optical feedthroughs with fiber connectors welded to a steel flange. However, although this method might improve fiber handling during nanofiber installation these feedthroughs also introduce at least 1dB loss for transmitted light[15].

---

[15] for example Vacom - SM850 feedthrough

Back flange A huge disadvantage of the current implementation of our setup is the heavy back flange. Although opening and closing is usually not done often, a smaller opening and easier to handle flange would be very beneficial. One idea is having the back flange similar to the front flange to be of 25 cm diameter with an, e.g., CF60 hole in the middle, where the mounted fiberarm would be connected to a smaller flange. The smaller opening would not only decrease the probability of dirt entering the chamber, also flooding with, and maintaining a nitrogen environment for the exchange of a fiber or Cs-dispensers would be possible.

MOT setup During 3 years of operation and several re-alignments of the MOT setup, I would suggest reducing the large free space setup of the MOT optics and decouple it into smaller setups via intermediate fiber coupling, where small misalignment does not carry on to larger misalignments further down the beam line. One suggestion would be to have a compact optical setup on a separate breadboard, similar to a commercially available fiber-cluster, where the self-built option allows for more versatility and means of monitoring and manipulating the light fields when necessary. Here, one can mix the cooling and repumping light and afterwards split it into six arms, that can be independently power controlled before injecting into fibers leading to the final MOT setup. The light could be directed at the chamber via fiber coupled beam expanders integrated into a suitable cage system, that already houses a $\lambda/4$ waveplate. Thus, the MOT setup would only consist of one telescope per beam, making alignment much easier and reducing the number of optics on the table. Additionally, at the moment we observe clipping of the large MOT beams on the last two 2-inch mirrors in each arm of the setup. Here, larger mirrors would be highly beneficial to further increase the overlap region of the MOT beams and thus the number of cooled and trapped atoms. It has been shown that the number of atoms trapped in a MOT increases with the diameter of trapping beams as d^6 [128], that would be beneficial to our MOT-stretching method and allow trapping of more atoms for lower Cs dispenser currents, therefore presumable lower Cs background.

Lock and heating For a better separation of lock and heating light from the measurement background, injection of those light fields in counter-propagating direction of the probing would be beneficial. This would in principle allow for uninterrupted locking of the resonator since the lock light would be significantly suppressed in the detection setup.

Die approbierte gedruckte Originalversion dieser Dissertation ist an der TU Wien Bibliothek verfügbar.
The approved original version of this doctoral thesis is available in print at TU Wien Bibliothek.
TU Bibliothek WIEN Your knowledge hub

Chapter 6

Observation of multimode strong coupling

In the previous chapters I discussed the limits of the conventional description of strong coupling in cavity QED and introduced conditions for which a different approach needs to be found to accurately describe coupled atom–resonator systems. Furthermore, I described in detail the experimental apparatus that allows us to reach coupling strengths exceeding the free spectral range of our resonator. In this chapter, I will present our experimental findings when investigating cQED in this new regime, where the Jaynes- and Tavis-Cummings model cannot be applied.

First, I will elaborate on experimental details regarding data acquisition sequences for these measurements. Secondly, we show the versatility of our experimental setup and theoretical framework by realizing a transition from a ring resonator to a long waveguide. Next, I will show transmission spectra of a short fiber ring resonator perfectly agreeing with the predictions of the Tavis-Cummings model. Finally, I show the inferred spectra of a long resonator operating in the multimode strong coupling regime, where I discuss whether our theoretical predictions hold up.

Afterwards, I will discuss our preliminary observations, where we probe our coupled ensemble through the nanofiber with optical pulses much shorter than the spontaneous decay time of Cesium atoms, being the base for further investigation of the dynamics of multimode strong coupling.

6.1 Experimental proceedings

6.1.1 Experimental sequence

To record a steady state spectrum of our resonator we need to alternate between two individual measurements, where we always start with measuring the single-pass optical density of the atomic ensemble coupled to the nanofiber. To this end, we fully overcouple the resonator, such that the light performs only a single roundtrip through the system. Afterwards, we measure the spectra of the atom–resonator system, for the situation of the resonator critically coupled with respect to the empty resonances, i.e., when scanning the resonator without coupled atoms, the transmission on-resonance reaches zero.

Adjusting the optical density in the measurement is done by changing the overlap between the MOT cloud and the nanofiber, realized by adding an offset current to one of the magnetic MOT coils. For the OD measurements we scan over several magnetic offset currents and accumulate data of typically 100 individual experimental realizations each, where we fit Beer-Lambert's law (Eq. 5.13) to the measured data. Once the set of ODs is evaluated, we proceed with transmission measurements of the coupled resonator for the same values of magnetic field offset, allowing to record a set of spectra for different coupling strengths. In a last step, we redo the OD measurements for comparison to the initial measurement to guarantee the long-term stability of the experiment and to confirm that during data acquisition the individual optical densities did not change.

This measurement routine was chosen over the alternation of overcoupling and critically coupling the resonator for each individual optical density for various reasons. First, we noticed a hysteresis on the setting of the variable beam splitter. By taking the whole set of transmission measurements in one go we can guarantee identical coupling parameters κ_{ext} for the whole set of data taken. Secondly, by performing the whole scan at once we speed up the measurement process significantly. Note that after each re-set of the beamsplitter a slight adjustments of the resonators eigenpolarizations and consecutive test of the lock would be required.

6.1.2 Probing the resonator

Our probing consists of two consecutive pulses sweeping light across atomic resonance, after the MOT trapping lights were switched off, as shown in Fig. 6.1. In the first pulse, we measure the interaction with atoms, the second pulse measures the empty resonator transmission for reference. Between the pulses we apply a strong resonant laser beam coming from the imaging setup to push away the atoms from the nanofiber, making sure the reference signal is not perturbed. The scanning of the probe light is performed with a double-pass AOM driven by a fast high-end RF-driver, capable of intensity stabilisation of the probe light during the sweep. For recording data, we use single photon counting modules (SPCM) and record the detection events using a fast FPGA timetagger (see chapter 5).

For a single experimental realization, we alternate between the preparation of the cold atom cloud, during which the resonator is actively locked and a probing phase as described above, intermittently interrupting the lock. The length of the probe pulses has been chosen to be 1 ms, such that we can fully resolve the cavities resonances. Much slower scanning leads to broadening of the measured signal, since there is a residual shift of the resonator's resonance frequency. For scanning much faster on the other hand we start seeing a cavity ring-up. Note, with the update to the narrow-linewidth laser, a pulse duration of 0.8 ms performed best. For this implementation, the residual movement of the intermittently unlocked resonator has been quantified to be less than the resonators linewidth, inferred by comparing the probe to the reference pulse.

TU Bibliothek, WIEN Your knowledge hub
Die approbierte gedruckte Originalversion dieser Dissertation ist an der TU Wien Bibliothek verfügbar.
The approved original version of this doctoral thesis is available in print at TU Wien Bibliothek.

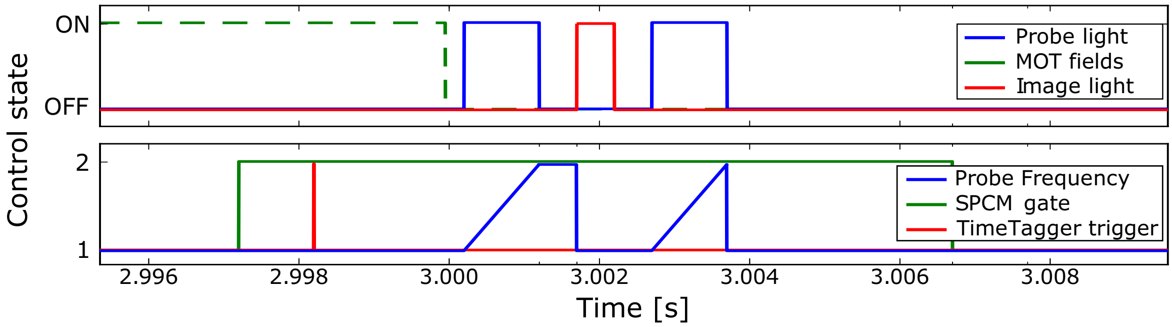

Fig. 6.1 Sequence used to interface the resonator after the MOT cooling light switches off (green dashed). During the time the SPCM is gated on (green) we switch on the probe twice, for interfacing the atoms and for reference, while the probe light frequency is scanned across atomic resonance. After the initial probing, a resonant imaging beam is used to push away atoms from the fiber.

6.1.3 Intensity calibration

In order to stay within the small excitation limit, it is necessary to attenuate the probe laser accordingly. To ensure that there is on average not more than 1 photon per roundtrip time in the resonator we estimated that for an empty, critically coupled resonator on resonance, the input flux needs to be smaller than ν_{FSR}. Additionally, for optimal measurements we aim for an SPCM photon detection rate on the order of 1 MHz, where it still operates in its linear response regime. Here, the average photon arrival time difference is much smaller than the SPCMs dead time. For this countrate, we inferred that less than 300 photon counts per second amount to the 780 nm heating light, with the dark countrate specified to be 26 Hz. Considering the variable beamsplitter's insertion loss, this 1 MHz countrate (for the Viennese resonator) results in approximately 0.5 pW inside the resonator, measured directly at the output of the resonator with a high sensitivity powermeter[1].

6.1.4 Data acquisition

For data acquisition, we connect the three SPCMs to a triggered time tagger FPGA, synchronized using ADwin. We employ a short pause between triggering the FPGA and the SPCM, to not record false clicks that occur when switching on the SPCM (see Fig. 6.1). The time tagger is equipped with an on-board micro-controller allowing for a real-time display of the acquired data and is additionally interfaced using a python routine. This way we can save lists of time tags of each detected photon, acquire pre-processed spectra of each individual experimental realization and monitor the experiment during data acquisition having the time tagger software pre-analyse and display the data in real-time.

---

[1] Ophir - Nova

6.2 Transmission measurements

6.2.1 Overcoupling the resonator - transition to waveguide physics

In order to highlight the versatility of our experimental setup, where we can realize any coupling scenario between light outside and inside the resonator, we show a transition from a undercoupled to a completely overcoupled resonator effectively transforming it into a long waveguide, a scenario discussed theoretically in 2.4.3.

Figure 6.2 shows the acquired spectra for an $\mathrm{OD} = 11.9 \pm 0.8$, where the external coupling parameter was changed via the setting of the variable beam splitter and inferred via fitting our transmission model to the acquired data. The spectra in Fig. 6.2 show the known strong coupling spectra when critically coupled (b) and shortly before the resonator fully transits into being fully overcoupled (c). Note that for the last two implementations in (a) the lock fails, as there is effectively no resonator present for which we could acquire an error signal, leading to a slight broadening of the measured data.

When measuring the single-pass optical density through the fully overcoupled resonator, we sometimes run into the problem of residue modulation of the resonator, exaggerated in Fig. 6.2(c). Note that with the given beamsplitter mechanics it is very hard to precisely fully overcouple the resonator and it requires careful alignment to minimize the residual resonances. To summarize, we can fit our model satisfactorily to the whole acquired transition, showing the versatility of our setup and theoretical approach.

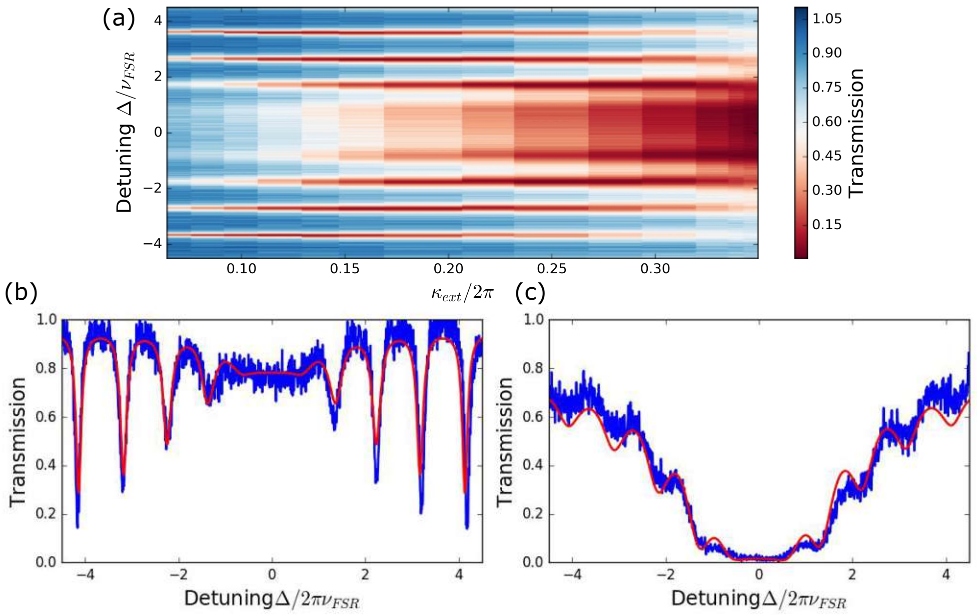

Fig. 6.2 (a) Coupling-fiber transmission for $\mathrm{OD} \approx 12$, scanning the coupling strength κ_{ext} between the interfacing waveguide and the cavity from critically coupling $\kappa_{\mathrm{ext}} = \kappa_0$ to fully overcoupling $\kappa_{\mathrm{ext}} = \nu_{\mathrm{FSR}}/2$. (b) Spectrum of the critically coupled resonator with fit theory, and (c) spectrum of the almost fully-overcoupled resonator resembling the transmission of an ensemble of atoms coupled to a waveguide.

6.2.2 Short ring resonator

Before moving to Berlin, we took the chance of disassembling the experiment to remove the fiber spool containing most of the ring resonator to realize a much shorter version of it. The ends of the variable fiber beamsplitter were directly spliced to the pigtails of the nanofiber, leading to an increase of the free spectral range to $\nu_{\mathrm{FSR}} = 36.75\,\mathrm{MHz}$, amounting to a 5.66 m long resonator and $\kappa_0/2\pi = 1.58\,\mathrm{MHz}$. The higher internal loss rate is due to the reduced length, where for the same finesse the internal loss rate scales as $\kappa_0 \propto 1/L$.

In Fig. 6.3(a) the acquired transmission spectra are plotted versus the coupling strength g_N. Due to the increased free spectral range, scanning the number of coupled atoms allowed to nicely show strong coupling, where $g_N > (\gamma_l, \kappa)$, indicated in Fig. 6.3(a) as lower horizontal line. The condition $g_N^2/\gamma_l \gg \nu_{\mathrm{FSR}}$ was also violated, putting us into the regime, where the Tavis-Cummings model cannot be used for correctly predicting the spectral features. The corresponding threshold is indicated by the upper horizontal line at $g_N/2\pi = 3.9\,\mathrm{MHz}$. For the experiment a maximum splitting of $g/2\pi = 0.3 \times \nu_{\mathrm{FSR}} = 11.25\,\mathrm{MHz}$ was measured, corresponding to an optical density of OD = 16.6, leading to a single-atom coupling strength of $g_1 = 2\pi \times 0.41\,\mathrm{MHz}$. With this, the intrinsic single-atom cooperativity is $C_{0,1} = 0.02$, where for the maximum coupling we achieved a collective cooperativity $C_N = 15.3$.

Nevertheless, although already operating in the regime $g_N^2/\gamma_l > \nu_{\mathrm{FSR}}$, the central splitting can be described theoretically using $g_N^2 = 2\beta\gamma\nu_{\mathrm{FSR}}$, indicated as black line in Fig. 6.3(a). Note that the Tavis-Cummings model will correctly model this splitting until $g_N \approx \nu_{\mathrm{FSR}}/2$ but fails to predict new resonances. When looking at the theoretical expectation using the cascaded interaction approach, expanded to even higher coupling strengths (compare Fig. 6.3(b)), one can see we were just short of observation of this new resonances, expected for $g_N/2\pi \approx 14\,\mathrm{MHz}$. In Fig. 6.3(c) we plot theoretical spectra for $g_N/2\pi = 11.25\,\mathrm{MHz}$, being the maximally realized coupling strength in our measurement (green), and $g_N/2\pi = 20\,\mathrm{MHz}$ (blue). Here, one can see that the expected onset of the new resonances features vanishing visibilities $V = T_{max} - T_{min}/T_{max} + T_{min}$, too small to be observed experimentally. Furthermore, the optical densities that could be achieved at that time were too little to allow for the observations of new resonances. Nevertheless, this measurement suggests that a resonator of intermediate optical length, would be ideal for investigating the emergence of new cavity resonances.

6.2.3 Multimode strong coupling

Soon after initial set up of the experimental apparatus, we managed to successfully measure the onset of multimode strong coupling, presented in detail in [53]. Summarized, in this implementation we showed splitting of the central mode for a maximum optical density of OD = 14.2, where we already observed the adjacent modes being pushed out significantly. With a measured $\nu_{\mathrm{FSR}} = 7.1\,\mathrm{MHz}$ we calculate the single-atom coupling strength to be $g_1 = 2\pi \times 0.18\,\mathrm{MHz}$ leading to an intrinsic cooperativity $C_{0,1} = 0.03$. This resonator was also used to determine the single-atom optical density being $\mathrm{OD}_1 = 0.022$, resulting in a channelling efficiency $\beta = 0.0055$, as discussed in detail in chapter 5.5.

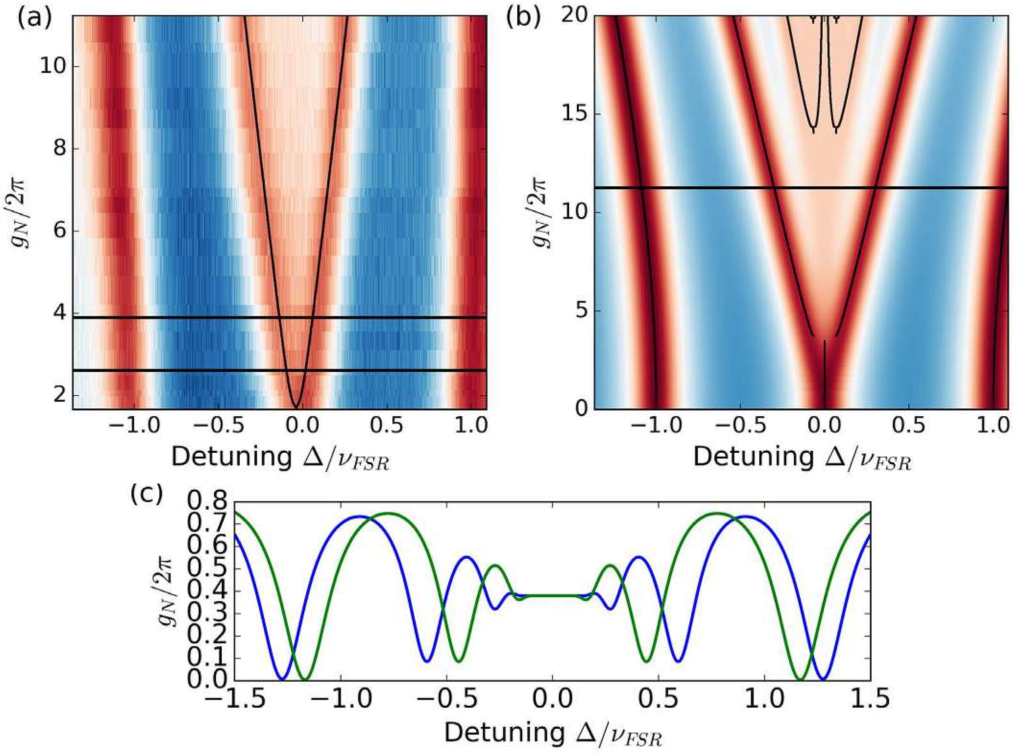

Fig. 6.3 Comparison of experiment (a) and theory (b) for the observation of strong coupling with a resonator of $\nu_{\mathrm{FSR}} = 36.75\,\mathrm{MHz}$ and a maximal splitting of $g_N/2\pi = 11.25\,\mathrm{MHz}$. The horizontal lines in (a) indicate $g_N = \gamma_l$ and $g_N^2/\gamma_l = \nu_{\mathrm{FSR}}$. In (a) the central splitting has been overlapped with the theoretical predictions of the Tavis-Cummings model, where in (b) we employed the cascaded interaction approach, exceeding the coupling strengths realized in (a). Cuts through the model are shown in (c) for the maximum splitting realized in (a) (green) and for the prediction for $g_N/2\pi = 20\,\mathrm{MHz}$ (blue). As one can see, for our realized OD in the experiment the new resonances do not yet emerge.

In a next step, we were curious to explore the regime, where $g_N > \nu_{\mathrm{FSR}}$, to see how well our theoretical predictions describe our observations. To experimentally realize this scenario for the implemented resonator (in Vienna) we calculated a single-pass optical density $\mathrm{OD} > 35$ is required. Once realized, the transmission through the coupling fiber for a loaded cavity was measured for a range of different light–matter coupling strengths, where in order to change the coupling strength we changed the overlap between the nanofiber and the atom cloud.

Figure 6.4(a) shows the acquired steady state transmission versus realized optical densities, where the probe has been scanned over $\Delta_a = \Delta_c = \Delta = \pm 32\,\mathrm{MHz}$ around atomic resonance. The corresponding coupling strengths have been inferred from fitting our transmission model in Eq. (2.22) to the recorded spectra, where in Fig. 6.4(b) we show an exemplary spectrum for $\mathrm{OD} = 39.7$, indicated in (a) as vertical blue line. For data analysis, we first fit the empty resonator spectrum to the recorded reference spectra to quantify the

TU Bibliothek Your knowledge hub WIEN
Die approbierte gedruckte Originalversion dieser Dissertation ist an der TU Wien Bibliothek verfügbar.
The approved original version of this doctoral thesis is available in print at TU Wien Bibliothek.

coupling parameters $\kappa_0 = 2\pi \times 0.33\,\text{MHz}$ and $\kappa_{\text{ext}} = 2\pi \times 0.39\,\text{MHz}$, slightly higher compared to our first measurements in [53], presumably due to excessive exposure to Cesium. Furthermore, although the resonator has been set to have its central resonance line up with the atomic resonance, we monitor the change of Δ_c between the empty resonator and the coupled resonator spectra via fitting to check for an additional parasitic drift of the resonator, when being unlocked during the measurement. Note that, such a parasitic drift, other than the known shift of less than 100 kHz (see chapter 4) has only been observed occasionally and indicated instability of the experiment, where the corresponding runs had to be re-measured. Finally, after inferring the cavity parameters, we fit our transmission model to the coupled atom–resonator system, where the number of atoms N is the only free fitting parameter.

To summarize the outcome of this measurement, in Fig. 6.4(a) the maximum splitting was measured to be $g_N/2\pi = 9.23\,\text{MHz} = 1.3 \times \nu_{\text{FSR}}$, placing us well into the multimode strong coupling regime. To his end we coupled 2360 atoms to the resonator resulting in an $\text{OD} = 52$. At the same time, we reach $g_N^2/\gamma_l = 28 \times \nu_{\text{FSR}}$, a regime where we claim that Tavis-Cummings approach cannot be applied successfully.

As one can see in Fig. 6.4(b), when comparing the fitted spectra to the data, although the positions of resonances are described well, we do observe deviations between fit and data on the red detuned side of atomic resonance. This behaviour could later be identified as a slight change in optical density during a single scan. This could be confirmed observing the accompanying OD measurement as for instance in 6.4(c). Here, we plot the acquired data in blue and in red we plot the calculated single-pass transmission for the inferred number of atoms from the fitted spectrum in 6.4(b). Note that inverting the frequency scan direction, the asymmetry does not invert, underlining that we really observe the OD changing over time. Nevertheless, the fit overlaps well on the blue detuned side of atomic resonance, and the width of area where there is no transmission is nicely reproduced. Note that also here we observe a slight residue of the resonator in the single-pass transmission measurement caused by not being able to exactly fully overcouple the resonator. Hence, both the reference and probe pulse experience residue of cavity resonances perturbing the quality of the OD fit.

After moving to Berlin, we installed a longer and finer resonator, for which in Fig. 6.5 we show the steady state spectra of the loaded resonator. This implementation features $\nu_{\text{FSR}} = 4.5\,\text{MHz}$ and $\delta\nu = 420\,\text{kHz}$, hence a finesse $F \approx 10.7$. Note that the slightly higher finesse compared to the first implementation (see chapter 4) presumably originates in the resonator lock update, where we re-did one of the fiber splices inside the fiber ring.

Assuming the same single-atom OD_1 as for the Viennese resonator, a qualified assumption due to having the same nanofiber specifications and similar MOT dynamics, the single-atom coupling strength was inferred to be $g_1 = 2\pi \times 0.14\,\text{MHz}$. The slightly lower value compared to Vienna can be explained by having a lower free spectral range. Nevertheless, the better finesse of the resonator features a higher intrinsic single-atom cooperativity $C_1 = 0.085$. Most importantly, with this new implementation, the asymmetry of the spectrum has been reduced due to faster probing. However, we did not expect to see any new features compared to the Viennese resonator but could show that the quality of the acquired spectrum is far improved with the updated resonator setup.

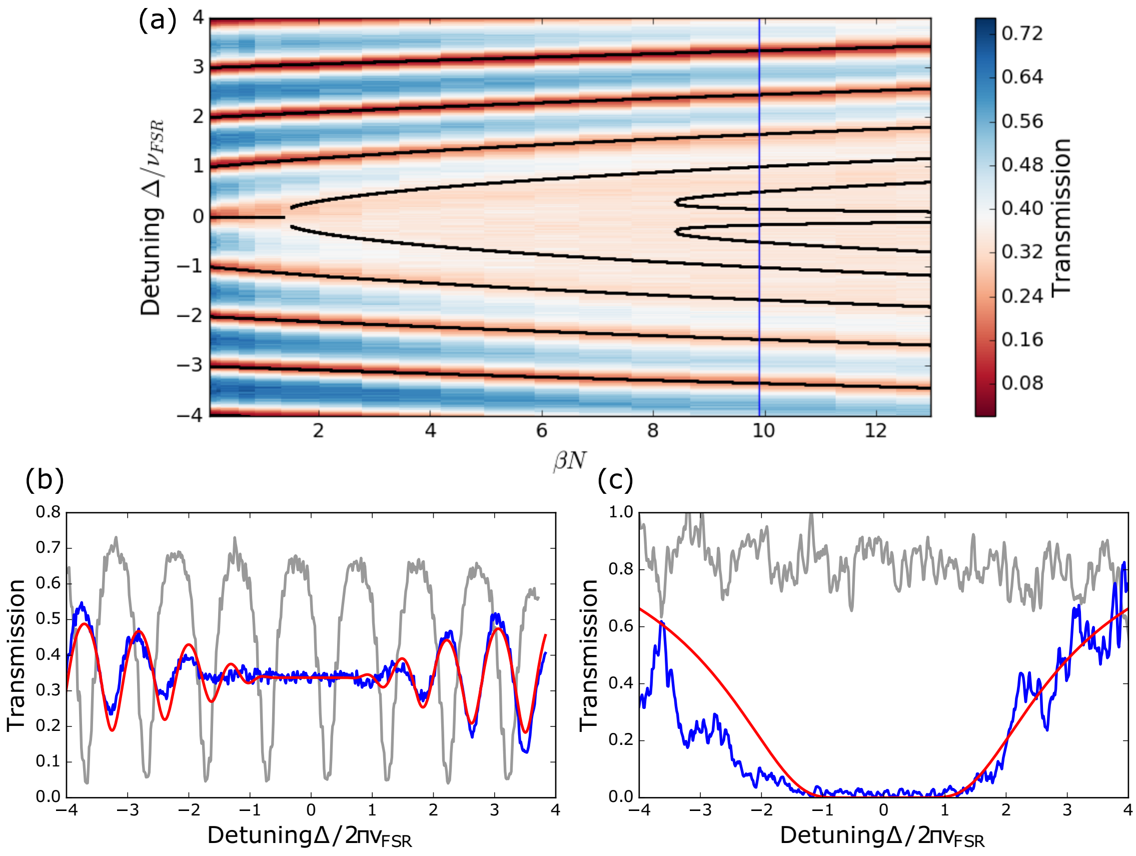

Fig. 6.4 (a) Transmission through the coupling fiber as a function of atoms coupling to the resonator. We see a clear transition, first, into the strong coupling regime and second, into the multimode strong coupling regime. As a guide to the eye, the expected resonances, calculated from Eq. (2.38) have been plotted on top of the data. Our full model has been fitted to the measured transmission, as shown in (b). In (c) we show a plot of the optical density, i.e., the transmission for the fully ovecoupled resonator, measured in parallel to the spectrum. Here, the theoretical curve shown in red is plotted for the number of atoms inferred from the fit in (b). The asymmetry of the measured data between positive and negative detuning is due to a change of OD during the individual measurements.

To summarize, conducting these experiments we could show, that the acquired data supports our theoretical predictions, where we observe a continuation of splitting exceeding $\nu_{\mathrm{FSR}}/2$, being the limit derived using a multimode Tavis-Cummings approach. To underline this finding, the data shown in Fig. 6.4(a) is overlapped with the theoretical predictions for the position of resonances derived from Eq. (2.38), where both, theory and data do not appear as if the splitting saturates.

On the other side, we were unable to observe the predicted emergence of new resonances. As seen for the theoretical predictions in Fig. 6.4(a) we should be able to see new resonances appearing for $\beta N \approx 8.5$, although for those predictions the loss of the system is not considered.

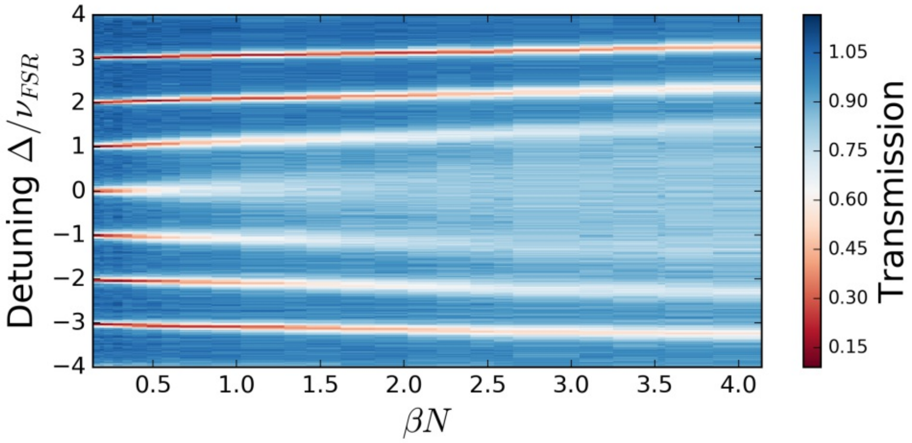

Fig. 6.5 Steady state transmission for the resonator set up in Berlin, featuring much finer resonances, for increasing coupling strengths up to $g_N/2\pi = 3.96$, coupling approximately 760 atoms.

Comparing to the theory considering loss, shown in red in Fig. 6.4(b) and in Fig. 6.3(c), it becomes obvious that as the new resonances emerge, they immediately fuse with the central plateau, where the absorption from the atomic ensemble is largest. For the resonator implementation shown in Fig. 6.4, only for even higher number of coupled atoms (OD $\geq$ 100), the position of the first new resonance is shifted outwards far enough, such that the visibility exceeds 0.02. Even for the much finer resonator realized in Berlin, the optical densities necessary to realize conditions for which the new resonances can be seen remain experimentally challenging, where instead we probably need to shorten the resonator as discussed in 6.2.2. The confirmation of whether our predictions for the new resonances are correct is therefore still pending.

6.3 Further experiments - Pulsed excitation of fiber coupled atoms

6.3.1 Dynamics of multimode strong coupling

After we successfully investigated the steady state transmission of multimode strong coupling, we were interested in the time-domain of the coupled atom–resonator system. For this purpose, we send pulses with a duration much shorter than the resonator's roundtrip time into the system and observe their repeated interaction with the atomic ensemble. In this setting, pulsed revivals of the atomic inversion on the time scale of the roundtrip time of the resonator have been predicted [129, 130].

However, already when testing the pulsed excitation setup in a fully overcoupled resonator we recognized compelling collective interaction effects in the recorded pulses. Thus, we intended to do pulsed measurements more systematically in the fully overcoupled regime, where the setup is equivalent to a waveguide without a resonator around.

6.3.2 Simplified experimental setup

Experimentally, to generate the required length pulse of about $1-30$ ns, our probe setup was extended by an EOM-controlled fiber-integrated Mach-Zehnder interferometer[2] used as a switch. By sending an electronic pulse the EOM changes the phase in one of the interferometer arms quickly such that the device becomes transmitting. For the generation of the electronic pulses, we use a programmable pulse generator[3] and a fast amplifier[4]. With this, the generation of optical pulses of $0.25-25$ ns with rise times < 1 ns is possible.

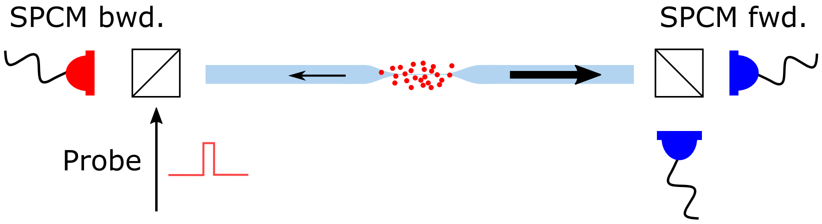

Fig. 6.6 The fully overcoupled resonator acts as a long waveguide coupled to an ensemble of atoms via the nanofiber. We excite the atoms with a short pulse provided by a fast EOM intensity modulator and record the resulting response of the atoms in forwards direction with 2 SPCMs (allowing for coincidence measurements) and 1 SPCM in backwards direction.

For the first implementation of measurements, we set the resonator to be fully overcoupled, such that the probe light enters the resonator and leaves after only one roundtrip. With our pulses being at most 25 ns long, the measurement was conducted stroboscopically with very high repetition rates to mitigate the low number of photon counts per single run. Since we operate in the low excitation regime, we detect less than one photon per pulse. In more detail, after initially loading the MOT, we interrupt the MOT beams for 1 ms and send a single short excitation pulse through the nanofiber. This is typically repeated about 800.000 times during a 2-hour measurement. We acquire the transmitted light through the ensemble with 2 SPCMs in forward direction and a single SPCM collects photons reflected from the atomic ensemble, in backwards direction. The data is sorted into histograms featuring 125 ps bin size. The simplified setup is shown in Fig. 6.6 and an example of a recorded transmission of 25 ns pulse is plotted in Fig. 6.7 for an OD = 6.6 (a) and OD = 33.2 (b).

6.3.3 Observations

When sending 25 ns pulses into the ensemble, we observed that the decay time of the temporal slope of the absorption as well as the re-emission of photons after the pulse has been switched off can be much shorter than the natural decay time of Cs and that this decay time depends on the optical density of the coupled ensemble of atoms. Furthermore, we observe a sharp revival of transmission when the probe pulse is switched off, as can be seen in Fig. 6.7(b).

---

[2] iXBlue NIR-MX800-LN-10, max. 10 GHz modulation frequency

[3] Highland Technologies T240-1

[4] DR-PL-10-MO

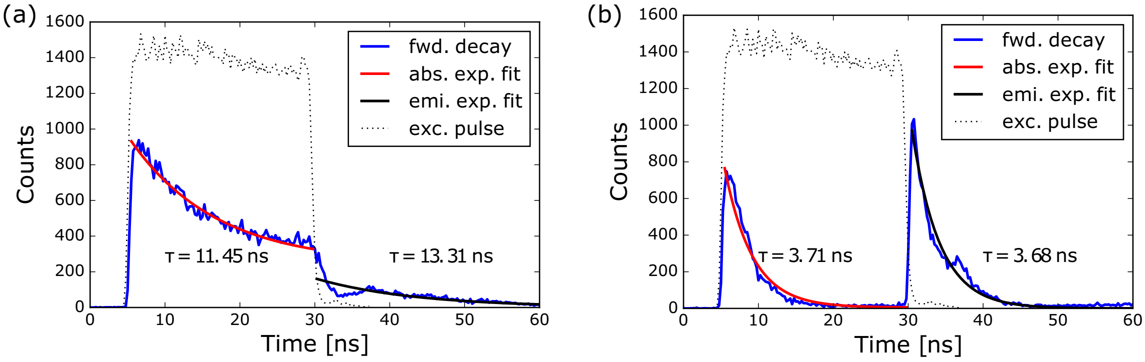

Fig. 6.7 Measured data (blue) in forward direction when exciting the ensemble with a 25 ns pulses (black dotted line). (a) For OD = 6.6 we already see a decrease in decay time τ compared to the natural atomic decay time of 30 ns. In the re-emission pulse, we can also observe some oscillatory behaviour, that suggests, fitting an exponential decay to the data (black) might not reveal a correct description, which is subject to our current research. (b) For OD = 33.2 both the fitted absorption (red) and re-emission (black) are even more significantly sped up by a factor of ~ 8 with respect to the natural spontaneous decay.

The latter behaviour is expected for probing an ensemble with short pulses, being a consequence of the interference of collective forward scattering of light from the atomic ensemble with the excitation field passing the ensemble. While these light fields destructively interfere, we observe an absence of light in the temporal shape of the transmitted pulse. Once the probing pulse is switched off only the emitted light is left. Thus, the destructive interference vanishes, resulting in a sudden intensity rise, similar to Fig. 6.7(b).

It has been shown in [131] that the intensity of the emitted light can surpass the level of the excitation pulse, an effect that has been called superflash. This peak intensity only depends on the phase between the input and scattered light, determined by the probing laser-detuning from atomic resonance. Depending on the coupling strength between the atomic ensemble and the waveguide, one can find a detuning to maximise the intensity of re-emitted light to be maximally 4 times the input intensity. Note that the observed increase of intensity in the re-emitted light in our measurements is not as pronounced as in the experiment cited above. Supposedly, this is due to us exciting the ensemble well below saturation intensity with pulse lengths, where the spectral width of our excitation pulse exceeds the width of the atomic linewidth, thus, the probe laser–atom detuning is not as well defined. For further investigations, we plan on measuring the temporal response for a given ensemble with large detuning compared to the atomic linewidth, up to $\Delta = 10\Gamma$, where we assume to observe a similar effect.

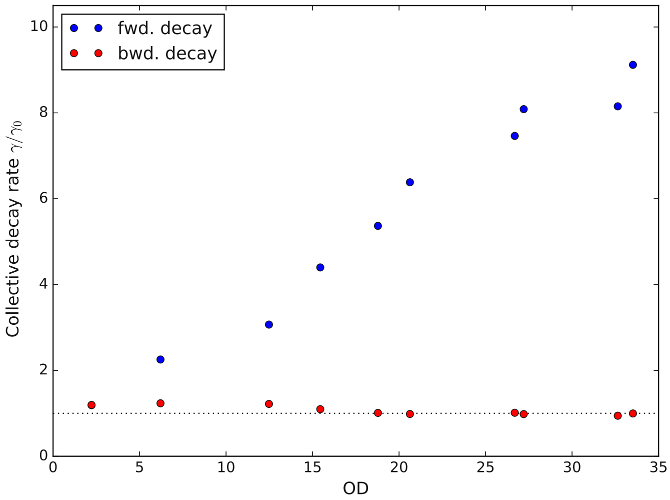

Fig. 6.8 Fitted decay time after pulse switch off versus optical density in forwards (blue) and backwards (red) direction. While the forward emission experiences an atom number dependent increase in decay rate, the backwards decay remains approximately constant at $2\gamma_0 = 2\pi \times 5.22\,\mathrm{MHz}$.

More importantly, before investigating transmission characteristics depending on the detuning in greater detail, we were interested to systematically investigate the atom number dependency on the decay times of absorption and re-emission, when probing with 25 ns pulses, resonant to the Cs D2 line. Fitting an exponential decay to the slope of re-emitted light, we obtained a decay rate with the corresponding results shown in Fig. 6.8. In the figure one observes, that in forwards direction there is an approximately linear dependency of the collective decay rate on the number of coupled atoms. We note that the decay is only exponential for short time scales and for larger time scales one can see oscillations that appear more pronounced with higher ODs. Furthermore, while evaluating the collected data for this thesis, I noticed that for higher optical densities, the stroboscopic loading of the MOT might lead to a different optical density than those measured before in a steady state after loading the MOT for two seconds. This discrepancy between the two experimental realizations is particularly striking for higher optical densities and leads to an overestimation of OD shown in Fig. 6.8.

Interestingly, for the pulses detected in backwards direction, when excited with resonant light (compare Fig. 6.9(b)) we noticed no increased decay of the atomic ensemble after it has been excited, independent of excitation pulse power and optical density of the ensemble. Furthermore, the number of photons emitted in backwards direction is two orders of magnitude smaller than in forwards direction. This observation supports our understanding that only in forwards direction the emission processes interfere constructively.

Another interesting observation of the pulsed measurements is the observation of quantum beats [132] when probing with short excitation pulse lengths, such that the bandwidth of the probe pulse is on the order of the level spacing between the F'=4 and F'=5 excited state hyperfine level. In this regime, the two levels can both be excited and as the transitions have a frequency difference of 250 MHz, the resulting emitted light will oscillate between constructive and destructive interference between the two emission paths. Figure 6.9(a) shows the behaviour after an excitation with a 2 ns pulse resulting in an oscillation of re-emitted light with a period of around 4 ns $\approx 1/(250MHz)$. We attribute this to quantum beats and unfortunately this oscillation masks other predicted oscillatory effects [129, 130] and prevents a precise determination of the decay time. One way to circumvent this would be to excite the ensemble on the D1 line of Cs at 894 nm, where the hyperfine splitting of the excited state $\Delta = 1.167$ GHz, is 4.5 times larger.

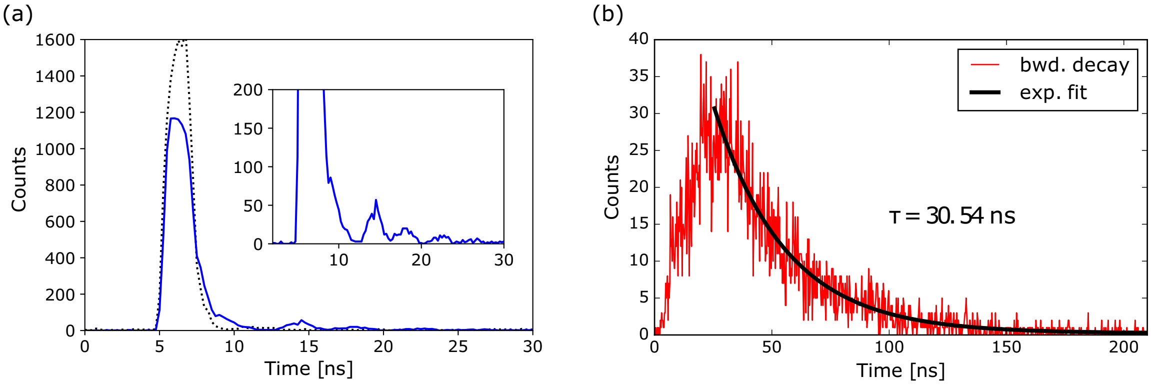

Fig. 6.9 (a) For the shorter 2 ns excitation pulse the dynamic of absorption and re-emission is much weaker as for the 25 ns pulse and the oscillations in the emitted light, known as quantum beats, mask the collective behaviour we want to investigate. (b) In backwards direction, we observe for a 25 ns pulse the usual unaltered spontaneous decay time $\tau = 1/2\gamma$ fitted here to be $\tau = 30.54$ ns.

Ultimately, our measurements confirmed that we observe a collective response of the atomic ensemble coupled to a nanofiber, when excited with an optical pulse, that is much shorter than the natural atomic decay time. In previous measurements, where the dynamics of a cold atomic ensemble to the sudden switch-on and -off of an excitation pulse have been measured [133–135], oscillations depending on the detuning of the excitation pulse have been observed, where the initial slope can change much faster than the atomic decay time. As it turned out, for the measurements performed so far, our excitation pulses were too short to fully resolve any oscillatory behaviour expected on time scales of a few atomic decay times. Nevertheless, the necessary adaptations to prolong the pulse length are easily implemented, where our setup is ideally suited to investigate this collectively enhanced, superradiant behaviour of the ensemble, especially since compared to the experiments in the aforementioned citations, we have an advantage of being able to couple the ensemble to a nanofiber allowing for efficient excitation and collection of photons from the ensemble.

Chapter 7

Summary and Outlook

7.1 Summary

During the course of this thesis, an experiment was set up and conducted, that allowed us to enter the multimode strong coupling regime. While that regime has recently been observed in circuit QED [35, 36] we are the first group to experimentally enter this regime by using optical wavelengths and cold atoms. This way, our experiment could spark far more investigation of multimode strong coupling in the optical regime using similar experimental platforms such as [55, 58, 136].

The experimental setup developed during this thesis, is a versatile apparatus allowing to trap and cool atoms in a magneto optical trap (MOT) around a nanofiber. With this we could optimise the atomic cloud to reach optical densities exceeding $\mathrm{OD} = 50$, when probed through the nanofiber. Additionally, we determined the single-atom channelling efficiency to be $\beta = 0.0055$ using correlation measurements of fluorescence photons emitted from to ensemble into the nanofiber.

The backbone of our experiment is a long fiber ring resonator with an integrated nanofiber section, where the unique length independence of cooperativity of such a resonator allowed us to reach multimode strong coupling in two settings, by collectively coupling up to 2300 atoms to a 29.3 m long resonator and up to 1000 atoms to a 45.5 m long resonator. Our results show that in this regime the standard description of collective atom–resonator coupling - the Tavis-Cummings model - does not apply any more. We observed significant deviations of our measurement from the behaviour expected from the multimode version of the Tavis-Cummings model, that predicts limited normal-mode splitting for the multimode strong coupling case, while the measured splitting exceeds the free spectral range of the resonators significantly.

To derive an accurate theoretical model of our experiment, we used a bottom-up approach, where we applied a real-space formalism relying on the position dependent photon field in the resonator. Extending this formalism to a ring cavity we then derived an accurate Hamiltonian of the coupled system. Our predictions, in contrast to the Jaynes- and Tavis-Cummings model, agree well with the measured spectra in the multimode strong coupling regime. This shows that the introduced framework, that merges the description of waveguide and cavity

TU Bibliothek WIEN Your knowledge hub

QED is well suited to describe the physics of this new regime of light-matter coupling. In the end, our theoretical approach revealed boundaries for the validity of the established Jaynes- and Tavis-Cummings model, that fail as soon as the atom induced scattering rate from the cavity g_N^2/γ_l becomes large with respect to the resonator's free spectral range, a situation that occurs under many experimental settings, e.g., [137–140].

7.2 Outlook

Our measurements and theoretical derivation point towards a new regime of collective strong coupling where, e.g., a set of additional resonances is expected. However due to their reduced visibility we have not yet been able to observe the predicted new resonances of the coupled system. To do so, we have to reduce the linewidth of the resonator, i.e., to minimize the intra-cavity loss. Furthermore, the long-term stability of atom number needs to be improved, to minimize washing out of spectral features due to averaging over many experimental runs. From our observations, a shorter resonator around 5 m length and a finesse of at least 30 would be a good candidate for obtaining spectra showing new resonances, which is in reach of our experimental capabilities, as seen in 4.5 for the resonator setup in Berlin.

Additionally, for further studies trapping of atoms in the resonator field would be beneficial, which would increase the life-time of atoms in close vicinity of the fiber and enable a more stable and reliable number of atoms coupled to the resonator. In this way, more complex protocols could be established, for example, would it allow more effective excitation of the ensemble using Bragg angles [25] to couple light into the resonator.

Using a traditional two-colour dipole trap with fiber guided light in the nanofiber [23–25] can be experimentally challenging for our ring resonator. We observed an extreme sensitivity of resonator stability to high powers inside the nanofiber causing fast fluctuations of our cavity's resonances. Thus, a perquisite for trapping is an improved locking mechanism which could potentially be realized utilizing the thermal self-stability effect in a nanofiber [55, 141]. Moreover, for the variable beamsplitter at hand, the trapping light, although subject to different resonator finesse, would still have to be resonant to the cavity. Together with the fact that the cavity is subject to a strong wavelength dependent birefringence, trapping in the fiber fields requires the development of a suitable coupling method.

A more realistic way to implement trapping and a general improvement of the versatility of the setup could be established by replacing the fiber-beamsplitter by a so-called null coupler [142–144]. Here, two fibers are fused together creating a four-port coupler. In the idle state there is no coupling between the input of the first and output of the second fiber. However, a flexural acoustic wave, provided by an attached piezo can facilitate an almost 100% transition from one fiber to the other. Most importantly, providing several excitation frequencies allows for the independent control of the wavelength that would be coupled in and out of the resonator. In this way, one could decide which wavelengths should be resonantly enhanced and which not.

Alternatively, a trapping configuration with light from the outside could be employed, where two strong planar waves, impinging on the nanofiber at an angle, could create a standing-wave trapping potential either in the field reflected from the fiber or in the focus

TU Bibliothek WIEN Your knowledge hub
Die approbierte gedruckte Originalversion dieser Dissertation ist an der TU Wien Bibliothek verfügbar.
The approved original version of this doctoral thesis is available in print at TU Wien Bibliothek.

behind the nanofiber [145]. Furthermore, on could use an optical tweezer to trap atoms in close vicinity of the nanofiber surface in order to couple effectively to the resonator mode [146].

Currently we are investigating the temporal response of the atomic ensemble to short excitation pulses featuring a superradiant behaviour. Preliminary results show a reduced decay rate of the ensemble which depends on its optical density. We will continue this investigation of collective atom–light interaction, where our system operating at the boundary between cavity QED and waveguide QED could experimentally reveal a transition of coupling to a finite set of quantized modes to coupling to the continuum of vacuum modes in free space [134, 135]. Furthermore, our experimental platform is ideally suited to study the predicted non-Markovian dynamics in long fiber resonators [147] or the dynamics predicted for the superstrong coupling regime, where, e.g., Rabi oscillations expected for driven atom–resonator systems are replaced by pulsed revivals [129, 130]. Most importantly, observing this behaviour requires high optical densities, where in this regime the Tavis-Cummings model is not expected to result in accurate predictions. However, the description derived in this thesis is well suited given its wide range of applicability. Finally, we are interested in exploring the multimode strong coupling regime in the time domain, where we excite the atomic ensemble with an extremely short probing pulse (~ 1 ns), observing the multimode strong coupling spectrum in the Fourier-transform of the temporal response of the ensemble.

Another route of research would utilize our long fiber ring resonator outside of multimode strong coupling, following a more general two-mode approach, where the atoms couple to the resonator mode as well as a propagating mode, to observe, e.g., vacuum-induced transparency [148, 149]. Other possible applications for our ring resonator are quantum annealing algorithms using atoms [150] or photons [151] as carriers of information. Furthermore, based on the recent observation of collectively enhanced non-linearities in light–matter interaction between an atomic ensemble and nanofiber guided light [65, 105], it could be interesting to study such non-linear effects in cavity enhanced fields.

App. A

Driven optical cavity with loss

In this section I present, how to derive the dynamics of a driven cavity subject to losses using a master-equation approach based on the Jaynes-Cummings Hamiltonian. For a general introduction to master-equations used for solving open quantum systems refer to [52]. For the explicit solution of the case of a single atom coupled to a whispering gallery mode resonator interfaced with a waveguide, which is analogue to our scenario, refer to [152, 153].

In the main text we assume a Fabry-Pérot cavity driven by a coherent light source through one of the mirrors, as shown in Fig. A.1. The cavity can lose energy to the environment via absorption and scattering in the mirrors, indicated by the loss rate $\kappa = \kappa_{\text{ext}} + \kappa_0$. Inside the cavity there is a coupled two-level atom with energy spacing $\hbar\omega_{\text{at}}$ that undergoes spontaneous emission into free space with the decay rate γ_l. The Hamiltonian of the system is given by the Jaynes-Cummings Hamiltonian with an additional driving term

$$\hat{H}/\hbar = \Delta_c \hat{a}^\dagger \hat{a} + \Delta_a \hat{\sigma}_+ \hat{\sigma}_- + g\left(\hat{a}^\dagger \hat{\sigma}_- + \hat{a}\hat{\sigma}_+\right) + i\varepsilon\left(\hat{a} - \hat{a}^\dagger\right), \tag{A.1}$$

where $\Delta_a = \omega - \omega_{\text{at}}$ is the detuning of the atomic resonance and $\Delta_c = \omega - \omega_c$ the cavity resonance frequency with respect to the driving probe light of frequency ω. The driving term is given by $\varepsilon = \sqrt{2\kappa_{\text{ext}}} S_0$, where κ_{ext} is the coupling strength for the the light in- and outside of the cavity and S_0 is the driving field amplitude.

The master equation is given by

$$\frac{d\hat{\rho}}{dt} = -\frac{i}{\hbar}[\hat{H}, \hat{\rho}] + \mathscr{L}, \tag{A.2}$$

with $\hat{\rho}$ being the density matrix of the system. In the weak driving limit, where we assume at most a single excitation, the base states spanning the density matrix are $\{|g,0\rangle, |g,1\rangle, |e,0\rangle\}$. In this approach, the losses from the open system are considered via the Liouvillian operator, defined for our system as

$$\mathscr{L} = \gamma_l \left(2\hat{\sigma}_- \hat{\rho} \hat{\sigma}_+ - \hat{\sigma}_+ \hat{\sigma}_- \hat{\rho} - \hat{\rho} \hat{\sigma}_+ \hat{\sigma}_-\right) + (\kappa_0 + \kappa_{\text{ext}}) \left(2\hat{a}\hat{\rho}\hat{a}^\dagger - \hat{a}^\dagger \hat{a} \hat{\rho} - \hat{\rho}\hat{a}^\dagger \hat{a}\right), \tag{A.3}$$

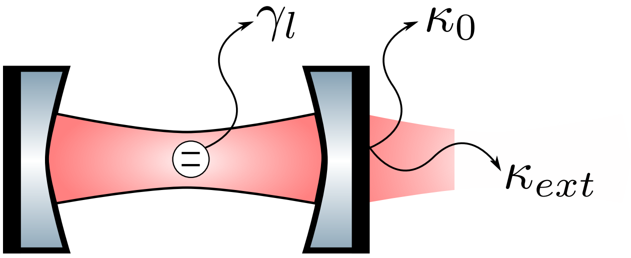

Fig. A.1 Sketch of a driven Fabry-Pérot cavity coupled to a two-level atom. The cavity loss can be identified as κ_0, the intrinsic loss and κ_{ext}, the loss due to coupling to a dedicated driving field. Furthermore, the atom can decay into the surrounding continuum of modes via spontaneous emission with the rate γ_l.

where $\gamma_l = (1-\beta)\gamma$ is the atom decaying into the continuum of surrounding non-cavity modes. Here, we assume the atom emits a photon into the cavity proportional to a rate $\beta\gamma$, where γ is the spontaneous decay rate of an atom and β the corresponding channelling efficiency.

One can solve for the expectation values of an observable $\hat{O}$ of the system in the steady state using the relation $\langle\hat{O}\rangle = \text{Tr}[\hat{\rho}\hat{O}]$. With this the master equation can be simplified to be

$$\frac{d}{dt}\langle\hat{O}\rangle = -\frac{i}{\hbar}\langle[\hat{O},\hat{H}]\rangle + \frac{\Gamma}{2}\left\langle[\hat{c},\hat{O}]\hat{c}^\dagger + \hat{c}^\dagger[\hat{O},\hat{c}]\right\rangle, \tag{A.4}$$

where $\hat{c}$ are the jump operators of the system and Γ the corresponding decay channels, i.e., κ_0, κ_{ext} and γ_l. Solving for the observables, $\langle\hat{a}^\dagger\hat{a}\rangle$, the number of excitations in the cavity field and $\langle\hat{\sigma}_+\hat{\sigma}_-\rangle$, the atomic excitation probability, one gets

$$\begin{aligned}\langle\hat{a}^\dagger\hat{a}\rangle &= \frac{\varepsilon^2\left(\gamma_l^2+\Delta_a^2\right)}{g^4+2g^2(\gamma_l(\kappa_0+\kappa_{\text{ext}})-\Delta_a\Delta_c)+\left(\gamma_l^2+\Delta_a^2\right)((\kappa_0+\kappa_{\text{ext}})^2+\Delta_c^2)}\\ \langle\hat{\sigma}_+\hat{\sigma}_-\rangle &= \frac{\varepsilon^2 g^2}{g^4+2g^2(\gamma_l(\kappa_0+\kappa_{\text{ext}})-\Delta_a\Delta_c)+\left(\gamma_l^2+\Delta_a^2\right)((\kappa_0+\kappa_{\text{ext}})^2+\Delta_c^2)},\end{aligned} \tag{A.5}$$

where

$$P_a = \frac{\langle\hat{\sigma}_+\hat{\sigma}_-\rangle}{\langle\hat{a}^\dagger\hat{a}\rangle} = \frac{g^2}{\gamma_l^2+\Delta_a} \tag{A.6}$$

is the probability of exciting the atom through the mean cavity field.

In a next step we can solve for the spectral features of the system revealed when comparing the output field to the input $\frac{\langle S_{\text{out}}\rangle}{\langle S_0\rangle}$ of the single sided cavity. For the output field $\langle S_{\text{out}}\rangle$, being the superposition of the input field $\langle S_0\rangle$ and the out-coupled cavity field, we obtain $\langle S_{\text{out}}\rangle = \langle S_0\rangle - i\sqrt{2\kappa_{\text{ext}}}\langle\hat{a}\rangle$. With this, the measured signal can be determined to be

$$\frac{\langle S_{\text{out}}\rangle}{\langle S_0\rangle} = 1 - i\sqrt{2\kappa_{\text{ext}}}\frac{\langle\hat{a}\rangle}{\langle S_0\rangle} = \frac{g^2+(\gamma_l+i\Delta_a)(\kappa_0-\kappa_{ext}+i\Delta_c)}{g^2+(\gamma_l+i\Delta_a)(\kappa_0+\kappa_{ext}+i\Delta_c)}. \tag{A.7}$$

App. B

Multimode expansion for Jaynes- and Tavis-Cummings model

When calculating the spectral features of a coupled atom–resonator system once ν_{FSR} comes of the order of the coupling strength g, it is required to take into consideration more than just the central resonance. Starting from the standard Jaynes-Cummings approach we can add the contributions of the additionally considered resonator modes to the Hamiltonian to obtain

$$\frac{\hat{H}}{\hbar} = \sum_j \omega_j \hat{a}_j^\dagger \hat{a}_j + \omega_{\mathrm{at}} \hat{\sigma}_+ \hat{\sigma}_- + g \sum_j \left(\hat{\sigma}_+ \hat{a}_j + \hat{\sigma}_- \hat{a}_j^\dagger \right), \tag{B.1}$$

where $\hat{\sigma}_+$ ($\hat{\sigma}_-$) is the atomic raising (lowering) operator, $\hat{a}_j^\dagger$ ($\hat{a}_j$) creates (annihilates) a photon in the n-th mode of the resonator and we assume $g \in \mathbb{R}$. The resonator modes, separated by the free spectral range $\omega_{\mathrm{FSR}} = 2\pi\nu_{\mathrm{FSR}}$ are given by $\omega_j = j\,\omega_{\mathrm{FSR}} + \Delta_a$, where Δ_a is the atom–resonator detuning, defined for the resonance closest to ω_{at}.

In a similar way, we can apply this expansion to the Tavis-Cummings approach

$$\frac{\hat{H}}{\hbar} = \sum_j \omega_j \hat{a}_j^\dagger \hat{a}_j + \omega_{\mathrm{at}} \hat{S}_+ \hat{S}_- + \sqrt{N} g \sum_j \left(\hat{S}_+ \hat{a}_j + \hat{S}_- \hat{a}_j^\dagger \right), \tag{B.2}$$

where we made use of the single-excitation spin wave operators $\hat{S}_\pm = 1/\sqrt{N} \sum_n \hat{\sigma}_n^\pm$, to consider a collective N-atom–resonator interaction. For simplicity, the remainder of the derivation is shown for the Jaynes-Cummings method, but works analogously for Tavis-Cummings.

Setting the zero point of the energy scale to atomic resonance, $\omega_{\mathrm{at}} = 0$ we arrive at a simplified Hamiltonian, given by

$$\frac{\hat{H}}{\hbar} = \sum_j \left[\omega_j \hat{a}_j^\dagger \hat{a}_j + g \left(\hat{\sigma}_+ \hat{a}_j + \hat{\sigma}_- \hat{a}_j^\dagger \right) \right]. \tag{B.3}$$

To solve the Schrödingers equation $H|\Psi\rangle = \varepsilon|\Psi\rangle$, we make a single-excitation wavefunction ansatz

$$|\Psi\rangle = \sum_j \alpha_j \hat{a}_j^\dagger + \beta \hat{\sigma}^+, \tag{B.4}$$

where for applying the ansatz to the simplified Hamiltonian and comparing coefficients we obtain

$$\begin{aligned} \alpha_j &= \frac{g\beta}{\omega' - j\,\omega_{\mathrm{FSR}} - \Delta_a} \\ \beta &= \frac{g}{\omega'} \sum_j \alpha_j . \end{aligned} \tag{B.5}$$

Combining these findings, we can formulate a resonance condition for the coupled resonators eigenfrequencies

$$1 = \frac{g^2}{\omega'} \sum_{j=-J}^{J} \frac{1}{\omega' - j\,\omega_{\mathrm{FSR}} - \Delta_a}, \tag{B.6}$$

having $2(J+1)$ solutions that require numerical methods to be solved for.

However, since we are only interested in the limiting case of very large coupling strengths, where $g \gg \omega_{\mathrm{FSR}}$ one can solve for the new eigenfrequencies analytically via defining $\omega' = m\omega_{\mathrm{FSR}}$ ($m \in \mathbb{R}$) and expanding the sum to include all longitudinal modes inside the resonator. Thus, we can reformulate the resonance condition to be

$$m = \frac{g^2}{\omega_{\mathrm{FSR}}^2} \sum_{-\infty}^{\infty} \frac{1}{m - n - \tilde{\Delta}_a}, \tag{B.7}$$

where $\tilde{\Delta}_a = \Delta_a/\omega_{\mathrm{FSR}}$. In this regime, one can approximate $m\frac{\omega_{\mathrm{FSR}}^2}{g^2} \rightarrow 0$, such that

$$0 = \sum_{-\infty}^{\infty} \frac{1}{m - j - \tilde{\Delta}_a}. \tag{B.8}$$

This equation can be satisfied for $m = \frac{1}{2} + \tilde{\Delta}_a + J$, where when plugged into Eq. (B.8) yields

$$\sum_{-\infty}^{\infty} \frac{1}{(2J+1)/2 - j} \approx 0, \tag{B.9}$$

for each $J \in \mathbb{N}$. With this ansatz for the energy shift, we find for the coupled atom–resonator system for large coupling strengths the position of maximally split resonances at frequencies

$$\tilde{\omega}_j = \omega_j + \frac{1}{2}\omega_{\mathrm{FSR}} = j\omega_{\mathrm{FSR}} + \Delta_a + \frac{1}{2}\omega_{\mathrm{FSR}}, \tag{B.10}$$

where j is the resonance's mode-number. Thus, to conclude, all resonances initially positioned at $j\omega_{\mathrm{FSR}}$ are shifted by $\omega_{\mathrm{FSR}}/2$, where the shift saturates.

Die approbierte gedruckte Originalversion dieser Dissertation ist an der TU Wien Bibliothek verfügbar.
The approved original version of this doctoral thesis is available in print at TU Wien Bibliothek.
TU Bibliothek Your knowledge hub WIEN

App. C

Transmission coefficients of the coupling beamsplitter

In order to couple a waveguide to our fiber ring resonator featuring chiral light–matter interaction we use a beamsplitter matrix given by

$$\hat{U}_{bs} = t_{\mathrm{rt}} \left(i v_c t_1 \hat{a}(L) \hat{a}^\dagger(0) + \sqrt{v_c v_g} t_2 \hat{a}(L) \hat{d}^\dagger(0) \right) + i v_g t_1 \hat{c}(0) \hat{d}^\dagger(0) + \sqrt{v_g v_c} t_2 \hat{c}(0) \hat{a}^\dagger(0), \tag{C.1}$$

where t_1 and t_2 are the amplitude reflection and transmission trough the beamsplitter and t_{rt} is the single roundtrip transmission through the resonator (see Fig C.1). The group velocity inside the cavity is given by v_c and in the probing waveguide by v_g.

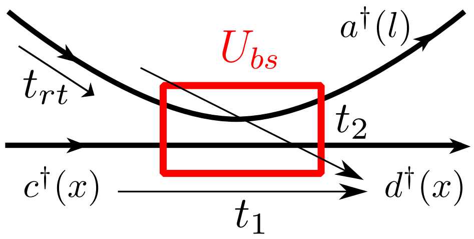

Fig. C.1 t_1 quantifies the transmission trough the beamsplitter, while t_2 quantifies the coupling between the ring resonator and input/output fiber. In order to describe intra-cavity energy loss, we introduce the single roundtrip transmission t_{rt}.

The field after one roundtrip in a loss-less resonator reads $E_{\mathrm{rt}} = t_1^2 E_0$. One can translate this into a field dissipation per roundtrip, with the roundtrip time τ_{rt}

$$\dot{E} = -\frac{1}{\tau_{\mathrm{rt}}}(E_0 - E_{\mathrm{rt}}) = -\frac{1}{\tau_{\mathrm{rt}}} E_0 (1 - t_1^2), \tag{C.2}$$

hence

$$\frac{\dot{E}}{E_0} = -\nu_{\mathrm{FSR}}(1 - t_1^2). \tag{C.3}$$

Comparing this to a field decay rate from the resonator κ_{ext} via a dedicated loss channel (for us the coupling fiber)

$$E(t) = E_0 e^{-2\kappa_{\text{ext}} t}, \tag{C.4}$$

such that

$$\frac{\dot{E}}{E_0} = -2\kappa_{\text{ext}}. \tag{C.5}$$

Plugging this equation into Eq. C.3 and using $t_2^2 = 1 - t_1^2$ one arrives at

$$\begin{aligned} t_1 &= \sqrt{1 - \frac{2\kappa_{\text{ext}}}{\nu_{\text{FSR}}}} \\ t_2 &= \sqrt{\frac{2\kappa_{\text{ext}}}{\nu_{\text{FSR}}}}. \end{aligned} \tag{C.6}$$

In an analogue derivation, one can determine the single roundtrip transmission through the fiber ring resonator to introduce loss to the cavity via an intrinsic loss rate κ_0, considering scattering and absorption in the resonator glasfiber. The final expression is given by

$$t_{\text{rt}} = \sqrt{1 - \frac{2\kappa_0}{\nu_{\text{FSR}}}}. \tag{C.7}$$

App. D

Solution to the chiral–interaction Hamiltonian

The Hamiltonian for our system considering chiral light–matter interaction is given by

$$\begin{aligned}\frac{\hat{H}}{\hbar} = &\int_{-\infty}^{0} dx\hat{c}^{\dagger}(x)\left(\omega_0 - iv_g\frac{\partial}{\partial x}\right)\hat{c}(x) + \int_{0}^{+\infty} dx\hat{d}^{\dagger}(x)\left(\omega_0 - iv_g\frac{\partial}{\partial x}\right)\hat{d}(x) + \\ &\int_0^L dl\left\{\hat{a}^{\dagger}(l)\left(\omega_0 + iv_c\frac{\partial}{\partial l}\right)\hat{a}(l) + \sum_{n=1}^{N}\left[\delta(l)\hat{\sigma}_n^{+}\hat{\sigma}_n^{-}(\omega_{\mathrm{at}} - i\gamma_l) + \right.\right. \\ &\left.\left.\delta(l-l_n)V_n(\hat{\sigma}_n^{+}\hat{a}(l) + \hat{\sigma}_n^{-}\hat{a}^{\dagger}(l))\right]\right\} + \hat{U}_{bs},\end{aligned} \tag{D.1}$$

where $\hat{c}^{\dagger}(x)$ is the input field, $\hat{d}^{\dagger}(x)$ is the output field, $\hat{a}^{\dagger}(l)$ is the cavity field, v_g (v_c) the group velocity of light in the coupling (cavity) fiber, $\hat{\sigma}_n^{\pm}$ the atomic raising and lowering operators, V_n the coupling between the cavity field and the n-th atom, ω_{at} the resonance frequency of the atomic transition and γ_l the atom-induced photonic loss rate proportional to the spontaneous emission γ. To solve the eigenvalue problem $\hat{H}|\Psi\rangle = \varepsilon|\Psi\rangle$ we make an ansatz for a single-excitation wavefunction

$$|\Psi\rangle = \left[\int_{-\infty}^{0} dx\phi_c(x)\hat{c}^{\dagger}(x) + \int_{0}^{+\infty} dx\phi_d(x)\hat{d}^{\dagger}(x) + \int_0^L dl\phi_a(l)\hat{a}^{\dagger}(l) + \sum_{n=1}^{N}\phi_{\mathrm{at},n}\hat{\sigma}_n^{+}\right]|0\rangle, \tag{D.2}$$

where for the fields we assume propagating plane waves with wavenumber k

$$\begin{aligned}\phi_c(x) &= e^{ikx}\phi_c\Theta(-x) \\ \phi_d(x) &= e^{ikx}\phi_d\Theta(x) \\ \phi_a(l) &= e^{-ikl}\sum_{n=0}^{N}\phi_n\Theta(l-l_n)\Theta(l_{n+1}-l),\end{aligned} \tag{D.3}$$

where for the cavity field $\phi_a(l)$ we apply the boundary conditions $l_0 = 0$ and $l_{N+1} = L$. Furthermore, ϕ_c (ϕ_d) is the complex excitation amplitude of the coupling waveguide field before (after) the beamsplitter. Inside the resonator the field $\phi_a(l)$ is split into a set of fields ϕ_n via Heaviside step functions Θ, where ϕ_n is the field after interaction with the n-th atom positioned at l_n. Note that for the resonator field we assume the wavenumber to be $-k$ to consider the direction of propagation of the CCW field inside the resonator. With the coupling term $\hat{U}_{bs}$ (see appendix C)

$$\hat{U}_{bs} = t_{\mathrm{rt}}\left(iv_c t_1 \hat{a}(L)\hat{a}^\dagger(0) + \sqrt{v_c v_g} t_2 \hat{a}(L)\hat{d}^\dagger(0)\right) + iv_g t_1 \hat{c}(0)\hat{d}^\dagger(0) + \sqrt{v_g v_c} t_2 \hat{c}(0)\hat{a}^\dagger(0), \tag{D.4}$$

we can plug the ansatz functions into the Schrödinger equation, using $\partial/\partial x = \partial_x$ and assuming $v_g = v_c$ to obtain:

$$\begin{aligned}
\frac{\hat{H}}{\hbar}|\psi\rangle = &- iv_g \left[\int dx \hat{c}^\dagger(x)\left[\partial_x \phi_c(x)\right] + \int dx \hat{d}^\dagger(x)\left[\partial_x \phi_d(x)\right] + \int dl \hat{a}^\dagger(l)\left[\partial_l \phi_a(l)\right]\right] \\
&+ v_g \left[it_{\mathrm{rt}} t_1 \int dl \hat{a}^\dagger(0)\phi_a(l)\delta(l-L) + t_{\mathrm{rt}} t_2 \int dl \hat{d}^\dagger(0)\phi_a(l)\delta(l-L)\right. \\
&\left. + it_1 \int dx \hat{d}^\dagger(0)\phi_c(x)\delta(x) + t_2 \int dx \hat{a}^\dagger(0)\phi_c(x)\delta(x)\right] \\
&+ \sum_{n=1}^{N}\left[\int dl \hat{\sigma}_n^+ \left[\delta\left(l-l_n\right)V_n\right]\phi_a(l) + \int dl \left[\delta\left(l-l_n\right)V_n \hat{a}^\dagger(l)\right]\phi_{\mathrm{at},n}\right. \\
&\left. + \delta(l)\hat{\sigma}_n^+(\omega_{\mathrm{at}} - i\gamma_l)\phi_{\mathrm{at},n}\right].
\end{aligned} \tag{D.5}$$

Note that in order to get this expression we reduced any operators $\hat{c}(x)\hat{c}(x') = \delta(x-x')$ and used $\hat{\sigma}_n^- \hat{\sigma}_n^+ = 1$. In the next step we evaluate the expressions

$$\begin{aligned}
\partial_x \phi_c(x) &= e^{ikx}\phi_c(ik + \delta(-x)) \\
\partial_x \phi_d(x) &= e^{ikx}\phi_d(ik + \delta(x)) \\
\partial_l \phi_a(l) &= e^{-ikl}\sum_{n=0}^{N}\phi_n\left(ik + \delta(l-l_n) + \delta(l_{n+1}-l)\right),
\end{aligned} \tag{D.6}$$

where when integrating over the edge of a integration interval for the delta-functions we obtain $\int_{-\infty}^{0} dx\delta(x) = \int_0^\infty dx\delta(x) = \frac{1}{2}$. Evaluating the plane-waves at the step of a Heavyside function gives us for the complex excitation amplitudes

$$\begin{aligned}
\phi_c(0) &= \lim_{\varepsilon\to 0}\frac{1}{\varepsilon}\int_{0-\varepsilon}^{0+\varepsilon}\phi_c(x) = \frac{\phi_c}{2} \\
\phi_d(0) &= \lim_{\varepsilon\to 0}\frac{1}{\varepsilon}\int_{0-\varepsilon}^{0+\varepsilon}\phi_d(x) = \frac{\phi_d}{2} \\
\phi_a\left(l_n\right) &= \lim_{\varepsilon\to 0}\frac{1}{\varepsilon}\int_{l_n-\varepsilon}^{l_n+\varepsilon}\phi_a(l) = \frac{\phi_{n-1}+\phi_n}{2}e^{-ikl_n}.
\end{aligned} \tag{D.7}$$

This allows us to evaluate the Schrödinger equation, yielding

$$
\begin{aligned}
&\frac{\hat{H}}{\hbar}|\psi\rangle = \frac{\varepsilon}{\hbar}|\psi\rangle = \\
&\quad v_g k\left[\int dx \hat{c}^\dagger(x)\phi_c(x) + \int dx \hat{d}^\dagger(x)\phi_d(x) + \int dl \hat{a}^\dagger(l)\phi_a(l)\right] \\
&\quad - i v_g\left[-\hat{c}^\dagger(0)\frac{\phi_c}{2} + \hat{d}^\dagger(0)\frac{\phi_d}{2} - \hat{a}^\dagger(0)\frac{\phi_0}{2} + \sum_{n=1}^{N}\hat{a}^\dagger(l_n)\left(\phi_n - \phi_{n-1}\right)e^{-ikl_n} + \hat{a}^\dagger(L)\frac{\phi_N}{2}e^{-ikL}\right] \\
&\quad + v_g\left[-it_{\mathrm{rt}}t_1\hat{a}^\dagger(0)\frac{\phi_N}{2}e^{-ikL} - t_{\mathrm{rt}}t_2\hat{d}^\dagger(0)\frac{\phi_N}{2}e^{-ikL} + it_1\hat{d}^\dagger(0)\frac{\phi_c}{2} + t_2\hat{a}^\dagger(0)\frac{\phi_c}{2}\right] \\
&\quad + \sum_{n=1}^{N} V_n\hat{a}^\dagger(l_n)\phi_{\mathrm{at},n} + \sum_{n=1}^{N}\hat{\sigma}_n^+\left[\frac{\phi_{n-1}+\phi_n}{2}e^{-ikl_n}V_n + \left(\omega_{\mathrm{at}} - i\gamma_l\right)\phi_{\mathrm{at},n}\right]
\end{aligned}
\tag{D.8}
$$

When comparing the coefficients in front of the operators we obtain a set of coupled equations

$$
\begin{aligned}
\hat{d}^\dagger(0):&\quad 0 = -iv_g\frac{\phi_d}{2} - v_g t_{\mathrm{rt}}t_2\frac{\phi_N}{2}e^{-ikL} + iv_g t_1\frac{\phi_c}{2} \\
\hat{a}^\dagger(0):&\quad 0 = iv_g\frac{\phi_0}{2} - iv_g t_{\mathrm{rt}}t_1\frac{\phi_N}{2}e^{-ikL} + v_g t_2\frac{\phi_c}{2} \\
\hat{a}^\dagger(l_n):&\quad 0 = -iv_g\left(\phi_n - \phi_{n-1}\right)e^{-ikl_n} + V_n\phi_{\mathrm{at},n} \quad n \neq 0 \\
\hat{\sigma}_n^+:&\quad 0 = V_n/2\,\left(\phi_n + \phi_{n-1}\right)e^{-ikl_n} + \left(\omega_{\mathrm{at}} - i\gamma_l - \omega\right)\phi_{\mathrm{at},n}
\end{aligned}
\tag{D.9}
$$

For the waveguide atom coupling $V_n = \sqrt{2\beta_n\gamma v_g}$ and the atom–field detuning $\Delta_a = (\omega_{\mathrm{at}} - \omega)$ we can solve this set of equations. By doing so we get the single-atom transmission

$$
\begin{aligned}
\frac{\phi_n}{\phi_{n-1}} &= 1 - \frac{2\beta_n\gamma}{\gamma + i\Delta_a} = t_{\mathrm{at},n} \quad n \neq 0 \\
\frac{\phi_0}{\phi_c} &= \frac{-it_2}{e^{-ikL}t_1 t_N t_{\mathrm{rt}} - 1},
\end{aligned}
\tag{D.10}
$$

where $t_N = \prod_{n=1}^{N} t_{\mathrm{at},n}$. The field after interfacing the coupled fiber ring resonator is given by

$$
\frac{\phi_d}{\phi_c} = \frac{t_N t_{\mathrm{rt}} e^{-ikL} - t_1}{t_N t_{\mathrm{rt}} t_1 e^{-ikL} - 1}.
\tag{D.11}
$$

and for the atomic excitation we get

$$
\frac{\phi_{\mathrm{at},n}}{\phi_c} = \frac{-\sqrt{2\beta_n\gamma v_g}\,t_2 e^{-ikl_n}}{(t_N t_{\mathrm{rt}} t_1 e^{-ikL} - 1)(\gamma + i\Delta_a)}.
\tag{D.12}
$$

We note that for small deviations of β_n one can show, using the binomial theorem, that $t_N = \prod_{n=1}^{N} t_{\mathrm{at},n} \approx t_{\mathrm{at}}^N$, where $t_{\mathrm{at}} = 1 - \frac{2\beta\gamma}{\gamma + i\Delta_a}$ is the single-atom transmission for an averaged β.

App. E

Atomic emission into the waveguide

In order to motivate the coupling strength $V_{\mathrm{at}} = \sqrt{2\beta\gamma v_g}$, we solve for the dynamic behaviour of a single initially excited atom emitting a photon into a coupled waveguide (in forwards direction). We use the reduced Hamiltonian of an atom at position $x = 0$ chirally coupled to a waveguide, given by

$$\frac{\hat{H}}{\hbar} = \int_{-\infty}^{\infty} dx \big[\hat{a}^\dagger(x)(\omega_0 + iv_g \frac{\partial}{\partial x})\hat{a}(x) + V_{\mathrm{at}}\delta(x)(\hat{\sigma}^+\hat{a}(x) + \hat{\sigma}^-\hat{a}^\dagger(x))\big] + \hat{\sigma}^+\hat{\sigma}^-(\omega_{\mathrm{at}} - i\gamma_l), \tag{E.1}$$

and use a generalized single-excitation wavefunction

$$|\Psi\rangle = \left[\int_{-\infty}^{\infty} dx \phi_a(x,t)\hat{a}^\dagger(x) + \phi_{\mathrm{at}}\hat{\sigma}^+\right]|0\rangle. \tag{E.2}$$

With this, the time-dependent Schrödinger equation $i\hbar\partial_t|\Psi\rangle = \hat{H}|\Psi\rangle$ is given by

$$\begin{aligned}\hat{H}\,|\Psi\rangle =& -iv_g \int_{-\infty}^{\infty} dx \hat{a}^\dagger(x)\,[\partial_x\phi_a(x,t)] + \int_{-\infty}^{\infty} dx \delta(x) V_{\mathrm{at}}\phi_{\mathrm{at}}(t)\hat{a}^\dagger(x)\\ &+ \int_{-\infty}^{\infty} dx \delta(x) V_{\mathrm{at}}\phi_a(x,t)\hat{\sigma}^+ + \Delta_a\phi_{\mathrm{at}}(t)\hat{\sigma}^+\\ i\partial_t\,|\Psi\rangle =& i\int_{-\infty}^{\infty} dx \partial_t\phi_a(x,t)\hat{a}^\dagger(x) + i\partial_t\phi_{\mathrm{at}}(t)\hat{\sigma}^+.\end{aligned} \tag{E.3}$$

In order to solve this equation, we assume for the atom a time-dependent probability amplitude

$$\phi_{\mathrm{at}}(t) = e^{-i\omega t}e^{-\gamma t}\Theta(t), \tag{E.4}$$

describing the atomic decay with rate 2γ for times $t > 0$. For the field inside the resonator, we can assume

$$\phi_a(x,t) = \sqrt{\frac{2\gamma\beta}{v_g}}\, e^{i(kx-\omega t)} e^{\gamma/\omega(kx-\omega t)}\Theta(\omega t - kx), \tag{E.5}$$

where a running wave is being emitted in forwards direction. Most importantly, note that the normalisation for $\phi_a(x,t)$ has been calculated such that

$$\lim_{t\to\infty}\int_{-\infty}^{\infty} dx\,|\phi_a|^2 = \beta, \tag{E.6}$$

where the probability to find the emitted photon in the waveguide for long times is per definition β. With this normalization, one can plug this Ansatz functions into the Schrödingers equation and can solve for $V_{\mathrm{at}} = \sqrt{2\beta\gamma v_g}$ accordingly.

References

[1] M. Planck, “Ueber das Gesetz der Energieverteilung im Normalspectrum,” *Ann. Phys.*, 1901.

[2] A. Einstein, “Über einen die Erzeugung und Verwandlung des Lichtes betreffenden heuristischen Gesichtspunkt,” *Ann. Phys.*, 1905.

[3] E. Schrödinger, “Quantisierung als Eigenwertproblem,” *Ann. Phys.*, vol. 79,80 & 81, 1926.

[4] P. A. M. Dirac, “The quantum theory of the electron,” *Proc. R. Soc. London. Ser. A*, vol. 117, no. 778, 1928.

[5] E. M. Purcell, “Spontaneous emission probabilities at radio frequencies,” *Phys. Rev.*, vol. 69, no. 11-12, p. 674, 1946.

[6] P. R. Berman, *Cavity quantum electrodynamics*. Academic Press, 1994.

[7] T. Walther, Herbert and Varcoe, Benjamin TH and Englert, Berthold-Georg and Becker, H. Walther, B. T. H. Varcoe, B.-G. Englert, and T. Becker, “Cavity quantum electrodynamics,” *Reports Prog. Phys.*, vol. 69, no. 5, pp. 1325–1382, 2006.

[8] S. Haroche and D. Kleppner, “Cavity quantum electrodynamics,” *Phys. Today*, vol. 42, no. 1, p. 24, 1989.

[9] A. Reiserer and G. Rempe, “Cavity-based quantum networks with single atoms and optical photons,” *Rev. Mod. Phys.*, vol. 87, no. 4, 2015.

[10] E. T. Jaynes and F. W. Cummings, “Comparison of quantum and semiclassical radiation theories with application to a beam maser,” *IEEE*, vol. 51, no. 1, 1963.

[11] G. Rempe, H. Walther, and N. Klein, “Observation of quantum collapse and revival in a one-atom maser,” *Phys. Rev. Lett.*, vol. 58, no. 4, pp. 353–356, 1987.

[12] M. Tavis and F. W. Cummings, “Exact Solution for an N-Molecule-Radiation-Field Hamiltonian,” *Phys. Rev.*, vol. 170, no. 2, pp. 379–384, 1968.

[13] V. Giovannetti, S. Lloyd, and L. Maccone, “Advances in quantum metrology,” *Nat. Photonics*, vol. 5, no. 4, pp. 222–229, 2011.

[14] “Quantum Simulation. Insight issue.,” *Nat. Phys.*, vol. 8, no. 4, pp. 263–299, 2012.

[15] N. Gisin and R. Thew, “Quantum communication,” *Nat. Photonics*, vol. 1, no. 3, pp. 165–171, 2007.

[16] H. J. Kimble, “The quantum internet,” *Nature*, vol. 453, no. 7198, pp. 1023–1020, 2008.

[17] T. D. Ladd, F. Jelezko, R. Laflamme, Y. Nakamura, C. Monroe, and J. L. O’Brien, “Quantum computers,” *Nature*, vol. 464, no. 7285, pp. 45–53, 2010.

[18] Press Release, “The Nobel Prize in Physics 2012,” 2012.

[19] J. Dalibard and C. Cohen-Tannoudji, “Laser cooling below the Doppler limit by polarization gradients: simple theoretical models,” *J. Opt. Soc. Am. B*, vol. 6, no. 11, p. 2023, 1989.

[20] E. L. Raab, M. Prentiss, A. Cable, S. Chu, and D. E. Pritchard, “Trapping of Neutral Sodium Atoms with Radiation Pressure,” *Phys. Rev. Lett.*, vol. 59, no. 23, p. 2631, 1987.

[21] A. Ashkin and J. M. Dziedzic, “Optical trapping and manipulation of viruses and bacteria,” *Science*, vol. 235, no. 4795, pp. 1517–1520, 1987.

[22] F. L. Kien, V. I. Balykin, and K. Hakuta, “Atom trap and waveguide using a two-color evanescent light field around a subwavelength-diameter optical fiber,” *Phys. Rev. A*, vol. 70, no. 6, p. 063403, 2004.

[23] E. Vetsch, D. Reitz, G. Sagué, R. Schmidt, S. T. Dawkins, and A. Rauschenbeutel, “Optical interface created by laser-cooled atoms trapped in the evanescent field surrounding an optical nanofiber,” *Phys. Rev. Lett.*, vol. 104, no. 20, p. 203603, 2010.

[24] A. Goban, K. S. Choi, D. J. Alton, D. Ding, C. Lacroûte, M. Pototschnig, T. Thiele, N. P. Stern, and H. J. Kimble, “Demonstration of a state-insensitive, compensated nanofiber trap,” *Phys. Rev. Lett.*, vol. 109, no. 3, p. 033603, 2012.

[25] N. V. Corzo, B. Gouraud, A. Chandra, A. Goban, A. S. Sheremet, D. V. Kupriyanov, and J. Laurat, “Large Bragg Reflection from One-Dimensional Chains of Trapped Atoms Near a Nanoscale Waveguide,” *Phys. Rev. Lett.*, vol. 117, no. 13, 2016.

[26] D. Reitz, C. Sayrin, R. Mitsch, P. Schneeweiss, and A. Rauschenbeutel, “Coherence properties of nanofiber-trapped cesium atoms,” *Phys. Rev. Lett.*, vol. 110, no. 24, p. 243603, 2013.

[27] R. Mitsch, C. Sayrin, B. Albrecht, P. Schneeweiss, and A. Rauschenbeutel, “Exploiting the local polarization of strongly confined light for sub-micrometer-resolution internal state preparation and manipulation of cold atoms,” *Phys. Rev. A*, vol. 89, no. 6, p. 063829, 2014.

[28] F. Le Kien, S. Dutta Gupta, V. I. Balykin, and K. Hakuta, “Spontaneous emission of a cesium atom near a nanofiber: Efficient coupling of light to guided modes,” *Phys. Rev. A*, vol. 72, no. 3, p. 032509, 2005.

[29] B. Gouraud, D. Maxein, A. Nicolas, O. Morin, and J. Laurat, “Demonstration of a Memory for Tightly Guided Light in an Optical Nanofiber,” *Phys. Rev. Lett.*, vol. 114, no. 18, 2015.

[30] C. Sayrin, C. Clausen, B. Albrecht, P. Schneeweiss, and A. Rauschenbeutel, “Storage of fiber-guided light in a nanofiber-trapped ensemble of cold atoms,” *Optica*, vol. 2, no. 4, pp. 353–356, 2015.

[31] M. Scheucher, A. Hilico, E. Will, J. Volz, and A. Rauschenbeutel, “Quantum optical circulator controlled by a single chirally coupled atom,” *Science*, vol. 354, no. 6319, pp. 1577–1580, 2016.

[32] A. Dareau, Y. Meng, P. Schneeweiss, and A. Rauschenbeutel, “Observation of Ultrastrong Spin-Motion Coupling for Cold Atoms in Optical Microtraps,” *Phys. Rev. Lett.*, vol. 121, no. 253603, 2018.

[33] P. Lodahl, S. Mahmoodian, S. Stobbe, P. Schneeweiss, J. Volz, A. Rauschenbeutel, H. Pichler, and P. Zoller, “Chiral quantum optics,” *Nature*, vol. 541, no. 7638, pp. 473–480, 2017.

[34] D. Meiser and P. Meystre, “Superstrong coupling regime of cavity quantum electrodynamics,” *Phys. Rev. A*, vol. 74, no. 6, pp. 6–9, 2006.

[35] N. M. Sundaresan, Y. Liu, D. Sadri, L. J. Szöcs, D. L. Underwood, M. Malekakhlagh, H. E. Türeci, and A. A. Houck, “Beyond Strong Coupling in a Multimode Cavity,” *Phys. Rev. X*, vol. 5, no. 2, p. 21035, 2015.

[36] R. Kuzmin, N. Mehta, N. Grabon, R. Mencia, and V. E. Manucharyan, “Superstrong coupling in circuit quantum electrodynamics,” *npj Quantum Inf.*, vol. 5, no. 20, 2019.

[37] J.-T. Shen and S. Fan, “Coherent photon transport from spontaneous emission in one-dimensional waveguides,” *Opt. Lett.*, vol. 30, no. 15, pp. 2001–2003, 2005.

[38] J.-T. Shen and S. Fan, “Theory of single-photon transport in a single-mode waveguide. I. Coupling to a cavity containing a two-level atom,” *Phys. Rev. A*, vol. 79, no. 2, p. 023837, 2009.

[39] J.-T. Shen and S. Fan, “Theory of single-photon transport in a single-mode waveguide. II. Coupling to a whispering-gallery resonator containing a two-level atom,” *Phys. Rev. A*, vol. 79, no. 2, p. 023838, 2009.

[40] J. A. Giordmaine and R. C. Miller, “Tunable Coherent Parametric Oscillation in LiNbO3 at Optical Frequencies,” *Phys. Rev. Lett.*, vol. 14, no. 24, pp. 973–976, 1965.

[41] R. E. Slusher, L. W. Hollberg, B. Yurke, J. C. Mertz, and J. F. Valley, “Observation of Squeezed States Generated by Four-Wave Mixing in an Optical Cavity,” *Phys. Rev. Lett.*, vol. 55, no. 22, pp. 2409–2412, 1985.

[42] M. Aspelmeyer, T. J. Kippenberg, and F. Marquardt, “Cavity optomechanics,” *Rev. Mod. Phys.*, vol. 86, no. 4, pp. 1391–1452, 2014.

[43] S. M. Spillane, T. J. Kippenberg, K. J. Vahala, K. W. Goh, E. Wilcut, and H. J. Kimble, “Ultrahigh-Q toroidal microresonators for cavity quantum electrodynamics,” *Phys. Rev. A*, vol. 71, no. 1, p. 013817, 2005.

[44] M. Pöllinger, D. O’Shea, F. Warken, and A. Rauschenbeutel, “Ultrahigh-Q Tunable Whispering-Gallery-Mode Microresonator,” *Phys. Rev. Lett.*, vol. 103, no. 5, p. 053901, 2009.

[45] R. Paschotta and Others, *Encyclopedia of laser physics and technology*, vol. 1. Wiley Online Library, 2008.

[46] K. J. Vahala, “Optical microcavities,” *Nature*, vol. 424, no. 6950, pp. 839–846, 2003.

[47] M. Fox, *Quantum optics: an introduction*. Oxford Master Series in Atomic, Optical and Laser Physics, Oxford: Oxford Univ. Press, 2006.

[48] S. H. Autler and C. H. Townes, “Stark Effect in Rapidly Varying Fields,” *Phys. Rev.*, vol. 100, no. 2, pp. 703–722, 1955.

[49] M. Brune, F. Schmidt-Kaler, A. Maali, J. Dreyer, E. Hagley, J. M. Raimond, and S. Haroche, “Quantum Rabi Oscillation: A Direct Test of Field Quantization in a Cavity,” *Phys. Rev. Lett.*, vol. 76, no. 11, pp. 1800–1803, 1996.

[50] R. J. Thompson, G. Rempe, and H. J. Kimble, “Observation of normal-mode splitting for an atom in an optical cavity,” *Phys. Rev. Lett.*, vol. 68, no. 8, pp. 1132–1135, 1992.

[51] D. A. Steck, *Quantum and Atom Optics*. 2012.

[52] H. Carmichael, *An open systems approach to quantum optics*. Springer Science & Business Media, 2009.

[53] A. Johnson, M. Blaha, A. E. Ulanov, A. Rauschenbeutel, P. Schneeweiss, and J. Volz, “Observation of Collective Superstrong Coupling of Cold Atoms to a 30-m Long Optical Resonator,” *Phys. Rev. Lett.*, vol. 123, no. 24, p. 243602, 2019.

[54] P. Schneeweiss, S. Zeiger, T. Hoinkes, A. Rauschenbeutel, and J. Volz, “Fiber ring resonator with nanofiber section for chiral cavity quantum electrodynamics and multimode strong coupling,” *Opt. Lett.*, vol. 42, no. 1, pp. 85–88, 2017.

[55] S. K. Ruddell, K. E. Webb, I. Herrera, A. S. Parkins, and M. D. Hoogerland, “Collective strong coupling of cold atoms to an all-fiber ring cavity,” *Optica*, vol. 4, no. 5, p. 576, 2017.

[56] W. Li, J. Du, V. G. Truong, and S. Nic Chormaic, “Optical nanofiber-based cavity induced by periodic air-nanohole arrays,” *Appl. Phys. Lett.*, vol. 110, no. 25, p. 253102, 2017.

[57] C. Wuttke, M. Becker, S. Brückner, M. Rothhardt, and A. Rauschenbeutel, “Nanofiber Fabry-Perot microresonator for nonlinear optics and cavity quantum electrodynamics.,” *Opt. Lett.*, vol. 37, no. 11, pp. 1949–1951, 2012.

[58] S. Kato and T. Aoki, “Strong Coupling between a Trapped Single Atom and an All-Fiber Cavity,” *Phys. Rev. Lett.*, vol. 115, no. 9, pp. 1–5, 2015.

[59] K. P. Nayak, M. Sadgrove, R. Yalla, F. Le Kien, and K. Hakuta, “Nanofiber quantum photonics,” *J. Opt.*, vol. 20, no. 7, p. 073001, 2018.

[60] A. Yariv, *Quantum Electronics*. Wiley Online Library, 3rd ed., 1989.

[61] F. Le Kien and K. Hakuta, “Cavity-enhanced channeling of emission from an atom into a nanofiber,” *Phys. Rev. A*, vol. 80, no. 5, p. 053826, 2009.

[62] A. Asenjo-Garcia, M. Moreno-Cardoner, A. Albrecht, H. J. Kimble, and D. E. Chang, “Exponential Improvement in Photon Storage Fidelities Using Subradiance and Selective Radiance in Atomic Arrays,” *Phys. Rev. X*, vol. 7, no. 3, p. 031024, 2017.

[63] F. L. Kien and A. Rauschenbeutel, “Anisotropy in scattering of light from an atom into the guided modes of a nanofiber,” *Phys. Rev. A*, vol. 90, no. 2, 2014.

[64] A. Beer, “Bestimmung der Absorption des rothen Lichts in farbigen Flüssigkeiten,” *Ann. Phys.*, vol. 162, no. 5, pp. 78–88, 1852.

[65] S. Mahmoodian, M. Čepulkovskis, S. Das, P. Lodahl, K. Hammerer, and A. S. Sørensen, “Strongly Correlated Photon Transport in Waveguide Quantum Electrodynamics with Weakly Coupled Emitters,” *Phys. Rev. Lett.*, vol. 121, no. 14, p. 143601, 2018.

[66] R. Kumar, V. Gokhroo, K. Deasy, and S. N. Chormaic, “Autler-Townes splitting via frequency up-conversion at ultralow-power levels in cold 87 Rb atoms using an optical nanofiber,” *Phys. Rev. A - At. Mol. Opt. Phys.*, vol. 91, no. 5, pp. 2–6, 2015.

[67] S. G. Leon-Saval, T. A. Birks, W. J. Wadsworth, P. S. Russell, and M. W. Mason, “Supercontinuum generation in submicron fibre waveguides,” *Opt. Express*, vol. 12, p. 2864, jun 2004.

[68] T. A. Birks, W. J. Wadsworth, and P. S. J. Russell, “Supercontinuum generation in tapered fibers,” *Opt. Lett.*, vol. 25, p. 1415, oct 2000.

[69] R. Yalla, M. Sadgrove, K. P. Nayak, and K. Hakuta, “Cavity quantum electrodynamics on a nanofiber using a composite photonic crystal cavity,” *Phys. Rev. Lett.*, vol. 113, no. 14, pp. 1–5, 2014.

[70] P. Solano, J. A. Grover, J. E. Hoffman, S. Ravets, F. K. Fatemi, L. A. Orozco, and S. L. Rolston, “Optical Nanofibers: a new platform for quantum optics,” *Adv. At. Mol. Opt. Phys.*, vol. 66, pp. 439–505, 2017.

[71] T. Nieddu, V. Gokhroo, and S. N. Chormaic, “Optical nanofibres and neutral atoms,” *J. Opt.*, vol. 18, no. 5, p. 53001, 2016.

[72] L. Liebermeister, F. Petersen, A. V. Münchow, D. Burchardt, J. Hermelbracht, T. Tashima, A. W. Schell, O. Benson, T. Meinhardt, A. Krueger, A. Stiebeiner, A. Rauschenbeutel, H. Weinfurter, and M. Weber, “Tapered fiber coupling of single photons emitted by a deterministically positioned single nitrogen vacancy center,” *Appl. Phys. Lett.*, vol. 104, no. 031101, 2014.

[73] A. Stiebeiner, O. Rehband, R. Garcia-Fernandez, and A. Rauschenbeutel, "Ultrasensitive fluorescence spectroscopy of isolated surface-adsorbed molecules using an optical nanofiber," *Opt. Express*, vol. 17, no. 24, p. 21704, 2009.

[74] A. W. Snyder and J. D. Love, *Optical Waveguide Theory*. Capman and Hall, 1983.

[75] F. Le Kien, J. Q. Liang, K. Hakuta, and V. I. Balykin, "Field intensity distributions and polarization orientations in a vacuum-clad subwavelength-diameter optical fiber," *Opt. Commun.*, vol. 242, no. 4-6, pp. 445–455, 2004.

[76] F. Warken, E. Vetsch, D. Meschede, M. Sokolowski, and A. Rauschenbeutel, "Ultrasensitive surface absorption spectroscopy using sub-wavelength diameter optical fibers," *Opt. Express*, vol. 15, no. 19, pp. 11952–11958, 2007.

[77] L. Tong, R. R. Gattass, J. B. Ashcom, S. He, J. Lou, M. Shen, I. Maxwell, and E. Mazur, "Subwavelength-diameter silica wires for low-loss optical wave guiding," *Nature*, vol. 426, no. 6968, pp. 816–819, 2003.

[78] F. Warken, *Ultradünne Glasfasern als Werkzeug zur Kopplung von Licht und Materie*. Phd thesis, Rheinische Friedrich-Willhelm-Universität Bonn, 2007.

[79] M. Pollinger, *Bottle microresonators for applications in quantum optics and all-optical signal processing*. PhD thesis, Johannes Gutenberg-Universität in Mainz, 2010.

[80] L. Ding, C. Belacel, S. Ducci, G. Leo, and I. Favero, "Ultralow loss single-mode silica tapers manufactured by a microheater," *Appl. Opt.*, vol. 49, no. 13, pp. 2441–2445, 2010.

[81] T. E. Dimmick, G. Kakarantzas, T. A. Birks, and P. S. J. Russell, "Carbon dioxide laser fabrication of fused-fiber couplers and tapers," *Appl. Opt.*, vol. 38, no. 33, pp. 6845–6848, 1999.

[82] S. Xie, R. Pennetta, and P. S. J. Russell, "Self-alignment of glass fiber nanospike by optomechanical back-action in hollow-core photonic crystal fiber," *Optica*, vol. 3, no. 3, p. 277, 2016.

[83] P. Lambelet, A. Sayah, M. Pfeffer, C. Philipona, and F. Marquis-Weible, "Chemically etched fiber tips for near-field optical microscopy: a process for smoother tips," *Appl. Opt.*, vol. 37, no. 31, pp. 7289–7292, 1998.

[84] H. J. Kbashi, "Fabrication of Submicron-Diameter and Taper Fibers Using Chemical Etching," *J. Mater. Sci. Technol.*, vol. 28, no. 4, pp. 308–312, 2012.

[85] J. D. Love, W. M. Henry, W. J. Stewart, R. J. Black, S. Lacroix, and F. Gonthier, "Tapered single-mode fibres and devices Part 1. Adiabaticity criteria," *IEE proceedings. Part J, Optoelectron.*, vol. 138, no. 5, pp. 343–354, 1991.

[86] R. J. Black, S. Lacroix, F. Gonthier, and J. D. Love, "Tapered single-mode fibres and devices Part 2. Experimental and theoretical quantification," *IEE proceedings. Part J, Optoelectron.*, vol. 138, no. 5, pp. 355–364, 1991.

[87] T. A. Birks and Y. W. Li, "The Shape of Fiber Tapers," *J. Light. Technol.*, vol. 10, no. 4, pp. 432–438, 1992.

[88] J. D. Love and W. M. Henry, "Quantifying Loss Minimisation in Single-Mode Fibre Tapers," *Electron. Lett.*, vol. 22, no. 17, pp. 912–914, 1986.

[89] W. Stewart, "Design limitation on tapers and couplers in single-mode fibers," *Tech. Dig. IOOC-ECOC*, vol. 1, pp. 559–562, 1985.

[90] A. Stiebeiner, R. Garcia-Fernandez, and A. Rauschenbeutel, "Design and optimization of broadband tapered optical fibers with a nanofiber waist," *Opt. Express*, vol. 18, no. 22, p. 22677, 2010.

[91] R. Nagai and T. Aoki, "Ultra-low-loss tapered optical fibers with minimal lengths.," *Opt. Express*, vol. 22, no. 23, pp. 28427–28436, 2014.

[92] K. Harrington, S. Yerolatsitis, D. Van Ras, D. M. Haynes, and T. A. Birks, "Endlessly adiabatic fiber with a logarithmic refractive index distribution," *Optica*, vol. 4, no. 12, p. 1526, 2017.

[93] C. Lutzler, *Fabrication of Optical Microfibers*. Master thesis, Rheinische Friedrich-Wilhelms-Universität Bonn, 2012.

[94] L. Fischer, *Transmission characterization as a tool for nanofiber fabrication*. Bachelor thesis, TU Wien, 2018.

[95] F. Le Kien, V. Balykin, and K. Hakuta, "State-insensitive trapping and guiding of cesium atoms using a two-color evanescent field around a subwavelength-diameter fiber," *IQEC, Int. Quantum Electron. Conf. Proc.*, vol. 2005, pp. 125–126, 2005.

[96] T. W. Hansch and B. Couillaud, "Laser frequency stabilization by polarization spectroscopy of a reflecting reference cavity," *Opt. Commun.*, vol. 35, no. 3, pp. 441–444, 1980.

[97] R. C. Jones, "A New Calculus for the Treatment of Optical Systems," *J. Opt. Soc. Am.*, vol. 31, no. 7, pp. 488–493, 1941.

[98] A. Libson, N. Brown, A. Buikema, C. C. López, T. Dordevic, M. Heising, and M. Evans, "Simple method for locking birefringent resonators," *Opt. Express*, vol. 23, no. 3, p. 3809, 2015.

[99] R. V. Pound, "Electronic frequency stabilization of microwave oscillators," *Rev. Sci. Instrum.*, vol. 17, no. 11, pp. 490–505, 1946.

[100] R. W. Drever, J. L. Hall, F. V. Kowalski, J. Hough, G. M. Ford, A. J. Munley, and H. Ward, "Laser phase and frequency stabilization using an optical resonator," *Appl. Phys. B*, vol. 31, no. 2, pp. 97–105, 1983.

[101] K. Flöckner, *Frequenzstabilisierung eines Diodenlasers für die Spektroskopie eines Faserringresonator*. Bachelor thesis, TU Wien, 2019.

[102] C. Wuttke, G. D. Cole, and A. Rauschenbeutel, "Optically active mechanical modes of tapered optical fibers," *Phys. Rev. A*, vol. 88, no. 6, p. 061801, 2013.

[103] D. Hümmer, P. Schneeweiss, A. Rauschenbeutel, and O. Romero-Isart, “Heating in Nanophotonic Traps for Cold Atoms,” *Phys. Rev. X*, vol. 9, no. 4, p. 41034, 2019.

[104] J. G. Hinney, *Generation of squeezed light with nanofiber-trapped atoms*. Phd thesis, TU Wien, 2019.

[105] A. S. Prasad, *Generating correlations between photons via interaction with nanofiber trapped atoms*. Phd thesis, TU Wien, 2020.

[106] M. Blaha, *Combined Polarisation and Absorption Imaging for experiments with Nanofiber trapped atoms*. Master thesis, TU Wien, 2016.

[107] M. Succi, R. Canino, and B. Ferrario, “Atomic absorption evaporation flow rate measurements of alkali metal dispensers,” *Vacuum*, vol. 35, no. 12, pp. 579–582, 1985.

[108] N. Solmeyer, K. Zhu, and D. S. Weiss, “Note: Mounting ultra-high vacuum windows with low stress-induced birefringence,” *Rev. Sci. Instrum.*, vol. 82, no. 6, p. 066105, 2011.

[109] C. Wuttke, *Thermal excitations of optical nanofibers measured with a fiber-integrated Fabry-Perot cavity*. Phd thesis, Jphannes Gutenberg Universität März, 2014.

[110] E. R. Abraham and E. A. Cornell, “Teflon feedthrough for coupling optical fibers into ultrahigh vacuum systems,” *Appl. Opt.*, vol. 37, no. 10, p. 1762, 1998.

[111] P. D. Lett, W. D. Phillips, S. L. Rolston, C. E. Tanner, R. N. Watts, and C. I. Westbrook, “Optical molasses,” *J. Opt. Soc. Am. B*, vol. 6, no. 11, p. 2084, 1989.

[112] C. Foot, *Atomic Physics (Oxford Master Series in Atomic, Optical and Laser Physics)*. Oxford Univ. Press, 2005.

[113] W. Ketterle, K. B. Davis, M. A. Joffe, A. Martin, and D. E. Pritchard, “High densities of cold atoms in a dark spontaneous-force optical trap,” *Phys. Rev. Lett.*, vol. 70, no. 15, pp. 2253–2256, 1993.

[114] M. Pichler, *Doppler-free Laser Spectroscopy of Cesium and Applications for Laser Locking*. Project thesis, TU Wien, 2017.

[115] J. B. Béguin, E. M. Bookjans, S. L. Christensen, H. L. Sørensen, J. H. Müller, E. S. Polzik, and J. Appel, “Generation and Detection of a Sub-Poissonian Atom Number Distribution in a One-Dimensional Optical Lattice,” *Phys. Rev. Lett.*, vol. 113, no. 26, p. 263603, 2014.

[116] J. A. Grover, P. Solano, L. A. Orozco, and S. L. Rolston, “Photon-correlation measurements of atomic-cloud temperature using an optical nanofiber,” *Phys. Rev. A*, vol. 92, no. 1, p. 13850, 2015.

[117] K. P. Nayak, F. Le Kien, M. Morinaga, and K. Hakuta, “Antibunching and bunching of photons in resonance fluorescence from a few atoms into guided modes of an optical nanofiber,” *Phys. Rev. A*, vol. 79, no. 2, p. 021801, 2009.

[118] R. Hanbury Brown and R. Q. Twiss, “Correlation between Photons in two Coherent Beams of Light,” *Nature*, vol. 177, no. 27-29, 1956.

[119] H. J. Kimble, M. Dagenais, and L. Mandel, "Photon antibunching in resonance fluorescence," *Phys. Rev. Lett.*, vol. 39, no. 11, pp. 691–695, 1977.

[120] B. Lounis and W. E. Moerner, "Single photons on demand from a single molecule at room temperature," *Nature*, vol. 407, pp. 491–493, 2000.

[121] X. T. Zou and L. Mandel, "Photon-antibunching and sub-Poissonian photon statistics," *Phys. Rev. A*, vol. 41, no. 1, pp. 475–476, 1990.

[122] S. Singh, "Antibunching, sub-poissonian photon statistics and finite bandwidth effects in resonance fluorescence," *Opt. Commun.*, vol. 44, no. 4, pp. 254–258, 1983.

[123] F. Diedrich and H. Walther, "Nonclassical radiation of a single stored ion," *Phys. Rev. Lett.*, vol. 58, no. 3, pp. 203–206, 1987.

[124] V. Gomer, B. Ueberholz, S. Knappe, F. Strauch, D. Frese, and D. Meschede, "Decoding the dynamics of a single trapped atom from photon correlations," *Appl. Phys. B Lasers Opt.*, vol. 67, pp. 689–697, 1998.

[125] F. Le Kien and K. Hakuta, "Correlations between photons emitted by multiatom fluorescence into a nanofiber," *Phys. Rev. A*, vol. 77, no. 3, p. 033826, 2008.

[126] D. A. Steck, "Cesium D Line Data,"

[127] R. Verberk and M. Orrit, "Photon statistics in the fluorescence of single molecules and nanocrystals: Correlation functions versus distributions of on- and off-times," *J. Chem. Phys.*, vol. 119, no. 4, pp. 2214–2222, 2003.

[128] A. Camara, R. Kaiser, and G. Labeyrie, "Scaling behavior of a very large magneto-optical trap," *Phys. Rev. A*, vol. 90, no. 6, p. 063404, 2014.

[129] D. O. Krimer, M. Liertzer, S. Rotter, and H. E. Türeci, "Route from spontaneous decay to complex multimode dynamics in cavity QED," *Phys. Rev. A*, vol. 89, no. 3, p. 33820, 2014.

[130] H. S. Dhar, M. Zens, D. O. Krimer, and S. Rotter, "Variational Renormalization Group for Dissipative Spin-Cavity Systems: Periodic Pulses of Nonclassical Photons from Mesoscopic Spin Ensembles," *Phys. Rev. Lett.*, vol. 121, no. 13, p. 133601, 2018.

[131] C. Kwong, T. Yang, M. S. Pramod, K. Pandey, D. Delande, R. Pierrat, and D. Wilkowski, "Cooperative Emission of a Coherent Superflash of Light," *Phys. Rev. Lett.*, vol. 113, no. 22, p. 223601, 2014.

[132] S. Haroche, J. A. Paisner, and A. L. Schawlow, "Hyperfine Quantum Beats Observed in Cs Vapor under Pulsed Dye Laser Excitation," *Phys. Rev. Lett.*, vol. 30, no. 20, pp. 948–951, 1973.

[133] M. O. Araújo, I. Krešić, R. Kaiser, and W. Guerin, "Superradiance in a Large and Dilute Cloud of Cold Atoms in the Linear-Optics Regime," *Phys. Rev. Lett.*, vol. 117, no. 7, p. 073002, 2016.

[134] W. Guerin, T. S. E. Santo, P. Weiss, A. Cipris, J. Schachenmayer, R. Kaiser, and R. Bachelard, "Collective Multimode Vacuum Rabi Splitting," *Phys. Rev. Lett.*, vol. 123, no. 24, p. 243401, 2019.

[135] T. S. do Espirito Santo, P. Weiss, A. Cipris, R. Kaiser, W. Guerin, R. Bachelard, and J. Schachenmayer, "Collective excitation dynamics of a cold atom cloud," *Phys. Rev. A*, vol. 101, no. 1, p. 013617, 2020.

[136] X. Yu, D. Xiong, H. Chen, P. Wang, M. Xiao, and J. Zhang, "Multi-normal-mode splitting of a cavity in the presence of atoms: A step towards the superstrong-coupling regime," *Phys. Rev. A*, vol. 79, no. 6, 2009.

[137] Y. Colombe, T. Steinmetz, G. Dubois, F. Linke, D. Hunger, and J. Reichel, "Strong atom–field coupling for Bose–Einstein condensates in an optical cavity on a chip," *Nature*, vol. 450, no. 7167, pp. 272–276, 2007.

[138] V. D. Vaidya, Y. Guo, R. M. Kroeze, K. E. Ballantine, A. J. Kollár, J. Keeling, and B. L. Lev, "Tunable-Range, Photon-Mediated Atomic Interactions in Multimode Cavity QED," *Phys. Rev. X*, vol. 8, no. 1, p. 11002, 2018.

[139] F. Brennecke, T. Donner, S. Ritter, T. Bourdel, M. Köhl, and T. Esslinger, "Cavity QED with a Bose–Einstein condensate," *Nature*, vol. 450, no. 7167, pp. 268–271, 2007.

[140] J. Lee, G. Vrijsen, I. Teper, O. Hosten, and M. A. Kasevich, "Many-atom–cavity QED system with homogeneous atom–cavity coupling," *Opt. Lett.*, vol. 39, no. 13, p. 4005, 2014.

[141] T. Carmon, L. Yang, and K. J. Vahala, "Dynamical thermal behavior and thermal self-stability of microcavities," *Opt. Express*, vol. 12, no. 20, p. 4742, 2004.

[142] T. A. Birks, P. S. J. Russell, and C. N. Pannell, "Low Power acousto-optic device based on a tapered single-mode fiber," *IEEE Photonics Technol. Lett.*, vol. 6, no. 6, p. 725, 1994.

[143] T. A. Birks, D. O. Culverhouse, S. G. Farwell, and P. S. J. Russell, "All-fiber polarizer based on a null taper coupler," *Opt. Lett.*, vol. 20, no. 12, p. 1371, 1995.

[144] T. A. Birks, S. G. Farwell, P. S. J. Russell, and C. N. Pannell, "Four-port fiber frequency shifter with a null taper coupler: erratum," *Opt. Lett.*, vol. 21, no. 3, p. 231, 1996.

[145] M. Sadgrove and K. P. Nayak, "Composite device for interfacing an array of atoms with a single nanophotonic cavity mode," *New J. Phys.*, vol. 19, no. 6, p. 063003, 2017.

[146] J. D. Thompson, T. G. Tiecke, N. P. De Leon, J. Feist, A. V. Akimov, M. Gullans, A. S. Zibrov, V. Vuletić, and M. D. Lukin, "Coupling a single trapped atom to a nanoscale optical cavity," *Science*, vol. 340, no. 6137, pp. 1202–1205, 2013.

[147] K. Sinha, P. Meystre, E. A. Goldschmidt, F. K. Fatemi, S. L. Rolston, and P. Solano, "Non-Markovian Collective Emission from Macroscopically Separated Emitters," *Phys. Rev. Lett.*, vol. 124, no. 4, p. 043603, 2020.

[148] H. Tanji-Suzuki, W. Chen, R. Landig, J. Simon, and V. Vuletić, "Vacuum-induced transparency," *Science*, vol. 333, no. 6047, pp. 1266–1269, 2011.

[149] Y.-J. Guo and W.-J. Nie, "Vacuum induced transparency and slow light phenomena in a two-level atomic ensemble controlled by a cavity," *Chinese Phys. B*, vol. 24, no. 9, p. 094205, 2015.

[150] V. Torggler, S. Krämer, and H. Ritsch, "Quantum annealing with ultracold atoms in a multimode optical resonator," *Phys. Rev. A*, vol. 95, no. 3, p. 032310, 2017.

[151] P. L. McMahon, A. Marandi, Y. Haribara, R. Hamerly, C. Langrock, S. Tamate, T. Inagaki, H. Takesue, S. Utsunomiya, K. Aihara, R. L. Byer, M. M. Fejer, H. Mabuchi, and Y. Yamamoto, "A fully programmable 100-spin coherent Ising machine with all-to-all connections," *Science*, vol. 354, no. 6312, pp. 614–617, 2016.

[152] C. Junge, *Cavity quantum electrodynamics with non-transversal photons*. Phd thesis, TU Wien, 2013.

[153] M. Scheucher, *Single-atom cavity quantum electrodynamics with whispering-gallery-modes: Single-photon nonlinearity and nonreciprocity*. Phd thesis, TU Wien, 2017.

Acknowledgements

My final words of this thesis are dedicated to all the wonderful people that supported and encouraged me in past years during the challenging task of pursuing my PhD in Physics. I feel like not only were they responsible for my scientific, but foremost my overall maturity.

At first, I would like to thank my supervisor and head of the group Arno Rauschenbeutel, who gave me the opportunity to set up a new experimental apparatus in his group. His rousing lectures were the reason for my initial interest in the field of quantum optics, as he always manages to explain even the most complicated concepts in a clear and inspiring fashion.

I am deeply grateful for the help and fruitful discussions with Jürgen Volz, without whom this project would probably not have succeeded in such a pace. His patient approach and ability to ask tricky questions about our experimental proceedings as well as his intuitive understanding and comprehensible ways of passing on his insights on the theoretical background of our experiment always struck me fascinated. He is the reason I will always continue to prepare two coffees at once. My coffee addiction will be forever in his favour.

I would like to especially thank Jakob Hinney and Christoph Clausen, who mentored me during my master's thesis and, through their enthusiasm for physics, inspired me to start my PhD studies. I like to thank Aisling Johnson, with whom I spent three years in the lab and nevertheless managed to become good friends. I enjoyed the spirit and dynamics of our collaboration at work and the musical jam-session outside of it. I learned a lot from her.

Furthermore, I would like to highlight the extremely open-hearted environment in our group and at the Atominstitut in Vienna in general, where the scientific and non-scientific discussions in the hallways, coffee-rooms and occasional BBQs often helped overcoming experimental obstacles or led to a significant boost of spirit. During my time spent in this group I gathered many valued colleagues, many of which became friends.

I would also like to thank the people outside of science, who are responsible for the many sweet things in life. Firstly, I would like to thank the people of Team Grizzly (your grandmas favourite lifting crew) and Berlin Strength, where I found a home for my second huge passion, competitive powerlifting.

Secondly, I thank my brother-of-another-mother, Dominik, my oldest and deepest companion, for being there for every high and low in my life, always grounding me. He is in a way responsible for the balance in my life, whether it is hanging in the wall by the side of a mountain or charging at the stages of a music festival.

Finally, I am deeply thankful for the support of my family, above all my mother who always believed in me and supported me throughout this journey. – Thank you very much

LEBENSLAUF

Martin Blaha
Anningerstraße 76-78/4
2353 Guntramsdorf
Österreich

Persönliche Daten

Geburtsdatum:	22. Mai 1991
Geburtsort:	Wien
Staatsangehörigkeit:	Österreich

Ausbildung

seit 2016	Doktorat der technischen Wissenschaften – Technische Physik, Technische Universität Wien
2014 - 2016	Master of Science in Technische Physik, Technische Universität Wien
2010 - 2014	Bachelor of Science in Technische Physik, Technische Universität Wien
2001 - 2009	Sport-Realgymnasium, Maria Enzersdorf
1997 - 2001	Volksschule, Guntramsdorf